UNDERSTANDING WIND-BLOWN SAND AND THE ELECTRIFICATION OF GRANULAR SYSTEMS

by

Jasper F. Kok

A dissertation submitted in partial fulfillment
of the requirements for the degree of
Doctor of Philosophy
(Applied Physics)
in The University of Michigan
2009

Doctoral Committee:

    Professor Nilton O. Renno, Chair
    Professor Roy Clarke
    Professor Emeritus William R. Kuhn
    Professor Emeritus Henry N. Pollack
    Professor Richard B. Rood

DEDICATION

To my dad

Our bathtub discussions about the universe when I was young
laid the foundation for this work

ACKNOWLEDGEMENTS

While I am immensely thankful for help, encouragement, and support from many people, I am especially grateful to my parents, my wife Shanna, and my advisor Nilton Renno.

My parents poured everything they had into me from the moment I was born, and I truly couldn't have wished for better parents. Without the loving, stable, and encouraging family environment they provided I would have never had the courage or motivation to move to the United States to pursue my Master's and now obtain my PhD. While this clearly backfired on my parents, coming 'home' is a delight every time, and I will also always treasure the memories from our sublime exotic vacations. While I am immensely and equally grateful to both my wonderful parents, my dad has been especially instrumental in my decision to pursue an academic career. When I was a child, we had many conversations about the origin of life and the universe, built a telescope to peer into the heavens, and visited many museums, observatories, and lectures on natural history and astronomy. All this instilled an intense sense of curiosity about the natural world in me that has been the seed out of which this work has grown. I am immensely thankful to my dad for this, which is why I gratefully dedicate my thesis to him.

My other source of inspiration has been my wonderful wife Shanna, who has directly and indirectly influenced most all of this thesis. Her constructive criticism improved both my writing and my science substantially. And her seemingly magical mastery of PowerPoint and other computer software has rubbed off on me in small quantities. But above all, I am grateful to Shanna for all her love and support, for always believing in my abilities, and of course for damping my 'high-frequency oscillations', especially during the first few years. In all, Shanna has not only been instrumental in getting me to the finish line, but has been the main reason that I have immensely enjoyed the journey there as well!

I was also very lucky to have an excellent advisor, Nilton Renno, to guide me through my PhD. I have learned much from Nilton's exemplary scientific and personal integrity, his ability to juggle many things at once, his daring to think outside of the box, and his generosity. From the moment I started working with him, Nilton has left me the independence to pursue my own ideas and encouraged me to work according to my own interests, rather than work on specific projects he favored. Nilton has thus consistently put my best interests ahead of his own, which is a rare trait in an advisor. The creative freedom he thus allowed me greatly contributed to my performance in graduate school. Nilton was also always available to provide guidance and a word of encouragement when needed and always seemed to trust and believe in my abilities much more than I did. I also sincerely appreciate the genuine interest and investment Nilton has shown in my continued academic success. Thank you so much for everything, Nilton!

I would also like to thank Jasper van Wezel, Earle Williams, Kristine Crous, Bill Kuhn, Michael Bretz, Chris Kelly, and Shanna Shaked for providing constructive criticism on my manuscripts; Dan Lacks, Manish Mehta, Keld Rasmussen, and Jon Merrison for collaborating with me; David Rea, Robb Gillespie, and Steven Rogacki for providing important help and guidance during my experimental work; and Donald Huffman, Ricky Rood, Bill Kuhn, Mary Anne Carroll, Jason Smerdon, Brad Orr, Robert Socolow, Henry Pollack, and Sheila Tobias for invaluable professional and personal advice. And thank you of course to my dissertation committee – Bill Kuhn, Roy Clarke, Ricky Rood, Henry Pollack, and Nilton Renno – for reading and commenting on my dissertation!

A special acknowledgement goes to the Applied Physics Program here at the University of Michigan. Stuck between physics and atmospheric science the way I am, the Applied Physics Program has been the perfect place for my interdisciplinary endeavors. The program really wants me and every other student they admit to succeed and has always been happy to help with whatever problems I encountered. Thank you so much, Brad Orr, Roy Clarke, Cyndi McNabb, and Charles Sutton for letting us all think, and reside, outside of the box!

I would also like to acknowledge all the great help I received from people in my advisor's department of Atmospheric, Oceanic, and Space Sciences. Thank you for all

TABLE OF CONTENTS

LIST OF FIGURES

CHAPTER 1
INTRODUCTION

The wind-blown transport of sediment is critical to a wide range of natural processes. For example, wind-blown sand creates sand dunes and dune ripples [*Bagnold*, 1941], and erodes geological features [*Greeley and Iversen*, 1985] and agricultural fields [*Sterk*, 2003]. Moreover, wind-blown sand, dust storms, and dust devils [*Shao*, 2000; *Renno et al.*, 2004] are the dominant sources of atmospheric dust aerosols, which play a major role in many Earth system processes [*Goudie and Middleton*, 2006; *IPCC*, 2001, 2007]. Indeed, dust aerosols provide limiting micronutrients such as iron and phosphorus to ecosystems [*Jickells et al.*, 2005], serve as cloud nuclei [*Twomey*, 1974; *DeMott et al.*, 2003], scatter and absorb both shortwave and longwave radiation [*Tegen and Lacis*, 1996; *Sokolik et al.*, 2001; *Myhre and Stordal*, 2001], enhance the melting of snow packs and glaciers upon deposition [*Painter et al.*, 2007], and possibly affect hurricane formation [*Sun et al.*, 2008]. Mineral dust aerosols are also a significant hazard to human health [*Prospero*, 1999]. Finally, the transport of sediment by wind shapes the landscapes of Mars, Venus, and Titan [e.g., *Greeley and Iversen*, 1985], and dust aerosols play a major role in the Martian climate [*Fenton et al.*, 2007].

As the wind speed increases, sand particles of ~70-500 μm diameter are the first to be moved by wind. After lifting, these particles bounce along the surface in a series of hops [*Bagnold*, 1941; *Greeley and Iversen*, 1985; *Shao*, 2000], in a process known as wind-blown sand or 'saltation' (Figure 1.1). The impact of these saltating particles on the soil surface can mobilize particles of a wide range of sizes. Indeed, dust particles, defined as particles with diameters < 62.5 μm [*Greeley and Iversen*, 1985], are not normally lifted by wind because their cohesive forces are large compared to the forces due to wind stress [*Gillette et al.*, 1974; *Shao and Lu*, 2000]. These small particles are instead ejected from the soil by the impacts of saltating particles [*Shao et al.*, 1993]. After their ejection, these dust particles can be transported upwards by convective motions and turbulent

eddies. Dust particles smaller than ~20 μm can travel thousands of kilometers from their source [*Gillette and Walker*, 1977], and affect the Earth system in a variety of manners as outlined above and in *Goudie and Middleton* [2006].
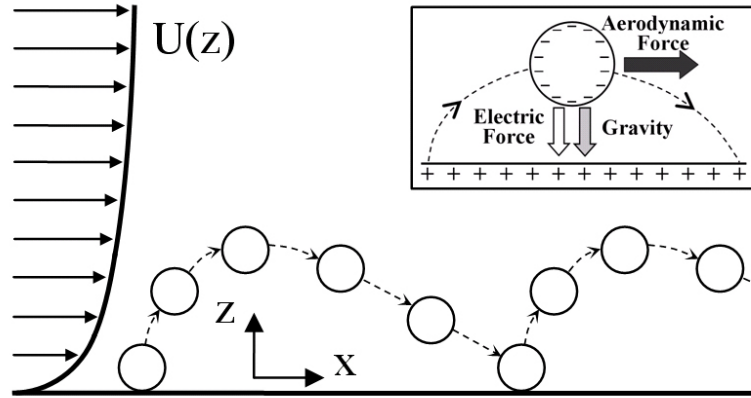
Figure 1.1: Schematic of saltation, showing the logarithmic wind profile *U*(*z*) (see Section 6.2.3) to the left of an idealized spherical sand particle propelled by wind and bouncing along the surface. Saltating particles absorb horizontal momentum from the wind, which is partially converted into vertical momentum during collisions with the soil surface. The inset illustrates the charge distribution in saltation in the absence of suspended dust, and shows a simplified force diagram of a negatively charged sand particle saltating over the positively charged soil surface. After *Kok and Renno* [2008].

Saltating particles can also mobilize larger particles. However, the acceleration of particles with diameters in excess of ~500 μm is strongly limited by their large inertia, and these particles generally do not saltate [*Shao*, 2000]. Instead, they roll or slide along the surface, driven by impacts of saltating particles and wind drag forces in a mode of transport known as 'creep' [*Bagnold*, 1941].

The transport of soil particles by wind can thus be separated into several physical regimes: long-term suspension (< 20 μm diameter), short-term suspension (~20 – 70 μm), saltation (~70 – 500 μm), and creep (> ~500 μm) [*Shao*, 2000]. Saltation is arguably the most important physical regime, because it occurs at the lowest wind speeds and it initiates the other three modes of wind-blown sediment transport [*Shao*, 2000].

As discussed above, a comprehensive understanding of saltation is thus critical to a wide range of problems across scientific disciplines. However, current numerical models of saltation are often based on empirical relations and are not yet able to correctly reproduce measurements of natural saltation [e.g., *Anderson and Haff*, 1988, 1991;

McEwan and Willetts, 1991; *Shao and Li*, 1999]. Moreover, neither these existing numerical models, nor the influential 'classical' theory of saltation [*Bagnold*, 1941; *Owen*, 1964], account for the effects of sand electrification. This is a potentially important omission, as electric fields (*E*-fields) in saltation can reach values in excess of 150 kV/m [*Schmidt et al.*, 1998], thereby affecting the mass flux and the trajectories of saltating particles [*Schmidt et al.*, 1998; *Zheng et al.*, 2003, 2006].

In this dissertation, I thus seek to contribute to an improved understanding of saltation by (i) performing a detailed investigation into the effects of sand electrification on saltation and dust lifting, (ii) by developing a quantitative theoretical model of the electrification of wind-blown sand and other granular systems of chemically identical insulators, and (iii), by developing the first comprehensive and physically-based numerical model of saltation that correctly reproduces measurements of natural saltation and can thus be used to study the wide range of scientific problems described above.

In the next Section, I briefly describe the basic physics of saltation. Subsequently, I summarize the current state of knowledge of sand and dust electrification. Finally, I discuss the specific scientific objectives of this thesis.

1.1 BASIC PHYSICS OF SALTATION

The physical parameter that drives saltation is the work done by the wind shear stress τ, which is usually expressed in terms of the wind shear velocity or friction velocity, $u* = \sqrt{\tau / \rho_a}$, where ρ_a is the air density. Saltation is initiated when this shear stress exerted by wind on the soil surface exceeds the threshold τ_t at which surface particles are lifted ($\tau_t \approx 0.05$ N/m^2 for loose sand). *Bagnold* [1941] derived a simple empirical expression for the threshold wind shear velocity at which loose sand particles start to saltate,

$$u *_t \equiv \sqrt{\tau_t / \rho_a} = A \sqrt{\frac{\left(\rho_p - \rho_a\right)}{\rho_a} g D_p} \, , \tag{1.1}$$

where $A \approx 0.10$ is a dimensionless scaling parameter, ρ_p and ρ_a are the particle and fluid densities, g is the gravitational acceleration, and D_p is the diameter of a sphere with the same volume as the irregularly shaped sand particle.

3

After saltation is initiated, the particles lifted from the surface exchange momentum with the wind. Upon striking the surface at angles of ~5-15˚ with the horizontal, these particles rebound at much steeper angles and thus acquire larger vertical speeds [*Rice et al.*, 1995, 1996; *Wang*, 2008]. After a few hops, saltating particles can be sufficiently accelerated by wind drag to eject (or 'splash') other particles when impacting the soil [*Bagnold*, 1973; *Ungar and Haff*, 1987]. These newly ejected particles are then accelerated by wind and eject more particles when impacting the surface. This causes an exponential increase in the number of saltating particles in the initial stages of saltation [*Anderson and Haff*, 1988, 1991; *Shao and Raupach*, 1992; *McEwan and Willetts*, 1993]. Indeed, this rapid exponential increase causes the flux of saltating particles to 'overshoot' the eventual steady-state mass flux [*Anderson and Haff*, 1988, 1991; *Shao and Raupach*, 1992; *McEwan and Willetts*, 1993], after which the exchange of momentum between the fluid and saltating particles reaches a steady state. This steady state is determined by the finite flux of momentum available to be transferred from the wind to the saltating particles, such that the wind speed during saltation is usually substantially reduced from that without saltation [e.g., *Owen*, 1964].

In steady-state saltation, surface particles are rarely lifted directly by fluid forces because the wind shear velocity at the surface is lower than the 'fluid threshold' given by Eq. (1.1). This surface wind shear is smaller than the threshold value because the transfer of momentum to the soil surface is dominated by the impacts of saltating particles, not by wind drag [*Bagnold*, 1937, 1973; *Ungar and Haff*, 1987; *Anderson and Haff*, 1988, 1991; *Shao and Raupach*, 1992; *McEwan and Willetts*, 1991, 1993]. As a result, once saltation is initiated, it can be maintained at shear velocities somewhat below the fluid threshold value (Eq. 1.1). This minimum shear velocity at which saltation can be maintained is termed the 'impact threshold' [*Bagnold*, 1941] and, for Earth ambient conditions, is approximately 80-85 % of the 'fluid threshold' defined by Eq. (1.1) [*Bagnold*, 1937].

A critical measure of the intensity of steady-state saltation is the height-integrated particle mass flux Q. Experiments show that Q increases approximately cubically with shear velocity [*Bagnold*, 1941; *Shao*, 2000], that is

$$Q = Q_0 \left(\rho_a / g \right) u*^3 , \qquad (1.2)$$

where g is the gravitational acceleration, and Q_0 the dimensionless particle mass flux.

1.2. DUST/SAND ELECTRIFICATION

The basic physics of saltation as outlined in the previous section is influenced by sand electrification and the resulting electric forces. This electrification of wind-blown sand and dusty phenomena, such as dust devils and dust storms, is caused by charge transfer occurring during particle collisions, such as those occurring among saltating sand particles, between saltating particles and the ground, and between sand and dust particles [*Harper*, 1967; *Lowell and Rose-Innes*, 1980; *Renno et al.,* 2003; *Lacks et al.*, 2008]. The physical mechanism that governs this charge transfer is not well understood yet (see Chapters 1.2.2 and 5), but measurements indicate that, on average, the larger particle becomes positively charged with respect to the smaller particle [*Freier*, 1960; *Schmidt et al.*, 1998; *Inculet et al.*, 2006; *Forward et al.*, 2009a]. Since the ground can be interpreted as the surface of an infinitely large plane, it is expected to charge positively with respect to saltating particles (see Chapter 3). This is indeed indicated by measurements of upward-pointing near-surface *E*-fields in saltation [*Schmidt et al.,* 1998; *Zheng et al.,* 2003; *Qu et al.,* 2004], dust devils [*Freier*, 1960; *Crozier*, 1964, 1970; *Renno et al.,* 2004], dust storms [*Stow*, 1969], and saltating snow [*Schmidt et al.,* 1999]. While the soil surface is thus expected to charge positively in dusty phenomena, the net charge on saltating particles depends on the relative frequencies of collisions with the surface (which charges them negatively) and suspended dust particles (which charges them positively). In the absence of suspended dust particles, saltating particles are thus expected to charge negatively [*Zheng et al.*, 2003].

After undergoing collisions with the surface and saltating sand, the smaller (negatively charged) dust particles can be lifted by turbulent eddies and updrafts, while the larger particles (whose charge can be either positive or negative) stay close to the positively charged surface. Figure 1.2 shows the hypothesized charge distribution in saltation and in dusty phenomena, based on the measurements reviewed in the next section.

1.2.1 Measurements of electrification in saltation and dusty phenomena

The electrification of wind-blown sand (saltation), dust devils, and dust storms has been studied in a variety of laboratory and field experiments. These studies have been

performed under Earth ambient conditions, but they also serve as analog studies of saltation and dusty phenomena on other planetary bodies, especially Mars [*Farrell et al.*, 2004; *Jackson and Farrell*, 2006]. Indeed, large *E*-fields are also predicted to occur in Martian saltation [*Melnik and Parrot*, 1998; *Farrell et al.*, 2003; *Zhai et al.*, 2006], possibly producing large quantities of hydrogen peroxide and making the Martian surface inhospitable to life as we know it [*Atreya et al.*, 2006].
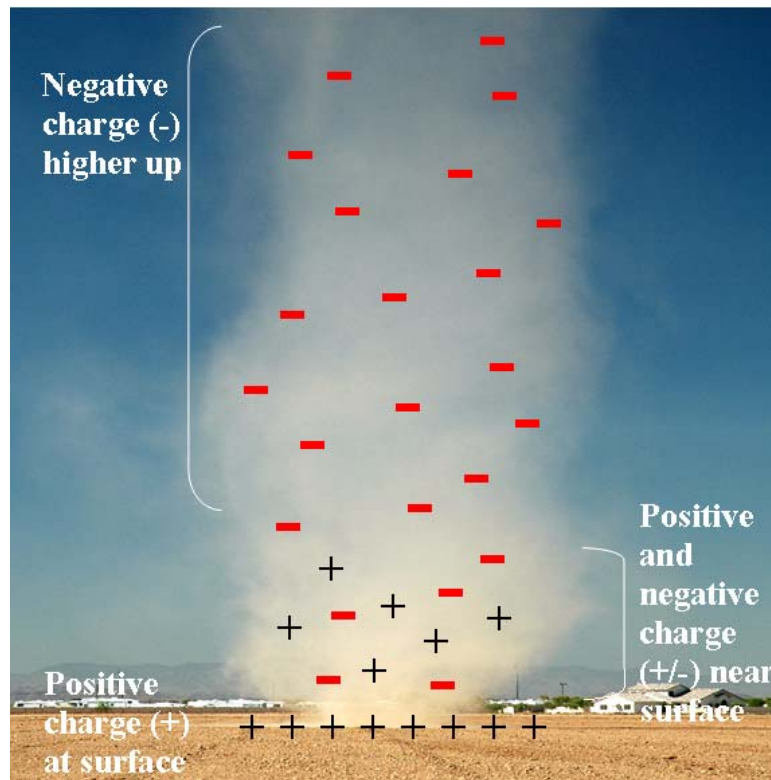
Figure 1.2: Hypothesized charge distribution in dusty phenomena (i.e., a dust storm or dust devil). Collisions with saltating particles are expected to charge the soil surface positively and dust particles negatively (see Chapter 1.2). The net charge held by saltating particles thus depends on the relative frequency of collisions with the surface and suspended dust, and can probably be both positive and negative. The small dust particles are transported upwards through convection or turbulent diffusion, while the larger and heavier saltating particles stay closer to the surface. This charge separation can produce large electric fields [e.g., *Renno et al.*, 2004; *Jackson and Farrell*, 2006; *Williams et al.*, 2009]. After *Renno and Kok* [2008].

Field measurements by *Schmidt et al.* [1998] found near-surface *E*-fields in saltation of up to 160 kV/m under moderate wind conditions. These *E*-fields were upward-pointing, indicating negatively charged saltating particles over a positively charged surface (inset of Figure 1.1). Surprisingly, a simultaneous measurement of the

6

average particle charge by *Schmidt et al.* found saltating particles at 5 cm height to be positively charged, in disagreement with their finding of upward-pointing *E*-fields increasing uniformly towards the surface. However, wind-tunnel studies by other investigators did find negatively charged saltating particles, and confirmed the finding of upward-pointing *E*-fields in saltation [*Zheng et al.*, 2003; *Qu et al.*, 2004].

A significant number of *E*-field measurements have also been made in dust devils. *Freier* (1960), who made the first of these measurements, used a grounded electric field mill to measure the *E*-field produced by a dust devil tens of meters away, and found a significant deviation from the fair-weather value. His result was consistent with the idea that dust devils have a negative dipole moment, that is that negative charges are found over positive charges (see Fig. 1.2). *Freier*'s measurements were confirmed by similar measurements by *Crozier* [1964, 1970]. More recent measurements by *Farrell et al.* [2004] and *Renno et al.* [2004] also found negative charges aloft, with measured *E*-fields exceeding the instrument range of about 10 kV/m, well before the dust devil passed over the sensors. More recently, *Jackson and Farrell* [2006] measured the horizontal *E*-field in dust devils and found values of up to 120 kV/m.

Although measurements of *E*-fields in dust devils are thus numerous, fewer measurements have been made in dust storms. However, there is anecdotal evidence of significant electrification of dust storms observed during the 'dust bowl' on the American Great Plains in the 1930s [*Keith*, 1944]. Later measurements in the Sahara found both downward-pointing [*Demon*, 1953] and upward-pointing [*Stow*, 1969] *E*-fields, with values of 1-15 kV/m at about 1 m above the ground, increasing to $50-200$ kV/m at the surface [*Stow*, 1969]. *Kamra* [1972] made a series of measurements in dust storms in the southwestern deserts of the United States and found both upward and downward-pointing *E*-fields with magnitudes similar to those measured by *Demon* [1953] and *Stow* [1969]. He also reported measurements of both positive and negative space charges at a height of 1.25 m. More recently, *Williams et al.* [2009] reported measurements during dust storms ('haboobs') in the Sahel and also found *E*-fields pointing both upwards and downwards, although most measurements indicated upward-pointing fields.

In summary, most measurements in saltation and dust devils show upward pointing *E*-fields. These measurements support the hypothesis that saltating particles charge

negatively upon colliding with the ground, and that dust particles become negatively charged after colliding with larger saltating particles (Figure 1.2). However, the situation appears to be more complex in dust storms, possibly in part because of the presence of thunderstorms, with *E*-fields pointing both upwards and downwards [*Kamra*, 1972; *Williams et al.*, 2009]. This apparent discrepancy between measurements in saltation and dust devils on the one hand, and measurements in dust storms on the other, stresses the need for a better understanding of the charging processes involved in dust/sand electrification. The current state of knowledge of this charging process is reviewed in the next section.

1.2.2 Charge transfer during dust/sand collisions

While the electrification of wind-blown sand and dusty phenomena is well-documented (see the previous section), the physical process responsible for it is still poorly understood. Indeed, although it is well-known that two objects rubbed together can become charged, this charge transfer is thought to be driven by differences in the objects' contact potential [*Harper*, 1967; *Lowell and Rose-Innes*, 1980]. Thus, little or no charge transfer would be expected when particles of identical material, such as sand and/or dust, collide. Since measurements show that significant charging does occur (see above and *Forward et al.* [2009]), a mechanism other than the 'traditional' contact electrification [*Harper*, 1967; *Lowell and Rose-Innes*, 1980] must play an important role in dust/sand electrification.

Several heuristic models to explain the mysterious triboelectric charging of identical insulators such as sand and dust have been proposed. *Lowell and Truscott* [1986b] proposed that the charge transfer is due to the presence of high-energy electrons that are 'trapped' in defect states. When collisions or rubbing brings empty low-energy states on another particle within close enough proximity, trapped high-energy electrons can tunnel to those states [*Lowell and Truscott*, 1986b]. The particle that rubs with a larger surface area during a collision, most likely the larger particle, consequently loses more of its trapped electrons and hence charges positively [*Lowell and Truscott*, 1986b]. 'Asymmetric rubbing' during collisions would thus lead to a net transfer of electrons

from larger to smaller particles, in agreement with observations [*Schmidt et al.*, 1998; *Zheng et al.*, 2003; *Inculet et al.*, 2006; *Forward et al.*, 2009].

An alternative but related model was proposed by *Lacks et al.* [2008]. They showed that, after several initial collisions in which small and large colliding particles lose roughly equal amounts of trapped electrons, smaller particles have nonetheless lost a larger fraction of their trapped electrons than larger particles have. Therefore, in subsequent collisions, smaller particles give up fewer trapped electrons than larger particles do, leading smaller particles to charge negatively and larger particles to charge positively, in agreement with the measurements discussed above.

Though the hypotheses put forth by both *Lowell and Truscott* [1986b] and *Lacks et al.* [2008] are promising, no quantitative model that describes the triboelectric charging of granular systems of identical insulators, such as wind-blown sand and dust storms, currently exists. For this reason, I develop a simple empirical charging scheme for wind-blown sand and dust in Chapter 3. This empirical scheme is constrained with measurements of *E*-fields in saltation [*Schmidt et al.*, 1998]. In Chapter 5, I use the ideas of *Lowell and Truscott* [1986b] and *Lacks et al.* [2008] to derive a more rigorous and physically-based quantitative charging scheme.

1.3 CENTRAL RESEARCH GOALS AND THESIS OUTLINE

As discussed above, this dissertation seeks to contribute to a comprehensive understanding of saltation, with emphasis on elucidating the potentially important role of sand electrification. It does so by pursuing three distinct, but related, investigations:

1. *What are the effects of electric forces on saltation and dust lifting?*

   In order to address this question, I investigate the effects of *E*-fields on the lifting of surface particles in saltation in Chapter 2. I do so by devising a simple laboratory experiment that quantifies the *E*-field at which soil particles are lifted directly by electric forces. In the subsequent chapter, I include this 'electric lifting' as well as the electric forces on saltating particles in a numerical model of saltation. I find that measurements of the height of the saltation layer can not be explained by the influential 'classical' model of saltation [*Bagnold*, 1941; *Owen*, 1964], but are consistent with our model predictions when sand electrification is

included. Since this numerical model is physically based, it can be applied to Mars. In Chapter 4, I thus apply this model to Mars and expand it to include the effects of E-fields on the ionization of CO_2 [*Delory et al.*, 2006], which limits the build-up of E-fields. I show that electric discharges are unlikely to occur in Martian saltation, and that important chemical effects produced by strong E-fields are less significant than previously thought [*Atreya et al.*, 2006; *Farrell et al.*, 2006].

2. *What are the physical processes that underlie the electrification of wind-blown sand and other granular systems of chemically identical insulating particles?*

   Since the research presented in Chapters 2, 3, and 4 supports the idea that electrification is an important component of saltation on both Earth and Mars, I develop the first quantitative theoretical model of the electrification of granular systems of chemically identical insulators, such as wind-blown sand and dust storms, in Chapter 5. Even though this model is based entirely on theoretical considerations and thus contains no empirical parameters, its predictions are both qualitatively and quantitatively consistent with measurements. This theory thus seems to provide an explanation for the hitherto puzzling phenomenon of the size-dependent charging of granular systems of identical insulators.

3. *The development of a comprehensive numerical model of saltation.*

   In Chapter 6, I describe a comprehensive numerical model of saltation that, in contrast to most previous numerical models, can simulate saltation over mixed soils. This comprehensive model is a substantial improvement over the simpler numerical model developed in Chapter 3, because it replaces many of the empirical relationships used in the latter model with physically-based relationships. Moreover, the model is the first physically-based numerical model that is capable of reproducing a wide range of field measurements of saltation. Since the model is formulated using a minimum of empirical relations, it can be easily adapted to study saltation under a variety of physical conditions, such as saltation on other planets, saltation under water, and saltating snow. This model can thus be used to study the wide range of natural processes for which saltation is a critical component.

CHAPTER 2
ENHANCEMENT OF DUST EMISSION BY ELECTRIC FORCES

2.1 INTRODUCTION

As discussed in the previous chapter, large *E*-fields have been measured in all natural dust lifting phenomena. In wind-blown sand, *E*-fields can reach up to ~160 kV/m [*Schmidt et al.,*1998], while electric fields ranging from 1 to 200 kV/m have been measured in dust devils [*Stow*, 1969; *Renno et al.*, 2004] and dust storms [*Stow,* 1969; *Qu et al.*, 2004; *Zhang et al.,* 2004].

The resulting electric forces on saltating particles can be of the order of the gravitational force [*Schmidt et al.,*1998], and can therefore affect their trajectories [*Zheng et al.*, 2003, 2006]. However, we investigate the effect of electric forces on the lifting of dust and sand particles for the first time in this chapter. We show that electric fields at the surface induce charges in soil particles. The sign of the induced charge depends on whether the electric field at the surface is upward-pointing (positive charge) or downward-pointing (negative charge). Since the charged surface particles are in the electric field that induced them, they always experience an upward-pointing electric force (see Figure 2.1) [*Jackson*, 1999]. We show that these electric forces facilitate the aerodynamic lifting of particles from the surface and can even directly lift them. Therefore, electric fields in dust phenomena increase the number of saltating particles and could thus enhance the emission of dust aerosols.

2.2 THEORY OF DUST LIFTING BY ELECTRIC FORCES

The charge separation occurring in saltation and dusty phenomena such as dust storms and dust devils produces an electric field $E_0(z)$, where z is the vertical distance from the surface. The Earth's surface is generally a good conductor because soil particles are usually covered by thin conducting films of water [*Kanagy and Mann*, 1994]. Therefore, the electric field E_0 induces charges at the surface [*Wahlin*, 1986].   A

conservative estimate of the induced surface charge density is obtained by approximating the Earth's surface to a flat plane, for which

$$\sigma_{ind} = 2E_0(0)\varepsilon_0,$$ (2.1)

where $\varepsilon_0 = 8.85 \times 10^{-12}$ F m^{-1} is the electric permittivity of air. The induced surface charges produce a second electric field, $E_{ind}(z)$. The total field $E_{tot}(z)$ is then the sum of the "original" field $E_0(z)$ and the induced field $E_{ind}(z)$. Close to the surface, the electric field $E_{ind}(z)$ is approximately that of a charged infinite plane, with charge density given by Eq. (2.1), which doubles the "original" electric field E_0

$$E_{tot}(z) \approx E_0(z) + E_{ind}(z) = E_0(z) + \frac{\sigma_{ind}}{2\varepsilon_0} = E_0(z) + E_0(0).$$ (2.2)

The electric force on soil particles protruding from the surface (Figure 2.1) can be estimated using an idealized model of a spherical, conducting particle, placed on a conducting plane. For this idealized case, the electric force is [*Lebedev and Skalskaya, 1962*]

$$F_{elec} = \frac{1.37\pi\varepsilon_0}{c_s} E_{tot}^2(0)D_p^2,$$ (2.3)

where D_p is the particle's diameter and c_s is a scaling constant that accounts for the non-sphericity of soil particles. Since the electric force increases with the particle's surface area, non-spherical particles are subject to larger electric forces than spherical particles of the same mass. Therefore, $c_s = 1$ for soils composed of perfectly spherical particles, and $0 < c_s < 1$ for real soils composed of non-spherical particles.

The upward-pointing electric force is opposed by the gravitational force (F_g)

$$F_g = \frac{\pi}{6}D_p^3\rho_p g$$ (2.4)

and the vertical component of the interparticle force (F_{ip}), that *Shao and Lu* [2000] show to be

$$F_{ip} = \beta D_p,$$ (2.5)

where $\rho_p \approx 2650$ kg/m^3 is the density of typical soil particles; $g = 9.8$ m/s^2 is the gravitational acceleration; and β is an empirical constant that scales the interparticle force and is on the order of $10^{-5} - 10^{-3}$ kg/s^2 [*Corn*, 1961; *Zimon*, 1982; *Shao and Lu*, 2000].

Soil particles are lifted when the upward electric force (Eq. 2.3) exceeds the sum of the downward gravitational (Eq. 2.4) and interparticle forces (Eq. 2.5). The theoretical threshold electric field necessary to lift a particle of diameter d is then

$$E_{thr}(d) = \sqrt{c_s \left(\frac{\beta}{1.37 \pi \varepsilon_0 D_p} + \frac{\rho_p D_p g}{8.22 \varepsilon_0} \right)}. \qquad (2.6)$$
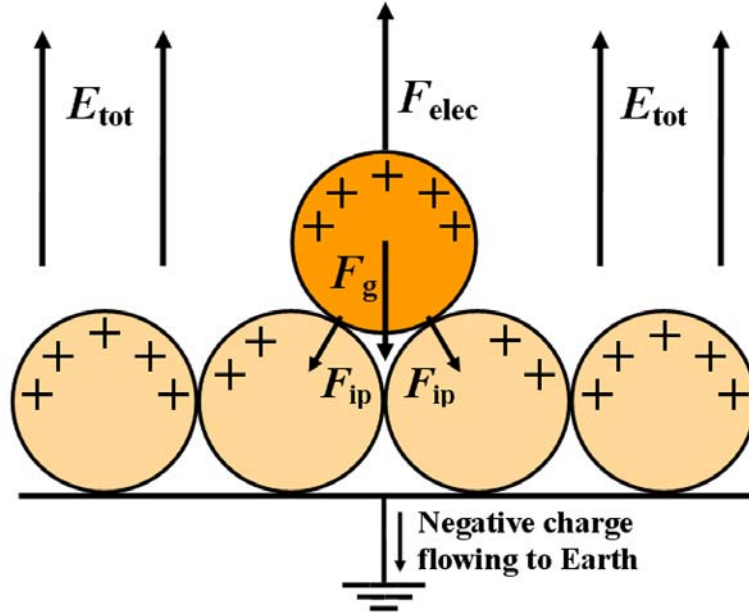
Figure 2.1: Force balance for a particle protruding from the surface. An upward (downward) pointing surface electric field (E_{tot}) can directly lift surface particles by inducing positive (negative) charges. These charged surface particles experience an upward-pointing electric force (F_{elec}). When the electric force exceeds the sum of the downward gravitational (F_g) and interparticle (F_{ip}) forces, particles are lifted from the surface. Particles protruding from the surface experience the largest electric forces, and are preferentially lifted.

2.3 EXPERIMENTAL PROCEDURE

We studied the lifting of soil particles by E-fields in the laboratory. Soil samples were collected from a field in the Sonoran desert in Arizona where dust devils and dust storms occur frequently [*Renno et al.*, 2004]. Lighter organic particles were removed from the soil samples. Fourteen samples of monodisperse (i.e., particles of similar size) mineral particles of diameters ranging from 20 to 300 μm were then wet sieved from the soil. Electron microscope images were taken to verify that each sample contained only monodisperse mineral particles (Figure 2.2). Measurements were made with both mixed (i.e., containing particles of all sizes) soil samples and monodisperse samples.

Sample soil particles were loosely deposited onto a metallic disc, with a 3.5 cm diameter, using a sieve. The soil sample was placed at the center of a parallel-plate capacitor (PPC), with dimensions of 0.4 by 0.3 m (Figure 2.3). An upward-pointing electric field E_{PPC} was generated at the center of the PPC by applying a voltage difference ΔV between the two plates,

$$E_{PPC} \approx \frac{\Delta V}{d} , \tag{2.7}$$

where the distance between the parallel plates was fixed at $d = 5$ cm. The effect of the soil sample on E_{PPC} is neglected because the sample thickness is small compared to the dimensions of the PPC.
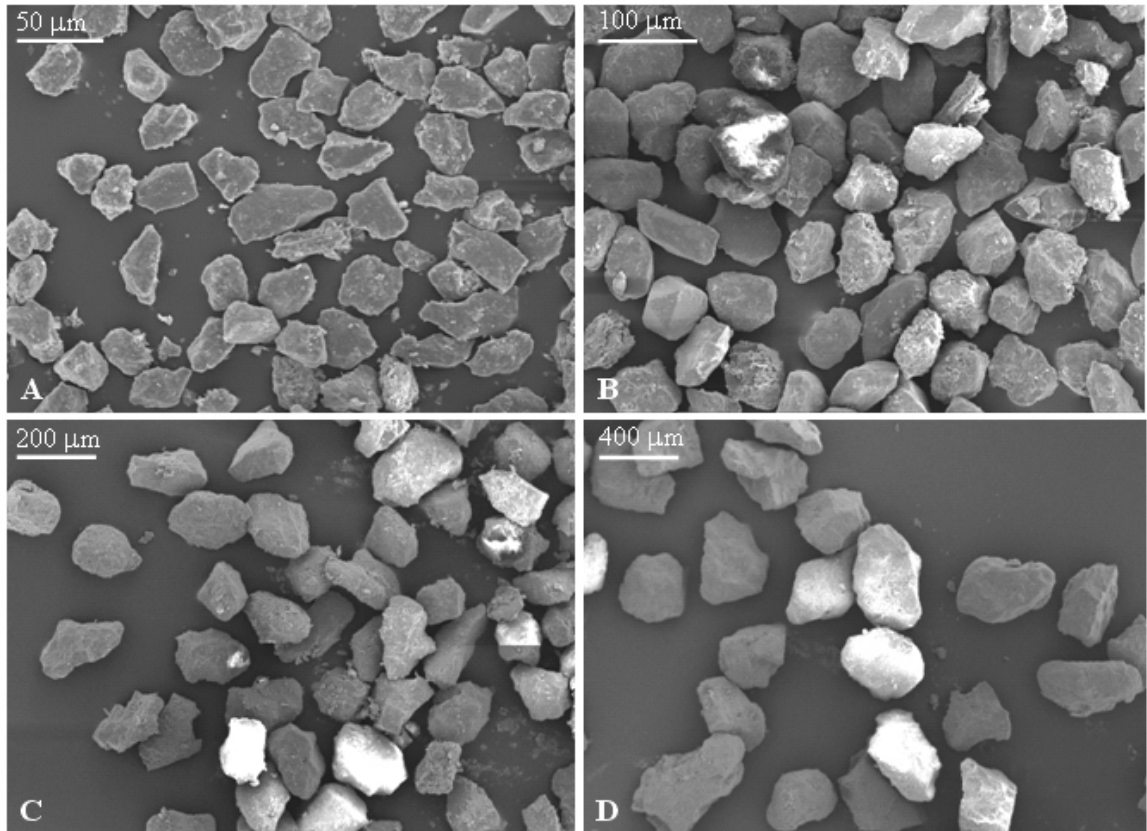
Figure 2.2: Scanning electron microscope pictures of monodisperse samples of (A) 23 μm, (B) 57 μm, (C) 111 μm, and (D) 264 μm.

14
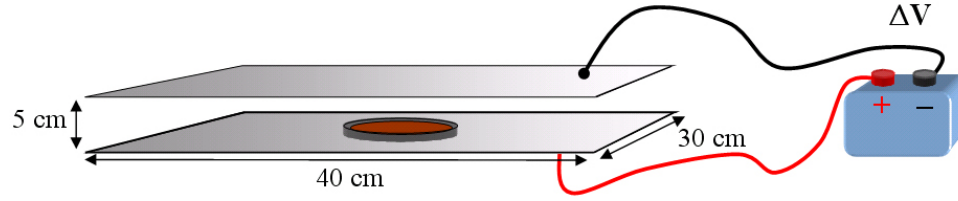
Figure 2.3: Schematic of the parallel plate capacitor (PPC) used for the experiment. The metallic disc with the soil sample has a diameter of 3.5 cm and is not drawn to scale.

We chose E_{PPC} to be upward-pointing since *Schmidt et al.* [1998] and *Zheng et al.* [2003] found upward-pointing *E*-fields near the surface during saltation. However, a downward-pointing *E*-field would similarly result in an upward force with value described by Eq. (2.3).

The E_{PPC} was increased in steps ranging from 10 to 50 kV/m until nearly all sample particles were lifted or the *E*-field reached 600 kV/m. The *E*-field was held at each value for 60 s. Sensitivity tests showed that increases in the exposure time period above 60 s does not significantly affect the results.

The amount of soil lifted by E_{PPC} was determined by weighing the soil samples before and after each incremental increase in the value of E_{PPC}, and taking the difference between the two values. The initial mass of both mixed and monodisperse samples with particles larger than 90 μm was 0.400 ± 0.003 g. Because for a fixed mass the number of particles rapidly increases with decreases in the particles' size, and because samples of small particles are difficult to handle, we used an initial mass of 0.250 ± 0.003 g for samples of monodisperse particles smaller than 90 μm. All measurements were made at a temperature of 21 ± 1 ˚C and relative humidity of 47 ± 5 %.

2.4 EXPERIMENTAL RESULTS AND ANALYSIS

Our measurements show that both monodisperse and mixed soil particles are lifted by *E*-fields of ~150-175 kV/m (Figure 2.4). Electric fields of this value have been measured in most dust lifting phenomena [*Stow et al.*, 1969; *Schmidt et al.*, 1998; *Zhang et al.*, 2004]. Measurements conducted with three different desert soil samples (not shown) yielded qualitatively similar results.

An abrupt increase in the mass of lifted soil particles occurs slightly after the *E*-field exceeds the threshold value necessary to initiate particle lifting. This abrupt

increase is partially due to particles bouncing on the top plate, colliding with the soil sample on the bottom plate, and ejecting other particles. The ejected particles then undergo a similar process, ejecting still more particles from the surface. Both this "cascading" effect and saltation involve particles impacting the surface and ejecting other particles. The cascade effect might therefore illustrate potentially important effects of electric fields on saltation. Indeed, strong electric forces in saltation facilitate the ejection of surface particles by saltating particles, resulting in an increase in particle ejections per impact of saltating particles.
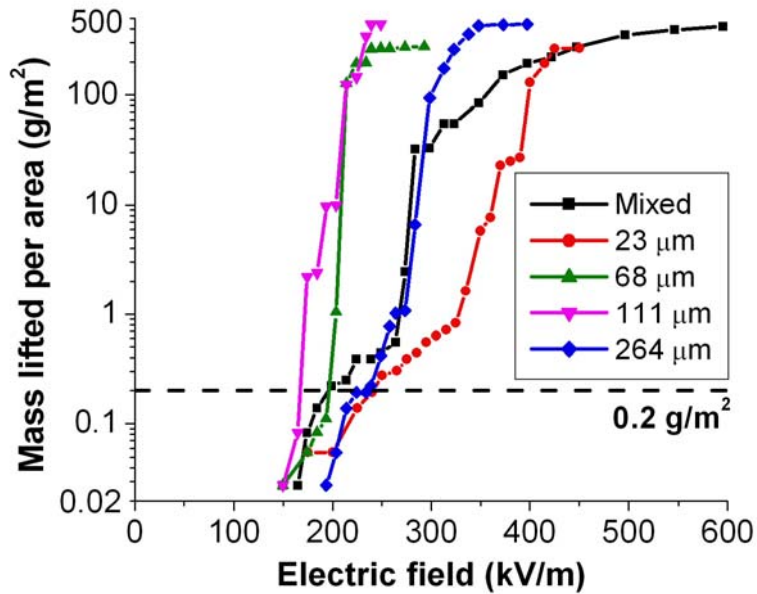
Figure 2.4: Soil mass lifted per area as a function of the applied electric field (E_{PPC}) for both mixed (solid black line) and representative monodisperse (solid colored lines) samples. The dashed black line represents the "threshold" value of 0.2 g/m^2, which we used to produce Figure 2.5. Values above ~100 g/m^2 need to be interpreted with caution, because parts of the sample were depleted of soil material. Error bars are not shown to avoid cluttering the figure. Above the measurement noise (~0.1 g/m^2), the relative errors based on the standard deviation of the mean range between 1 and 60%.

Note that our results are quantitatively valid only for the relative humidity range of 47 ± 5 %. This value is reasonable for wind-blown sand and dust storms that frequently occur when the relative humidity is between 10 and 40 % [e.g. *Jauregui*, 1989].

We define a threshold electric field (E_{thr}) as the field at which the lifting by electric forces first occurs. The threshold E-field is analogous to the concept of the threshold

friction velocity (Eq. 1.1) [*Bagnold*, 1941; *Greeley and Iversen*, 1985], which denotes the minimum surface shear stress needed for wind to move particles of a certain size. As such, the threshold friction velocity indicates the onset of saltation.

We define the threshold electric field as that which lifts 0.2 g/m^2 of monodisperse soil particles (Figure 2.5). The value 0.2 g/m^2 was chosen because it lies sufficiently above our measurement uncertainty of ~ 0.1 g/m^2 to ascertain that electric lifting has occurred. By adjusting the parameter c_s of the theoretical threshold (Eq. 2.6) to our experimental results (Figure 2.5), we obtain a semi-empirical expression for the threshold E-field

$$E_{thr} = 0.69 \sqrt{\left(\frac{\beta}{1.37 \pi \varepsilon_0 D_p} + \frac{\rho_p D_p g}{8.22 \varepsilon_0} \right)}, \tag{2.8}$$

where $\sqrt{c_s} = 0.69 \pm 0.02$ is determined by least-squares fitting of Eq. (2.6) to the data shown in Figure 2.5.
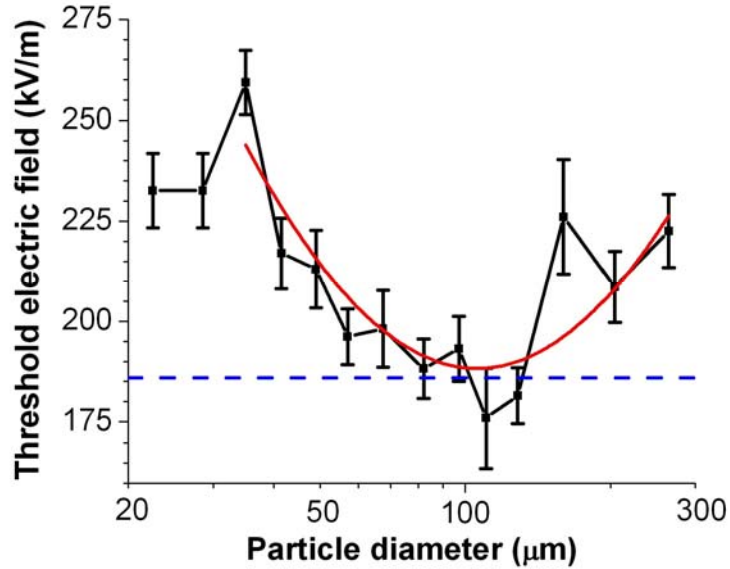
Figure 2.5: Threshold electric field at which 0.2 g/m^2 is lifted for monodisperse samples of particles of various diameters (black solid line). The error bars denote the uncertainty in determining the value of the threshold E-field and the standard deviation of the mean of four measurements for each sample. The red curve represents the least-squares fit of Eq. 2.8 to the experimental threshold electric field, corresponding to $\sqrt{c_s} = 0.69 \pm 0.02$. The blue dashed line represents the value of the electric field at which 0.2 g/m^2 of mixed sample is lifted, and has an uncertainty of ± 7.5 kV/m. The parameter β was set to 1.5×10^{-4} kg/s^2 [*Shao and Lu*, 2000].

Figure 2.5 suggests that the lifting of particles smaller than ~30 μm are poorly described by the physics underlying Eq. (2.8). This is probably because the interparticle forces of such small particles are not well understood and might thus be poorly described by Eq. (2.5) [*Zimon*, 1982; *Shao and Lu*, 2000]. A more detailed discussion is provided in Chapter 2.7. In order to determine the E_{thr} for the most easily lifted particles of diameters between ~50 and 200 μm, the data points for particles with diameters below 30 μm were omitted in the determination of c_s.

Although unable to directly lift particles, *E*-fields below E_{thr} (see Eq. 2.8) can reduce the threshold friction velocity by providing an additional upward force. We derived an equation for the threshold friction velocity that includes the effect of electric forces following the ideas proposed by *Shao and Lu* [2000], finding

$$v_{thr} = \sqrt{\frac{A_n}{\rho_{air}}\left(\rho_p g D_p + \frac{6\beta G}{\pi D_p} - \frac{8.22\varepsilon_0 E_{tot}^2(0)}{c_s}\right)}, \tag{2.9}$$

where $A_n \approx 0.0123$ is a dimensionless parameter that scales the aerodynamic forces, and G is a geometric parameter that depends on the bed stacking and is of order 1 [*Shao and Lu*, 2000]. This equation shows that *E*-fields above ~80 kV/m reduce the threshold friction velocity by more than 10 % (Figure 2.6).
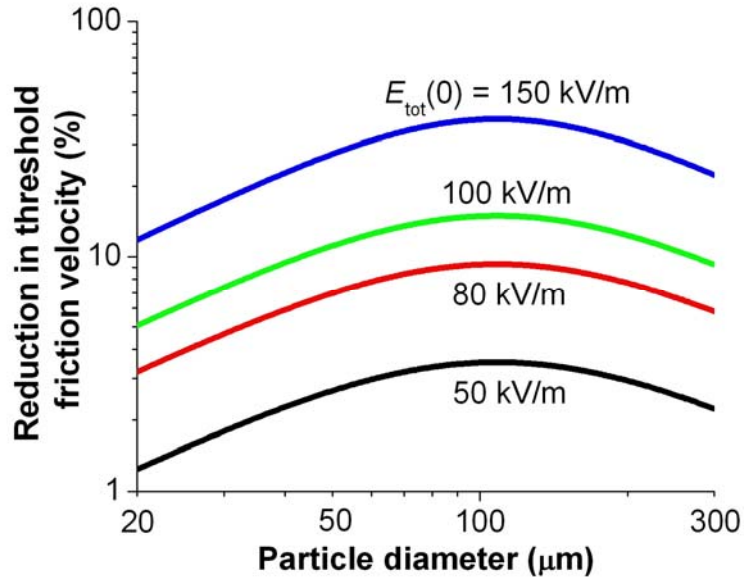
Figure 2.6: Percent reduction in the threshold friction velocity (see Eq. 2.9), as a function of particle size and surface electric field. The geometric factor G was set to 1; β was set to 1.5 × 10^{-4} kg/s^2 [*Shao and Lu*, 2000].

Momentum is transferred from the air to saltating particles, reducing the wind stress at the surface [*Bagnold*, 1941]. In steady-state saltation, the concentration of saltating particles is determined by the condition that the shear stress at the surface be just sufficient for surface particles to remain mobile [*Owen*, 1964]. Electric forces thus allow surface particles to remain mobile at a lower wind stress than in its absence. Therefore, electric forces allow saltation to equilibrate at a higher concentration of saltating particles.

2.5 CONCLUSIONS

We show that E-fields exceeding ~150 kV/m can directly lift surface particles (Figure 2.4). Additionally, we show that E-fields above ~80 kV/m considerably reduce the threshold friction velocity necessary to lift particles by wind action (Figure 2.6). Both these effects peak for particles with diameters ranging from ~50 to 200 μm. These are the particles that first undergo saltation [*Bagnold*, 1941; *Greeley and Iversen*, 1985]. Therefore, rather than directly lifting dust aerosols, E-fields modestly above ~80 kV/m intensify the saltation process that lifts mineral dust aerosols. Because electric fields in natural dust lifting phenomena can exceed 100-200 kV/m [*Schmidt et al.*, 1998; *Stow*, 1969; *Zhang et al.*, 2004], we conclude that electric forces play a potentially important role in the emission of terrestrial dust aerosols.

Electric forces might also play an important role in the lifting of dust on Mars. However, electrical break-down of the thin Martian atmosphere occurs at ~20 kV/m [*Renno et al.*, 2003], limiting bulk electric fields.

Additional studies are needed to further quantify the role of electric forces in the emission of dust aerosols. In particular, extensive measurements are necessary to assess whether strong near-surface E-fields are ubiquitous in dust lifting phenomena. If so, the incorporation of electric forces in dust lifting models could be essential for the modeling of this potentially important physical process.

2.6 ACKNOWLEDGEMENTS

Ron Miller, and an anonymous reviewer for constructive suggestions and useful discussions for improving this chapter. This research was supported by NSF award ATM 0402738 and by Rackham Applied Physics and Prins Bernhard Cultuurfonds fellowships to JK. This chapter was published as an article in *Geophysical Research Letters* [*Kok and Renno*, 2006].

2.7 APPENDIX: INTERPRETATION OF THRESHOLD ELECTRIC FIELD OF SMALL PARTICLES

The threshold *E*-field measured for monodisperse particles larger than ~30 μm agrees well with the theoretical prediction of Eq. (2.6). However, the discrepancy between theoretical and experimental results increases rapidly for particles smaller than ~30 μm (Figure 2.5). The likely reason for this discrepancy is discussed below.

The dominant force on particles smaller than 30 μm is the interparticle force (Eq. 2.5) [*Greeley and Iversen*, 1985]. Measurements indicate that the probability of a particle having a certain interparticle force follows a log-normal distribution, with the width of the distribution becoming progressively wider for smaller particles [*Zimon*, 1982]. Therefore, samples of smaller particles contain increasing numbers of particles with interparticle forces substantially smaller than that described by Eq. (2.5). These particles are lifted more easily.

Because we define the threshold electric field (Eq. 2.6) as the field for which lifting by electric forces first occurs, it is largely determined by the particles that are lifted most easily. Since Eq. (2.6) considers only the average interparticle force, the actual threshold *E*-field for small particles is expected to be lower than that predicted by Eq. (2.6).

The *E*-field necessary to lift 0.2 and 5 g/m^2 of a monodisperse sample is shown in Figure 2.7. The threshold *E*-field to lift 5 g/m^2 is in good agreement with the predictions of Eq. (2.5), even for small particles. However, the difference between the theoretical and experimental results increases for the lifting of 0.2 g/m^2, in particular for small particles. These results are consistent with our interpretation that the lower lifting threshold of particles smaller than ~30 μm is due to a widening distribution of the interparticle force for smaller particles.

20

In conclusion, the lowering of the threshold *E*-field for particles smaller than ~30 μm might be of importance to understanding the emission of dust particles from soils [*Shao*, 2000]. In the present study, however, we are mainly interested in describing the threshold *E*-field for the most easily lifted particles of diameters ~50 to 200 μm. Therefore, the "anomalous" threshold *E*-field values for particles smaller than ~30 μm were not taken into account for the derivation of Eq. (2.8).
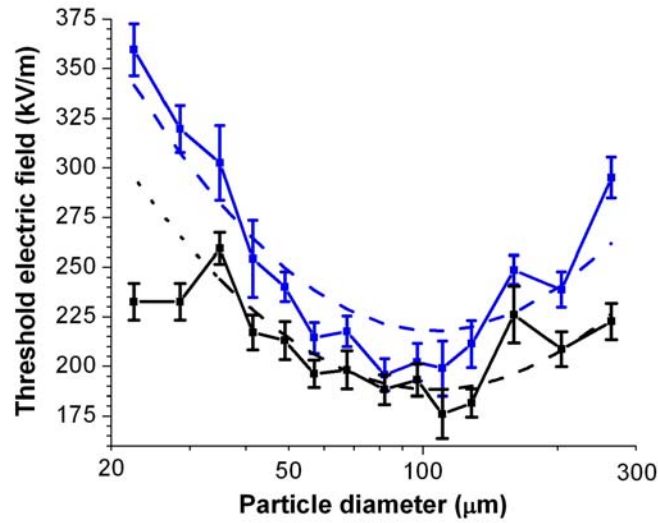
Figure 2.7. *E*-field at which 0.2 g/m^2 (black solid line) and 5 g/m^2 (blue solid line) is lifted for monodisperse samples of particles of various diameters The error bars denote the uncertainty in determining the value of the threshold electric field and the standard deviation of the mean of the four measurements taken for each sample. The black dashed curve represents Eq. (2.5), with the dotted portion of the curve denoting an extrapolation of Eq. (2.5) down to 23 μm. The blue dashed curve represents the least-squares fit of Eq. 4 to the measured electric field required to lift 5 g/m^2, with $\sqrt{c_s} = 0.80 \pm 0.02$. The parameter β was set to 1.5×10^{-4} kg/s^2 [*Shao and Lu*, 2000].

CHAPTER 3
ELECTROSTATICS IN WIND-BLOWN SAND

3.1 INTRODUCTION

It is known from industrial handling of powders that collisions between granular particles tend to leave smaller particles with net negative charge and larger particles with net positive charge [*Inculet et al.*, 2006; *Forward et al.*, 2009]. The physical mechanism governing this charge transfer is poorly understood (see Chapter 1.2.2), although various studies suggest that asymmetric rubbing (i.e., a small area of the small particle rubs over a large area of the large particle) causes a net transfer of electrons from the larger to the smaller particle [*Lowell and Truscott*, 1986]. We hypothesize that a similar process occurs in saltation, where particles bounce along the ground (Figure 1.1). Since the ground can be interpreted as the surface of an infinitely large particle, saltating particles are expected to charge negatively with respect to the surface. This is consistent with measurements of upward-pointing E-fields in wind tunnel and field experiments [*Schmidt et al.*, 1998; *Zheng et al.*, 2003; *Qu et al.*, 2004]. The occurrence of upward-pointing E-fields in dust devils and dust storms [*Freier*, 1960; *Stow*, 1969, *Renno et al.*, 2004] also suggests negatively charged particles over a positively charged surface.

The pioneering measurements of *Schmidt et al.* [1998] showed that *E*-fields of up to ~160 kV/m can be generated in saltation under moderate wind conditions. In the previous chapter, we used laboratory experiments to show that such *E*-fields facilitate the lifting of sand particles by winds, and can even directly lift sand particles from the surface. In the current chapter, we present the first physically-based numerical model of saltation that includes the generation of *E*-fields and the effects of electric forces on saltation. The model explicitly simulates the trajectories, concentration, and charging of saltating particles. We show that recent measurements in saltation [*Greeley et al.*, 1996; *Namikas*, 2003; *Rasmussen and Sorensen*, 2008] cannot be explained by classical saltation theory

[*Bagnold*, 1941; *Owen,* 1964], but are consistent with the predictions of our model when sand electrification is included.

3.2 MODEL DESCRIPTION

A detailed description of our model is given in Chapter 3.7, but we describe it here briefly. We model saltation as the interplay of four processes [*Anderson and Haff*, 1991]: (i) the motion of saltating particles, (ii) the modification of the wind profile through exchange of momentum between saltating particles and the wind flow, (iii) the collisions of particles with the soil surface, and (iv), the lifting of surface particles by wind stress and the impact of saltating particles on the surface. The main innovation of our model over previous models (e.g., [*Anderson and Haff*, 1991]) is that the charging of saltating particles during collisions with the surface and each other is included. The effect of the electric forces on particle motion and the threshold shear stress (Chapter 2) is explicitly accounted for.

We model particle motion in two dimensions by considering gravitational, fluid, and electric forces (Figure 1.1). The effects of turbulence and mid-air collisions on particle trajectories are neglected for the present study because they are relatively small for typical shear velocities [*Anderson and Haff*, 1991; *Shao*, 2000]. Results of laboratory and numerical studies are used to model the collision of particles with the surface, including the ejection of surface particles [*Anderson and Haff*, 1991].

For the calculation of the wind profile, we make the classical assumption that, in steady-state saltation, the fluid shear stress at the surface stays at the threshold value (τ_t) necessary to initiate the motion of surface particles [*Owen,* 1964]. The particle concentration per unit area is then given by

$$N = \tau_\mathrm{p}(0)/\overline{\tau_\mathrm{sp}(0)} = (\tau - \tau_\mathrm{t})/\overline{\tau_\mathrm{sp}(0)}, \tag{3.1}$$

where $\tau_\mathrm{p}(0)$ is the total shear stress exerted by saltating particles at the surface, and $\overline{\tau_\mathrm{sp}(0)}$ is the average surface stress exerted by a single saltating particle, as computed from the particle trajectories. The size distribution of saltating particles is assumed to be similar to that of the parent soil for particles of $100\text{-}500\,\mu\mathrm{m}$, in agreement with field measurements (see Chapter 3.7).

3.3 SAND ELECTRIFICATION

The model accounts for electrostatic charging of saltating particles during collisions with each other and the surface. Although collisional charge transfer between grains of granular material is observed in a variety of physical systems [*Freier*, 1960; *Stow*, 1969; *Schmidt et al.*, 1998; *Inculet et al.*, 2006; *Forward et al.*, 2009], the charging mechanism is not well understood (see chapter 1.2.2). Nonetheless, *Desch and Cuzzi* [2000] proposed a model in which the collisional charge transfer depends on the pre-existing charges, the particle sizes, and the difference in the particles' contact potential. They proposed that

$$q'_S = C_1(q_S + q_L) - C_2\Delta\Phi; \quad q'_L = (1 - C_1)(q_S + q_L) + C_2\Delta\Phi \qquad (3.2)$$

where q_S and q_L are the charges of the smaller and larger particles before the collision, q'_S and q'_L are the charges after the collision, $\Delta\Phi$ is the difference in particle contact potential, and C_1 and C_2 are functions of the mutual capacitances of the two particles, as defined by equations 5-10 of *Desch and Cuzzi* [2000]. For particles of similar composition (i.e., $\Delta\Phi = 0$), such as typical soil particles, Eq. (3.2) suggests that no charge transfer occurs when the colliding particles are not initially charged, which contradicts observations [*Freier*, 1960; *Stow*, 1969; *Schmidt et al.*, 1998; *Zheng et al.*, 2003; *Qu et al.*, 2004; *Forward et al.*, 2009]. To mitigate this problem, we propose an effective contact potential difference between particle pairs of similar composition but with different sizes. That is,

$$\Delta\Phi_{eff} = S(R_L - R_S)/(R_L + R_S), \qquad (3.3)$$

where S (in Volts) is a physical parameter that scales the collisional charge transfer, and R_S and R_L are the radii of the small and large particles. This simple model has the functional form expected from observations – smaller particles acquire net negative charge during collisions with larger particles, and the charge transfer is reduced as the relative difference in particle size decreases. Since saltating particles impacting the soil surface tend to interact with multiple surface grains [*Bagnold,* 1941; *Anderson and Haff*, 1991], we interpret the soil surface as the surface of an infinitely large particle (i.e., $R_L = \infty$). We determined S by calibrating the model with *E*-field measurements in saltation [*Schmidt et al.*, 1998], and found that $S = 6 \pm 4$ Volts (see Figure 3.1).

The soil surface is assumed to be conducting, both because charge exchange with saltating particles provides charge mobility, and because conducting films of water are generally adsorbed onto soils (Chapter 2). Since the height to which particles saltate is generally much smaller than the horizontal extent over which saltation occurs, we use the infinite plane approximation to determine the electric field E from the calculated space charge density ρ_c and soil surface charge density σ (Chapter 2),

$$E(z) = \frac{1}{2\varepsilon_0} \left(\sigma + \int_0^z \rho_c(z') dz' - \int_z^\infty \rho(z') dz' \right), \qquad (3.4)$$

where ε_0 is the electric permittivity of air.
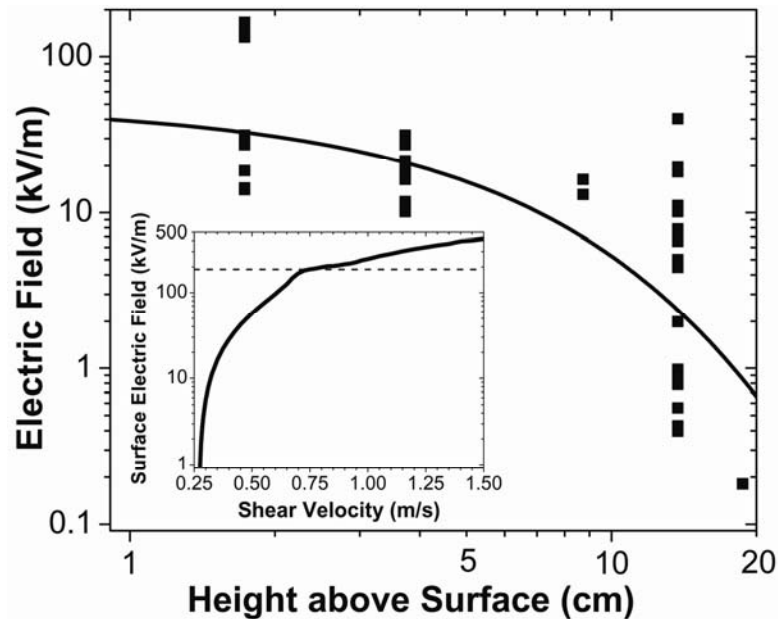
Figure 3.1: Comparison of measured (squares) and modeled (solid line) *E*-fields in saltation. The measurements [*Schmidt et al.*, 1998] were taken for winds of 4 – 12 m/s at 1.5 m height, which was estimated to correspond to an average shear velocity of 0.5 ± 0.1 m/s [*Shao*, 2000]. The soil particle size distribution was taken as typical for the broad top of a dune [*Lancaster*, 1986], where the measurements were made. The inset shows the dependence of the surface *E*-field on shear velocity for the size distribution reported in *Namikas* [2003], with the dashed line corresponding to the experimental electric lifting threshold (Chapter 2).

3.4 MODEL RESULTS

Detailed comparisons of vertical and horizontal profiles of the mass flux in saltation show that predictions of our model are in agreement with measurements (Figures 3.2 and 3.3). To the best of our knowledge, the model presented here is the first physically-based

model capable of accurately reproducing observed particle mass flux profiles. For high shear velocity, the agreement with field measurements improves when electric forces are included (Figure 3.2c). The height-integrated mass flux predicted by our model is also in good qualitative agreement with wind tunnel results (see Chapter 3.7).
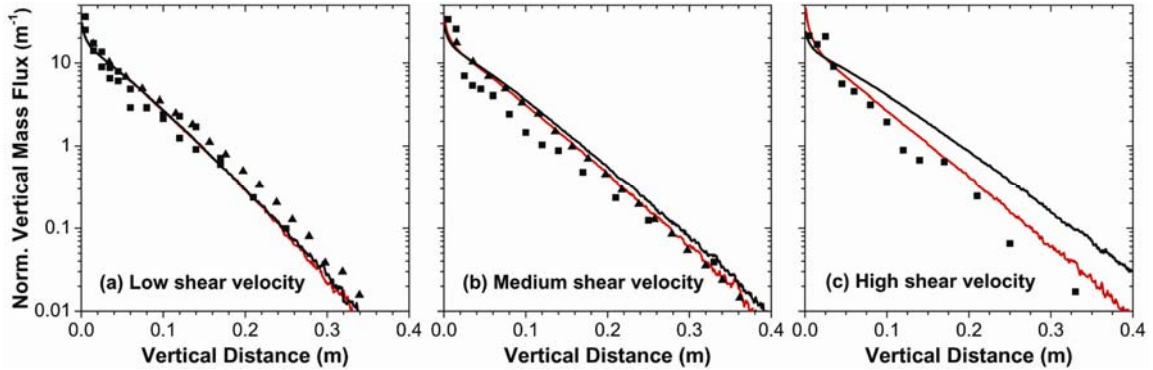
Figure 3.2: Vertical profiles of saltation mass flux from field measurements (squares [*Namikas*, 2003] and triangles [*Greeley et al.*, 1996]), and model predictions with and without electric forces (red and black solid lines, respectively). Both measured and modeled mass flux profiles are normalized by their total mass flux to simplify comparison. Results are shown for (a) low shear velocity ($u^* = 0.32$ m/s), (b) medium shear velocity ($u^* = 0.47$ m/s) and (c) high shear velocity ($u^* = 0.63$ m/s). Model results were obtained for the size distribution reported in *Namikas* [2003].
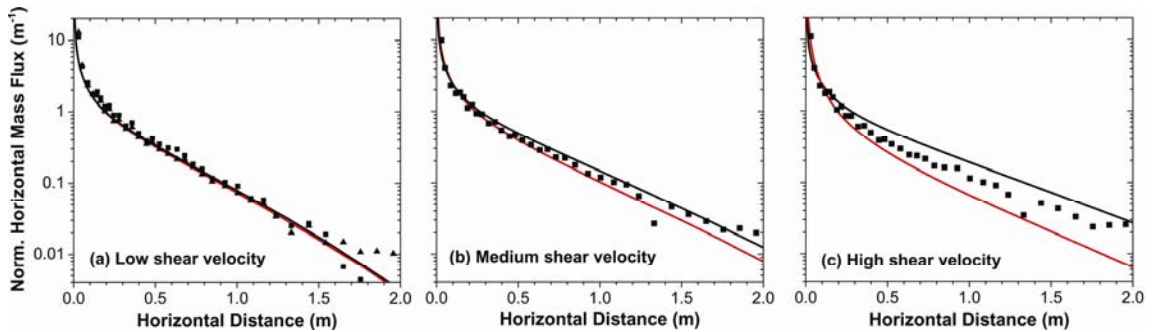
Figure 3.3: Horizontal profiles of saltation mass flux measured in field experiments (squares [*Namikas*, 2003]), and compared to model results with and without electric forces (red and black solid lines, respectively). Both measured and modeled mass flux profiles are normalized by their total mass flux to facilitate comparison. Results are shown for (a) low shear velocity ($u^* = 0.32$ m/s), (b) medium shear velocity ($u^* = 0.47$ m/s) and (c) high shear velocity ($u^* = 0.63$ m/s). Model results were obtained for the size distribution reported in *Namikas* [2003].

Our model predicts that *E*-fields increase sharply towards the surface and with wind speed (Figure 3.1), in agreement with measurements [*Schmidt et al.*, 1998; *Zheng et al.*, 2003; *Qu et al.*, 2004]. The surface *E*-field is of particular interest, because *E*-fields larger than ~80 kV/m significantly reduce the wind shear stress necessary to lift surface

particles (Chapter 2). Our model shows that electrification approximately doubles the concentration of saltating particles for large shear velocities (Figure 3.4).
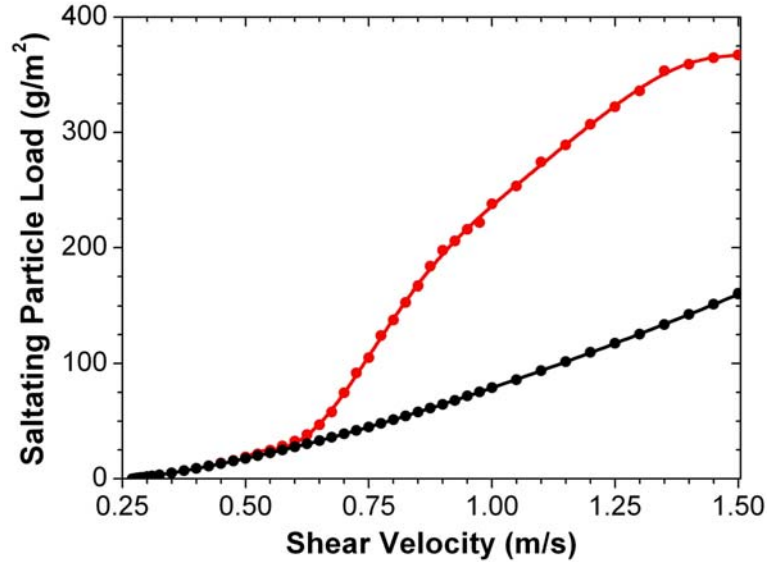
Figure 3.4: Mass load of saltating particles simulated with electric forces (red line) and without (black line) as a function of shear velocity, for the size distribution reported in *Namikas* [2003]. Electric forces cause the saltation particle load to increase at a given shear velocity by reducing the wind shear stress required to lift surface particles (Chapter 2) and by reducing the average wind momentum absorbed by each particle (see text).

In addition to increasing the concentration of saltating particles, electric forces also affect particle trajectories. The characteristic height of saltation can be taken as the height z_{50} below which 50 % of the mass transport occurs. Classical saltation theory [*Bagnold*, 1941; *Owen*, 1964] predicts that increases in wind speed produce increases in the momentum of saltating particles, causing them to impact and rebound from the surface at higher speed, and therefore reach larger heights. However, recent measurements show that z_{50} stays approximately constant as the wind speed increases [*Greeley et al.*, 1996; *Namikas*, 2003; *Rasmussen and Sorensen*, 2008]. This clear discrepancy between measurements and theory can be resolved by the inclusion of sand electrification in our physically based saltation model (Figure 3.5). As the negatively charged saltating particles bounce along the positively charged surface (Figure 1.1) [*Schmidt et al.*, 1998; *Zheng et al.*, 2003; *Qu et al.*, 2004], the downward electric force causes particles to travel closer to the surface and at reduced horizontal speed. The downward electric force on the saltating particles also increases with wind speed, forcing z_{50} to remain approximately

constant up to moderate shear velocities, in good agreement with measurements [*Greeley et al.*, 1996; *Namikas*; 2003; *Rasmussen and Sorensen*, 2008]. At larger shear velocities, electric forces become strong enough to lower the threshold shear velocity (Chapter 2). This reduces the near-surface winds and z_{50}. Note also that the decrease in particle speed due to electric forces reduces the average surface stress exerted by a single saltation particle ($\overline{\tau_{sp}(0)}$ in Eq. (3.1)), which contributes to the increase in particle concentration seen in Fig. 3.4.
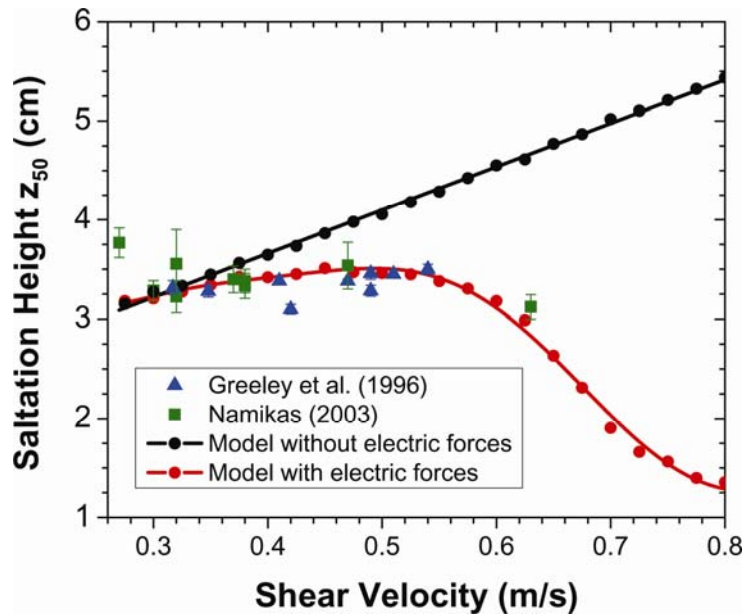
Figure 3.5: Dependence of the characteristic saltation height z_{50} (see text) on the wind shear velocity. Classical saltation theory predicts that z_{50} increases strongly with shear velocity [*Bagnold*, 1941; *Owen*, 1964], which our model also predicts when electric forces are not included (black circles). However, field measurements (squares [*Namikas*, 2003] and triangles [*Greeley et al.*, 1996]) show that z_{50} remains approximately constant. Inclusion of sand electrification in our model (red circles) resolves this discrepancy. Values of z_{50} were obtained from *Greeley et al.* [1996] and *Namikas* [2003] by fitting an exponential function to the measured vertical mass flux profiles, as described in *Namikas* [2003]. Error bars represent the uncertainty in the fitting parameters. Model results were obtained for the size distribution reported in *Namikas* [2003].

The linear increase in z_{50} when sand electrification is not included in our model is consistent with results from an independent numerical model [*Almeida et al.*, 2006]. This model includes effects of turbulence and assumes that the trajectories of all saltating

particles are similar. The agreement between the results of these two different models suggests that they are robust.

3.5 CONCLUSIONS

We developed the first physically based numerical saltation model that includes the effects of sand electrification. Significant discrepancies exist between predictions of classical saltation theory and field measurements [*Namikas*, 2003]. We show that inclusion of sand electrification in saltation models can resolve these discrepancies.

The model predictions are in good agreement with measurements of the flux of saltating particles (Figures 3.2 and 3.3). Model results show that sand electrification increases the concentration of saltating particles at a given wind shear velocity (Figure 3.5; Chapter 2). Moreover, the downward electric force on the saltating particles lowers their trajectories, improving the agreement between model predictions and measurements (Figure 3.5) [*Greeley et al.*, 1996; *Namikas*, 2003; *Rasmussen and Sorensen*, 2008].

Our results thus suggest that sand electrification is an important part of the physics of wind-blown sand.

3.6 ACKNOWLEDGEMENTS

3.7 APPENDIX: DETAILED MODEL DESCRIPTION

A schematic overview of our model is given in Figure 3.6. Following previous studies, we model saltation as the interplay of four processes [*Anderson and Haff*, 1991]: (i) the motion of saltating particles, (ii) the modification of the wind profile through momentum transfer between the wind flow and saltating particles, (iii) the collisions of particles with the surface, and (iv) the lifting of surface particles by wind stress and the impact of saltating particles with the surface. In addition to these four critical processes,

we also simulate the charging of saltating particles during collisions with other particles and the surface (see Section 3.3). The effect of electric forces on particle motion and on the critical wind speed required to lift them from the surface (Chapter 2) is calculated explicitly. Due to their interdependence, the wind profile, the electric field, and the saltating particles' motion, concentration, and charge, are calculated iteratively until steady state is reached (see Figure 3.6).

3.7.1 Equations of motion

As in previous studies [*Anderson and Haff*, 1991; *McEwan and Willetts*, 1991; *Shao and Li*, 1999], we model the motion of saltating particles in two dimensions. For simplicity, we neglect the effects of turbulence and mid-air collisions on particle trajectories, because these effects are relatively small for typical shear velocities [*Anderson and Haff*, 1991; *Shao*, 2000].
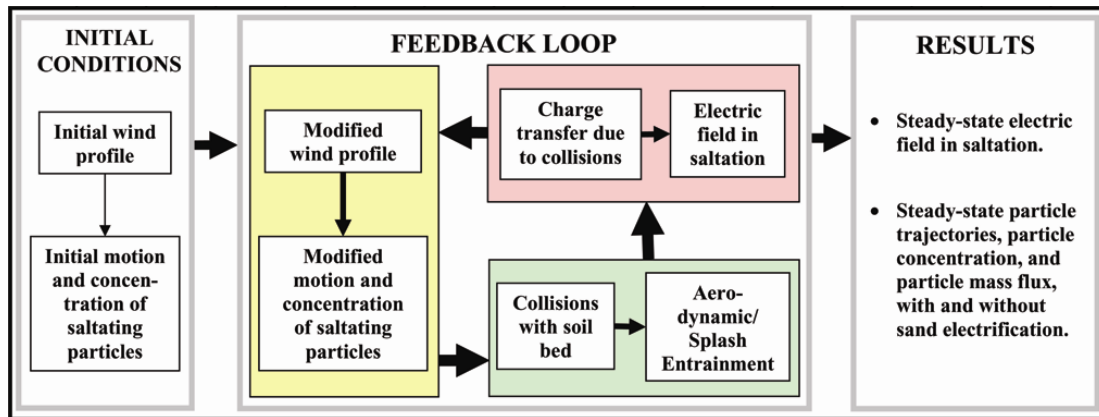
Figure 3.6: Schematic diagram of our physically based saltation model. As in previous studies [*Anderson and Haff*, 1991; *McEwan and Willetts*, 1991; *Shao and Li*, 1999], saltation is modeled by explicitly simulating (i) particle trajectories, (ii) the absorption of momentum from the wind by these particles, (iii) the collision of particles with the soil surface, and (iv) the creation of new saltating particles by aerodynamic entrainment and the ejection of surface grains by saltating particles striking the soil surface. In addition to these four critical processes, our model also includes sand electrification and the effects of electric fields on saltation (see Chapter 3.3). The steps indicated in the feedback loop are repeated until the changes in the saltation trajectories, the wind profile, and the electric field are smaller than a specified value in successive iterations.

In addition to including fluid drag and gravitational forces as in previous models [*Anderson and Haff*, 1991; *McEwan and Willetts*, 1991; *Shao and Li*, 1999; *Shao*, 2000], we also include the effects of electric forces (see chapter 3.3) on particle trajectories. Additionally, we include the fluid lift force, which is mainly important close to the

surface [*Anderson and Hallet*, 1986]. The motion of saltating particles is then described by

$$ma_x = \frac{\pi D_p^2}{8} \rho_a C_d |V_R|(U - v_x), \text{ and} \tag{3.5a}$$

$$ma_z = \frac{\pi D_p^2}{8} \rho_a \left[-C_d |V_R| v_z + C_l \left(U_{top}^2 - U_{bot}^2 \right) \right] - mg + qE , \tag{3.5b}$$

where m, q, and D_p are the particle's mass, charge and diameter, respectively; a_x and a_z are the particle accelerations in the x and z directions; v_x and v_z are the particle speeds in the x and z directions; V_R is the vector difference between the particle and wind velocities; U is the horizontal wind speed, and U_{top} and U_{bot} are the wind speeds at the top and bottom of the particle, respectively; ρ_a is the air density; g is the gravitational acceleration; and E is the electric field at the particle's position. We calculate the drag coefficient C_d using the Reynolds number [*Morsi and Alexander*, 1972] of the saltating particle, assuming that it has the shape of natural sand particles, for which we take the characteristic length scale as $0.75D_p$ [*Anderson and Hallet*, 1986; *Bagnold*, 1935; *Namikas*, 2003]. The lift coefficient C_l is taken as $0.85C_d$ [*Chepil,* 1958]. The equations of motion (Eq. 3.5) are integrated numerically for the calculation of the trajectories of the saltating particles.

3.7.2 Wind profile

The initial trajectories of saltating particles are calculated using the logarithmic wind profile formed by a turbulent fluid flowing over a no-slip surface [*Prandtl*, 1935],

$$U(z) = \frac{u^*}{\kappa} \ln\left(\frac{z}{z_0} \right), \tag{3.6}$$

where $\kappa = 0.4$ is the von Karman constant, z is the vertical distance from the surface, and $z_0 \approx 2D_p/30$ is the aerodynamic surface roughness [*Sherman*, 1992]. As in previous investigations [*Anderson and Hallet*, 1986; *Anderson and Haff*, 1991; *McEwan and Willetts*, 1991; *Shao and Li*, 1999], the wind flow is assumed to be horizontal.

The initial wind profile given by Eq. (3.6) is modified by the transfer of momentum and shear stress between the wind flow and saltating particles. The fluid shear stress is given by [*Shao*, 2000]

$$\tau_a(z) = \rho_a \left[\kappa z \frac{\partial U(z)}{\partial z} \right]^2. \tag{3.7}$$

Outside the near-surface layer where saltation takes place (the 'saltation layer'), the fluid shear stress is a constant given by [*Shao*, 2000; *Owen*, 1964]

$$\tau = \rho_a u^{*2}, \tag{3.8}$$

where u^* is the wind shear velocity. *Owen* [1964] showed that the shear stress due to saltating particles (τ_p) and the fluid shear stress in the saltation layer (τ_a) sum to the fluid shear stress outside the saltation layer (τ). That is,

$$\tau = \tau_a(z) + \tau_p(z), \tag{3.9}$$

where [*Shao*, 2000]

$$\tau_p(z) = \sum_i m_i v_x^i(z) - \sum_j m_j v_x^j(z), \tag{3.10}$$

and where the subscripts i and j respectively sum over all descending and ascending particles that pass the height z per unit area and unit time.

Owen [1964] further hypothesized that the fluid shear stress at the surface remains at 'a value just sufficient to ensure that the surface grains are in a mobile state'. That is,

$$\tau_a(0) \approx \tau_t, \tag{3.11}$$

where τ_t denotes the threshold shear stress (critical value) necessary to initiate the motion of surface particles. Although Owen's hypothesis has not been fully verified [*Shao*, 2000], it has been widely used in analytical (e.g. [*Raupach*, 1991, *Li et al.*, 2004]) and numerical (e.g., [*Shao and Li*, 1999; *Sauermann et al.*, 2001]) studies. We also use it, because it greatly simplifies the computation of both the wind profile and the concentration of saltating particles.

Since Eq. (3.11) describes one of the main assumptions in our model, we briefly explain the reasoning behind it. *Owen* [1964] argued that the fluid shear stress at the surface should remain at the threshold for particle entrainment because if the surface shear stress falls below this critical value, fewer particles are entrained by wind. This reduces the transfer of momentum between saltating particles and the wind flow, thereby increasing the surface shear stress back to its critical value. Conversely, if the surface shear stress exceeds the critical value, more particles are entrained, again restoring the surface shear stress to its critical value. Owen derived his hypothesis on the assumption

32

that surface particles are predominantly lifted by aerodynamic forces. That is, by assuming that the ejection of surface grains by saltating particles impacting the soil surface ('splashing') is negligible. However, a numerical model developed by *Anderson and Haff* [1991] predicts that the splashing of grains is the predominant method of particle entrainment in saltation. Nonetheless, they found that the fluid shear stress at the surface remains somewhat below the threshold shear value. *Raupach* [1991] argued that this result indicated that Owen's hypothesis is a reasonable approximation.

Limited experimental support for Owen's hypothesis was given by *Gillette et al.* [1998]. They found good agreement between field measurements and an analytical model of the aerodynamic roughness length in saltation that employs Owen's hypothesis [*Raupach*, 1991]. The numerical study by *Shao and Li* [*1999*] provided further support for Owen's hypothesis. This study found that splashing of grains only becomes important for large shear velocities, in disagreement with the earlier study of *Anderson and Haff* [1991].

Using Owen's hypothesis, the concentration of saltating particles can be calculated in a straightforward manner. By combining Eqs. (3.9) and (3.11), we find that the particle shear stress at the surface equals

$$\tau_p(0) = \tau - \tau_t. \tag{3.12}$$

The concentration of saltating particles per unit area is then

$$N = \frac{\tau_p(0)}{\overline{\tau_{sp}}(0)} = \frac{\tau - \tau_t}{\overline{\tau_{sp}}(0)}, \tag{3.13}$$

where $\overline{\tau_{sp}}(0)$ is the average shear stress that a single saltating particle exerts at the surface. With the concentration and trajectories of particles known, the particle shear stress at all heights ($\tau_p(z)$) is calculated. The fluid shear stress ($\tau_a(z)$) is then directly obtained through Eq. (3.9), and used to numerically integrate Eq. (3.7) to obtain the wind profile.

3.7.3 Particle collisions with the surface

The collision of saltating particles with the surface is an essential process in saltation [*Anderson and Haff*, 1991, *Shao*, 2000]. The experimental study of *Mitha et al.*

33

[1986] indicated that saltating particles have a probability of ~94 % of rebounding upon collision with the soil surface. The numerical study of *Anderson and Haff* [1991] investigated the rebound probability (P_{reb}) in more detail and found that

$$P_{reb} = 0.95[1 - \exp(-\gamma v_I)], \tag{3.14}$$

where $\gamma \approx 2$ m^{-1}s is a constant, and v_I is the speed with which the particle impacts the surface. Eq. (3.14) is consistent with the result of *Mitha et al.* [1986] for large impact speeds. Moreover, it predicts a decreasing chance of rebound for low impact speeds, as would be expected. We thus use Eq. (3.14) to calculate the chance of an impacting particle to rebound from the surface.

Results of laboratory and numerical studies [*White and Schulz*, 1977; *Mitha et al.*, 1986; *Anderson and Haff*, 1991; *McEwan and Willetts*, 1991; *Nalpanis et al.*, 1993; *Rice et al.*, 1995; *Rioual et al.*, 2000] are used to describe the velocity of particles rebounding from the surface as a normal distribution centered at 55 % (± 20 %) of the particle's impact speed, at an angle of 35º (± 15º) from horizontal.

The model calculates the charge transfer of rebounding particles with the soil surface using Eqs. (3.2) and (3.3). The charge of particles that do not rebound from the surface is added to the total charge held by the soil surface.

3.7.4 Lifting of surface particles

In steady-state saltation, the loss of saltating particles through Eq. (3.14) must be balanced by the ejection of new particles from the surface, either through aerodynamic entrainment or through splashing. Using Eq. (3.14), the model calculates the total number of particles that do not rebound, per unit area and unit time. In steady-state, this loss of saltating particles must be balanced by the sum of aerodynamically entrained and splashed particles. That is,

$$N_{nr} = N_a + N_s, \tag{3.15}$$

where N_{nr} is the number of non-rebounding particles per unit time and unit area, N_a (m^{-2}s^{-1}) is the number of aerodynamically entrained grains, and N_s (m^{-2}s^{-1}) is the number of splashed grains.

The aerodynamic entrainment of grains has been poorly studied, while the splashing of surface grains by impacting saltating particles has been investigated by several studies

[*Anderson and Haff*, 1991; *McEwan and Willetts*, 1991; *Rice et al.*, 1996; *Rioual et al.*, 2000]. These studies found consistently that, for particles impacting a surface of similar particles, the number of ejected particles per collision (n_s) varies approximately linearly with the speed of the impacting particle. Thus,

$$n_s \approx A v_I, \tag{3.16}$$

where conservation of momentum allows the constant A (m^{-1}s) to be rewritten as

$$A = a \frac{m_I}{m_{bed}}, \tag{3.17}$$

where a (m^{-1}s) is a constant, m_I is the mass of the impacting particle, and m_{bed} is the average mass of particles in the soil surface. For loose sand, we find that $a \approx 0.42$ m^{-1}s by fitting Eq. (3.17) to the experimental results reported in *McEwan and Willetts* [1991]. Then,

$$N_s = \sum_j n_s^j = \frac{a}{m_{bed}} \sum_j m_I^j v_I^j, \tag{3.18}$$

where j sums over all particles impacting the soil surface per unit area and unit time. Again using the result of laboratory and numerical studies, we describe the speed of splashed particles as a normal distribution centered at 8 % (± 4 %) of the speed of the impacting particle, at an angle of 55º (± 25º) from horizontal [*Anderson and Haff*, 1991; *McEwan and Willetts*, 1991; *Rice et al.*, 1996].

With N_s known, the number of aerodynamically entrained particles (N_a) is found using Eq. (3.15). A plausible assumption [*Anderson and Haff*, 1991; *Shao and Li*, 1999] is that the vertical component of the lift-off speed (v_a) of these particles can be described by an exponential distribution

$$P(v_a) = \frac{\exp(-v_a / \overline{v_a})}{\overline{v_a}}, \tag{3.19}$$

where we assume that the average vertical lift-off speed $\overline{v_a} = \sqrt{8 g D_p}$. Neglecting non-gravitational forces, a particle with vertical speed $\overline{v_a}$ would thus rise four particle diameters above the soil surface, which is a reasonable estimate [*Anderson and Haff*, 1991]. We further assume that particles lift off at an angle similar to that of splashed

particles (see above). The results reported in this chapter are mostly insensitive to the details of the parameterization of the lift-off of aerodynamically entrained grains.

The charge of surface grains lifted by aerodynamic entrainment or splashing is taken as their projected area ($\pi D_p^2 / 4$) times the soil surface charge density (σ).

3.7.5 Size distribution of saltating particles

Previous numerical models have focused mostly on saltation over soil surfaces made up of homogenous particles [*Anderson and Haff*, 1991; *McEwan and Willetts*, 1991; *Shao and Li*, 1999]. We here extend our model to include saltation over soil surfaces composed of mixed particles, which is a better representation of natural conditions.

Several studies have found that the size distribution of saltating particles is similar to that of the parent soil [*Gillette and Walker*, 1977; *Gillette et al.*, 1980, 1999]. A likely reason for this similarity is that saltation is the dominant process in the formation of dune and beach sands, and therefore they contain particles that can be readily transported by saltation. More specifically, measurements by *Namikas* [2003, 2006] show that the saltating particle size distribution is somewhat biased towards smaller particles, and shifts slightly towards larger particles with increasing shear velocity (Fig. 3.7). This probably happens because the wind shear velocity determines the size of the largest particles that can saltate. For simplicity, we assume that the saltating particle size distribution is identical to that of the parent soil for particles of 100-500 μm. This approximation is justified by the similarity between the size distributions of the saltating particles and the parent soil in this size range (Fig. 3.7 and [*Gillette and Walker*, 1977; *Gillette et al.*, 1980, 1999]).

3.7.6 Charge transfer during mid-air collisions

Although the effect of mid-air collisions on particle trajectories is neglected as explained, the model does account for the charge transfer during these collisions (see Section 3.3). The chance ΔP_λ that a given saltating particle will collide with a particle in particle bin j in the model time step Δt is given by

$$\Delta P_\lambda \left(z, \vec{v} \right) = \Omega^j \rho^j \Delta v^j \Delta t , \qquad (3.20)$$

where z and $\vec{v}$ are the position and velocity of the saltating particle, ρ^j is the density (in m^{-3}) of particles in bin j at the saltating particle's location, and Δv^j is the average magnitude of the relative velocity with particles in bin j. The collisional cross section Ω^j is given by

$$\Omega^j = \frac{\pi}{4}(D_p + D_p^j)^2 , \qquad (3.21)$$

where D_p^j is the diameter of particles in bin j.
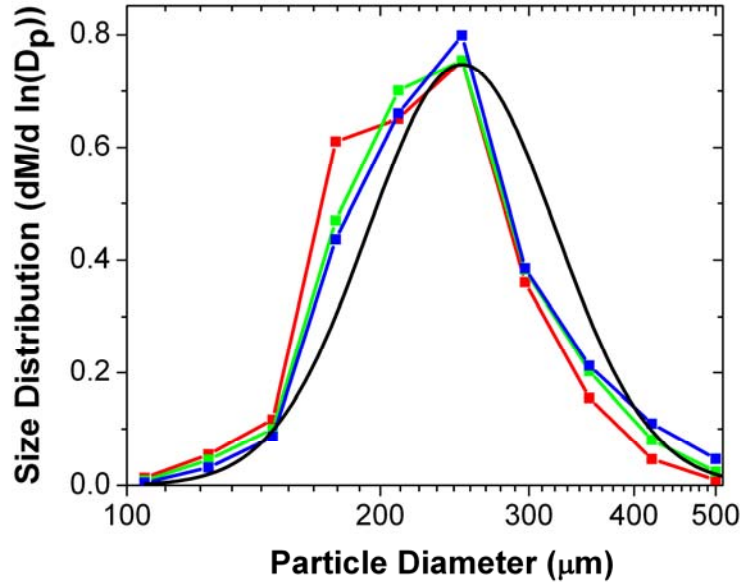
Figure 3.7: Measured saltating particle size distributions for shear velocities of $u^* = 0.30$, 0.36, and 0.55 m/s (red, green, and blue lines, respectively), where M represents the fractional contribution to the size distribution. The parent soil size distribution (black line) is plotted for comparison [*Namikas*, 2003]. Saltating particle size distributions were obtained from Figure 3 in *Namikas* [2006].

The transfer of charge between the colliding particles is modeled using Eqs. (3.2) and (3.3).

3.7.7 Reduction of threshold shear velocity by electric forces

The laboratory experiments reported in Chapter 2 show that electric forces provide an additional upwards force on surface particles, which aids their lifting by wind. They showed that the effect of electric forces on the threshold shear velocity is described by

$$u*_t = \sqrt{\frac{A_n}{\rho_a}\left(\rho_p g D_P + \frac{6\beta G}{\pi D_P} - \frac{8.22\varepsilon_0 E_{surf}^2}{c_s}\right)}, \quad (3.22)$$

where $A_n \approx 0.0123$ is a dimensionless parameter that scales the aerodynamic forces, ρ_p is the particle density, β is an empirical constant that scales the interparticle force between sand grains and is on the order of $10^{-5} - 10^{-3}$ kg/s^2, G is a geometric parameter that depends on the bed stacking and is of order 1, ε_0 is the electric permittivity of air, E_{surf} is the surface E-field as calculated by Eq. (3.4), and c_s is a scaling constant that accounts for the non-sphericity of soil particles. Our model uses Eq. (3.22) to quantify the reduction of the threshold shear velocity by electric forces.

3.7.8 Treatment of creeping particles

In wind-blown sand, the main mode of particle transport is saltation. However, a fraction of the mass transport occurs through particles striking the soil and pushing other particles in the direction of the wind flow. This surface transport of rolling and sliding particles is termed 'creep' [*Bagnold*, 1941]. Our model does not explicitly account for this mode of transport. However, most particles leave the surface (either through aerodynamic entrainment or splashing) with low speed, and will quickly settle back to the surface, as mathematically described by Eq. (3.14). These particles dominate the near-surface mass transport and can therefore be assumed to include the transport by creep [*Mitha et al.*, 1986]. This interpretation is supported by the good agreement between predicted and measured vertical and horizontal mass flux profiles, especially close to the surface where creep is important (Figures 3.2 and 3.3). Since electric forces reduce near-surface winds through Eq. (3.22), transport by creep is generally enhanced by electric forces, because fewer ejected or aerodynamically entrained surface grains will acquire enough speed to prevent them from quickly settling back to the surface.
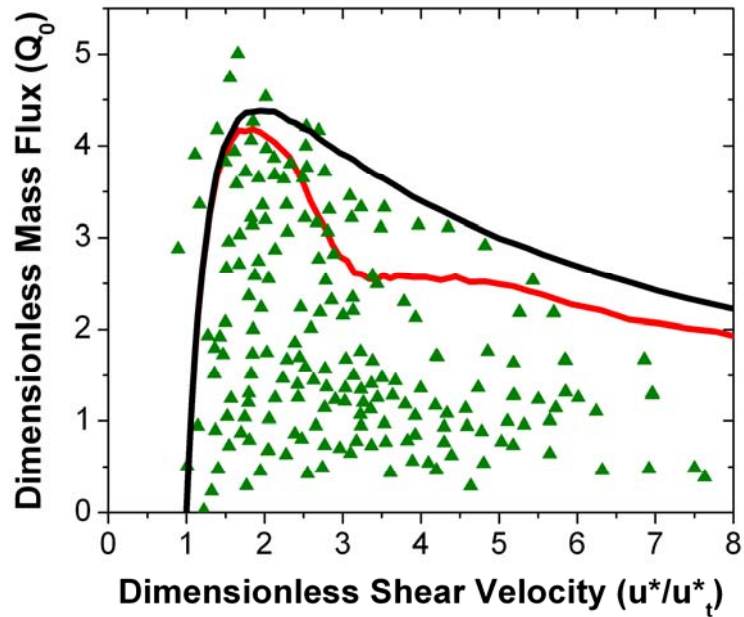
Figure 3.8: Dimensionless mass flux Q_0 (see Eq. 1.2) as a function of dimensionless shear velocity simulated with and without electric forces (red and black lines, respectively), and compared with results from more than a dozen wind tunnel studies and one field study (green triangles) compiled by *Iversen and Rasmussen* [1999]. A peak in the experimentally determined dimensionless mass flux is apparent around $u*/u*_t \approx 2$, and is reproduced by the model. Model results were obtained for the size distribution reported in *Namikas* [2003].

3.7.9 Additional model results

In Chapter 3.4, we show that our model produces results that are consistent with measurements of the vertical and horizontal profiles of the saltation mass flux (Figures 3.2 and 3.3). Here, we present additional tests of our numerical model of saltation.

The predicted height-integrated mass flux is in good qualitative agreement with data from over a dozen wind tunnel studies and one field study (Figure 3.8) [*Iversen and Rasmussen,* 1999]. In particular, the experimentally-determined peak in the dimensionless mass flux is well-reproduced by the model. To our knowledge, this peak has not been previously reproduced by numerical models and is often not reproduced by analytical models [*Iversen and Rasmussen,* 1999]. The predicted height-integrated mass flux appears larger than that measured by most experimental studies, which may be because sand collectors used in these studies have an efficiency of only ~50-70 % [*Greeley et al.,* 1996; *Rasmussen and Mikkelsen,* 1998]. Moreover, the effects of interparticle collisions on particle motion are neglected in the present model. *Sorensen*

and McEwan [1996] hypothesized that interparticle collisions attenuate the saltation mass flux at high shear velocities. We intend to present the effect of interparticle collisions on saltation in a future publication.

The inclusion of electric forces brings the predicted height-integrated mass flux in better agreement with measurements (red line in Fig. 3.8). However, it is not clear whether electric forces are fully equilibrated in the finite length available in wind tunnels. For this reason, wind tunnel studies might be inadequate for studying fully-developed saltation. Experimental studies are required to resolve this issue.

CHAPTER 4

THE ELECTRIFICATON OF WIND-BLOWN SAND ON MARS AND ITS IMPLICATIONS FOR ATMOSPHERIC CHEMISTRY

4.1 INTRODUCTION

On Mars, the electrification of wind-blown sand and dust storms could trigger electric discharges [*Eden and Vonnegut*, 1973; *Melnik and Parrot*, 1998] and reduce the wind stress required to lift particles from the surface (Chapter 2). Moreover, recent studies suggest that the large *E*-fields predicted in wind-blown sand and dust storms [*Melnik and Parrot*, 1998; *Farrell et al.*, 2003; *Zhai et al.*, 2006] produce energetic electrons [*Delory et al.*, 2006] that catalyze the production of hydrogen peroxide [*Atreya et al.*, 2006], a strong oxidant hostile to life as we know it. Indeed, these studies suggest that the atmosphere becomes supersaturated, causing hydrogen peroxide snow to precipitate onto the surface [*Atreya et al.*, 2006]. This provides a possible explanation for the reactive soil and the unexpected absence of organics at the Viking landing sites [*Oyama et al.*, 1977]. In addition, energetic electrons produced by strong *E*-fields are predicted to dissociate methane [*Farrell et al.*, 2006]. This is important because methane has been detected on Mars and is a possible marker of biological activity [*Formisano et al.*, 2004]. Both the production of hydrogen peroxide and the destruction of methane in Martian wind-blown sand and dust storms are thus highly relevant to studies of past and present life on Mars.

In the absence of direct measurements, most researchers have used laboratory experiments and numerical models to investigate the generation of *E*-fields in Martian saltation and dust storms. *Eden and Vonnegut* [1973] reported that shaking a flask of sand with CO_2 at Martian pressure produces electric discharges. The occurrence of electric discharges in Martian dust storms is also predicted by numerical models [*Melnik and Parrot*, 1998; *Farrell et al.*, 2003; *Zhai et al.*, 2006]. However, these numerical studies have two important shortcomings. First, because the charge transfer between colliding

sand/dust particles is poorly understood, these numerical studies have used charging models that are not constrained by either theory or experiments. Second, these studies have neglected the effects of E-fields on atmospheric conductivity. Fortunately, progress has recently been made on both these issues. Indeed, *Delory et al.* [2006] developed a plasma physics model that accounts for the production of energetic electrons by E-fields and the subsequent ionization of Martian air, while we recently developed an improved parameterization of sand/dust electrification that is constrained by E-field measurements in saltation on Earth (Chapter 3).

In this Chapter, we build on the study of *Delory et al.* [2006] to expand the numerical saltation model of Chapter 3 with plasma physics, and report the first calculations of E-fields in Martian saltation. Our study is an improvement over calculations of E-fields in dust storms [*Melnik and Parrot*, 1998; *Farrell et al.*, 2003; *Zhai et al.*, 2006] for three reasons: (i) our parameterization of the charge transfer between colliding sand/dust particles is constrained by measurements (Chapter 3), (ii) we account for the effects of E-fields on atmospheric conductivity [*Delory et al.*, 2006], and (iii) we account for the adsorption of ions and electrons to particulates [*Draine and Sutin*, 1987; *Jackson et al.,* 2008]. We find that electric discharges are unlikely to occur in Martian wind-blown sand, and that the production of hydrogen peroxide and the dissociation of methane by E-fields are less significant than previously thought.

4.2 MODEL DESCRIPTION

Our numerical model of saltation is described in detail in Chapter 3, and explicitly simulates the motion, concentration, and electric charging of saltating sand. Our model simulates saltation in the absence of suspended dust, as is representative of saltation on dunes, and its predictions are in good agreement with measurements of the particle mass flux and E-field in terrestrial saltation (Chapter 3). Here, we apply our model to Mars and calculate the E-field in saltation as described in Chapter 3. We assume that saltating particles have diameters $D_p = 100$ μm and density of 3000 kg/m^3 [*Claudin and Andreotti*, 2006], and take the atmospheric pressure (P) and temperature (T) as 627 Pa and 227 K. As described in more detail below, we expand the model by including the effects of E-

fields on atmospheric conductivity and accounting for the adsorption of ions and electrons to particulates.

4.2.1 Limits to Electric Fields on Mars

On Earth, sand and dust electrification can produce large E-fields (Section 1.2.1) because air is a good insulator and the E-field at which electric discharges occur is large (about 3 MV/m). The situation is quite different on Mars. There, E-fields are limited by large increases in atmospheric conductivity when E-fields become sufficiently large to ionize CO_2 [*Delory et al.*, 2006], and by electric discharges thought to occur at ~20-25 kV/m [*Melnik and Parrot*, 1998].

The E-field at which the insulating properties of a gas break down and an electric discharge occurs is described by the 'Paschen law' [*Raizer*, 1997; *Fridman and Kennedy*, 2004], and depends on the gas pressure and the distance of the "electrodes" (or centers of charge) between which the discharge occurs,

$$E_{\mathrm{br}} = \frac{BPT_0/T}{C + \ln(Pz_{\mathrm{cat}}T_0/T)},$$
(4.1)

with $C = \ln[A/\ln(1/\gamma + 1)]$. The constants A = 15 $m^{-1}Pa^{-1}$ and B = 350 $Vm^{-1}Pa^{-1}$ define the Townsend ionization coefficient α (see page 56 in *Raizer* [1997]) at T_0 = 293 K for a CO_2 atmosphere. We take the secondary Townsend ionization coefficient γ as 0.01 [*Raizer*, 1997; *Fridman and Kennedy*, 2004]. Note that Eq. (4.1) does not include the effect of sand and dust on the breakdown E-field. In the case of negatively charged saltating sand over a positively charged soil surface (see Chapter 3), the surface represents the anode, but the cathode is not well defined. We approximate the distance from the cathode to the anode by the height z_{cat} below which 50 % of the charge on saltating sand is contained. The results reported here are not sensitive to this approximation. For typical Martian saltation, we find z_{cat} = 30 cm and E_{br} = 43 kV/m, which is significantly above the ~20-25 kV/m value at which larger-scale discharges in dust storms are thought to occur [*Melnik and Parrot*, 1998].

The second mechanism limiting the generation of E-fields in Martian saltation and dust storms is the increase in atmospheric conductivity due to ionization by energetic electrons [*Delory et al.*, 2006]. The conductivity of the near-surface Martian atmosphere

is due mostly to mobile ions [*Molina-Cuberos et al.*, 2002] and equals [e.g., *Michael et al.*, 2008]

$$\sigma = e\left(K_e n_e + K_- n_- + K_+ n_+\right),$$ (4.2)

where e is the elementary charge, and K_e, K_-, K_+, n_e, n_-, and n_+ are the mobilities and number densities of free electrons and negative and positive ions, respectively. We take the 'background' concentration of electrons and ions to be $n_{e,0} = 5 \times 10^6$ m^{-3} and $n_{-,0} = n_{+,0}$ = 3×10^9 m^{-3} [*Molina-Cuberos*, 2001, 2002; *Delory et al.*, 2006]. Charges in the Martian atmosphere decay due to the adsorption of electrons and ions of opposite polarity, which is a complex process [*Draine and Sutin*, 1987; *Michael et al.*, 2008]. However, the conductivity defines the approximate time scale $t_{rel} = \varepsilon_0 / \sigma$, where ε_0 is the electric permittivity, with which charges in the Martian atmosphere decay. A simplified expression of this charge decay is thus

$$q(t + \Delta t) = q(t)\exp\left(-\Delta t / t_{rel}\right),$$ (4.3)

where $q(t)$ is the charge of the particle (or the surface) at time t, and Δt is the model time step. As the atmospheric conductivity increases, the charge relaxation time t_{rel} decreases, thereby also decreasing the charge held by saltating particles and the soil surface.

4.2.2 Plasma Physics

Electric fields on Mars are thus limited by the occurrence of electric discharges (Eq. 4.1) and by increases in atmospheric conductivity (Eqs. 4.2 and 4.3). As electrons are accelerated from the cathode (the top of the saltation layer) towards the anode (the surface), they can ionize CO_2 and produce additional free electrons, but they can also be absorbed through dissociative attachment to CO_2 [*Delory et al.*, 2006] and collisions with saltating sand particles. The electron concentration in the saltation layer is then approximately given by [*Raizer*, 1997; *Delory et al.*, 2006; *Jackson et al.*, 2008]

$$n_e = n_{e,0} \exp\left\{ \int_0^{z_{cat}} \left[\alpha(z) - \frac{k_{da}(z)N_{CO2}}{v_d(z)} - \frac{1}{4}\pi D_p^2 n_{salt}(z)\tilde{J}(z) \right] dz \right\},$$ (4.4)

where N_{CO2} is the CO_2 number concentration, v_d is the electron drift velocity and is obtained from Figure 4a in *Delory et al.* [2006], n_{salt} is the concentration of saltating sand particles as predicted by our saltation model (see Chapter 3), and $\tilde{J}$ is the normalized

cross section for a collision occurring between an electron and a saltating sand particle.

Since the sand particles are strongly negatively charged, we have $\tilde{J} < 1$, following Eq. (3.5) in *Draine and Sutin* [1987] and using Eq. (1) in *Jackson et al.* [2008] to obtain the electron temperature as a function of the *E*-field. Furthermore, we obtain the dissociative attachment rate constant k_{da} from Figure 4d of *Delory et al.* [2006], who solve the electron energy distribution to find k_{da} as a function of the *E*-field. Finally, we use Figure 4b of *Delory et al.* [2006] to obtain the Townsend ionization coefficient α, which describes the multiplication of electrons per unit length due to ionizing collisions as the initial population (n_0) is accelerated from the cathode to the anode [*Raizer*, 1997; *Fridman and Kennedy*, 2004]. This electron population becomes increasingly energetic as the *E*-field rises, and can produce positive ions (mainly CO_2^+) through electron impact ionization, and negative ions (mainly O^-) through dissociative attachment [*Delory et al.*, 2006]. The CO_2^+ ions quickly react with CO_2, O_2, and H_2O to form $H_3O^+ \cdot (H_2O)_j$ with $j \geq 1$, while O^- ions attach to CO_2, forming CO_3^-, which is hydrated to $CO_3^- \cdot (H_2O)_j$ [*Molina-Cuberos et al.*, 2001, 2002]. The concentration of negative ions in the saltation layer is then described by [*Michael et al.*, 2008]

$$\frac{dn_-}{dt} = \frac{N_{CO2} n_e}{z_{cat}} \int_0^{z_{cat}} k_{da}(z) dz - n_- n_+ k_{rec} - \frac{n_- K_- E_{surf}}{z_{cat}}, \qquad (4.5)$$

where N_{CO2} is the CO_2 number concentration, and E_{surf} is the surface *E*-field. The first term on the right-hand side denotes the production of negative ions through dissociative attachment to CO_2 [*Delory et al.*, 2006], the second term describes the recombination of positive and negative ions [*Molina-Cuberos et al.*, 2002], and the final term accounts for the adsorption of negative ions to the positively charged soil surface. We neglect other processes that are insignificant compared to these ion loss processes, such as photodetachment [*Molina-Cuberos et al.*, 2001; *Michael et al.*, 2007] and the attachment of negative ions to the strongly negatively charged saltating particles [*Draine and Sutin*, 1987], and we neglect the transport of ions out of the saltation layer. Furthermore, we take the ion recombination rate constant as $k_{rec} = 1.5 \times 10^{-13}$ m^{3}sec^{-1} [*Molina-Cuberos et al.*, 2002], and calculate n_- and n_+ iteratively using $n_+ = n_- + n_e$ [*Molina-Cuberos et al.*, 2001] and $dn_-/dt = 0$ in steady-state. We then use the ion and electron concentrations to

calculate the atmospheric conductivity using Eq. (4.2), with ion and electron mobilities derived from equations (5) and (7) of *Michael et al*. [2008], assuming the dominant ions to be $H_3O^+ \cdot (H_2O)_3$ and $CO_3^- \cdot (H_2O)_2$ [*Molina-Cuberos et al*., 2001, 2002].

4.3. RESULTS AND DISCUSSION

We implement the plasma physics processes discussed above in the numerical model of saltation described in Chapter 3, and iteratively calculate the *E*-field, the atmospheric conductivity, and the motion, charging, and concentration of saltating sand until steady-state is reached. As on Earth (see Chapter 3), the *E*-field in Martian saltation peaks at the surface and decreases monotonically with height (inset of Figure 4.1). On Mars, the rate of decrease of the *E*-field with height is smaller than on Earth because the smaller gravitational and aerodynamic drag forces cause the saltation layer to be thicker there [*Almeida et al*., 2008].
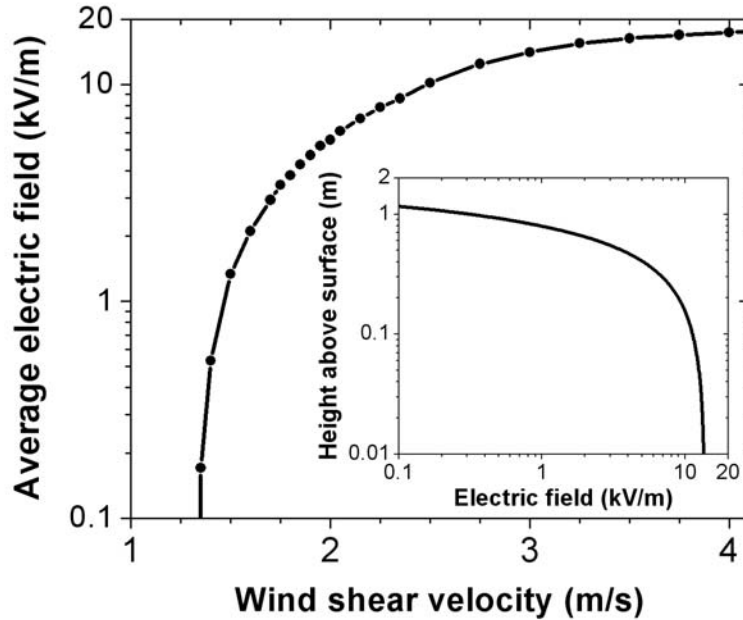
Figure 4.1: Simulated average *E*-field between the anode (the surface) and the cathode ($z_{cat} \approx 30$ cm) in Martian saltation as a function of wind shear velocity, $u^* = \sqrt{\tau / \rho_a}$, where τ is the wind shear stress directly above the saltation layer [*Shao*, 2000] and ρ_a is atmospheric density. The inset shows the vertical profile of the *E*-field for a wind shear velocity of 2.5 m/s. The results are obtained with the numerical model of saltation described in Chapter 3, expanded with Eqs. (4.2) – (4.5) to account for plasma physics processes and charge relaxation.

As expected, the E-field in the saltation layer increases with wind speed (Figure 4.1). The resulting increasingly energetic electron population starts dissociating CO_2 (i.e., $e + CO_2 \rightarrow CO + O^-$) at a few kV/m and ionizing CO_2 (i.e., $e + CO_2 \rightarrow 2e + CO_2^+$) at ~10 kV/m [*Delory et al.*, 2006]. The resulting increase in the concentration of ions and electrons with the E-field (Figure 4.2) enhances the atmospheric conductivity, which neutralizes the charges on saltating particles and the surface (see Eq. 4.3), thereby limiting further increases in the E-field. Indeed, we find that this negative feedback limits the E-field in Martian saltation to ~15–20 kV/m. This upper limit on the E-field in Martian saltation is relatively insensitive to uncertainties in model parameters and the model methodology, because of the sharp dependence of the production rate of ions on the E-field (see *Delory et al.* [2006], figure 4d).

Since the maximum E-field of ~15-20 kV/m is significantly below the threshold of ~43 kV/m required to initiate electric discharges (see Eq. 4.1), we conclude that such discharges are unlikely to occur in Martian saltation. However, discharges might still occur in dust devils and dust storms for several reasons. First, the E-field required to precipitate discharges over larger scales in dust storms is lower (see Eq. 4.1). Moreover, the abundant presence of particulate matter in dust storms likely lowers the background concentration of ions and electrons (n_0) [*Eden and Vonnegut*, 1973; *Michael et al.*, 2008], thereby increasing the charge relaxation time and thus the E-field. Finally, large-scale discharges in dust storms could occur at a lower E-field than predicted by the Paschen law (Eq. 4.1) through electron runaway breakdown [*Gurevich et al.*, 1992].

Recent studies have predicted that E-fields of 10-25 kV/m generate plasma conditions that produce hydrogen peroxide and dissociate methane in large quantities [*Delory et al.*, 2006; *Atreya et al.*, 2006; *Farrell et al.*, 2006]. While we here indeed find that the E-field in saltation can exceed 10 kV/m for large wind speeds, we also find that the concentration of ions and electrons at such E-fields is much smaller than suggested by these previous studies (Figure 4.2). The difference occurs because we expanded on these previous studies and accounted for losses of ions and electrons due to adsorption to saltating sand and the soil surface, as well as the loss of electrons from dissociative attachment to CO_2. A separate calculation shows that the large concentration of electrons and ions predicted by following these previous studies [*Delory et al.*, 2006; *Atreya et al.*,

2006] are unlikely to occur in saltation or dust storms, because the large conductivity of the resulting plasma limits the E-field to values well below those necessary to maintain the plasma (Figure 4.3). Indeed, the charging current necessary to maintain these plasma conditions is several orders of magnitude larger than that produced by saltation (Figure 4.3). Since saltation probably plays a key role in charge generation in dust storms and dust devils (see Section 1.2), we expect the charging current in these phenomena to be of similar magnitude as in saltation. We therefore conclude that the concentration of ions and electrons in Martian wind-blown sand, dust devils, and dust storms, is much smaller than previously suggested [*Delory et al.*, 2006; *Atreya et al.*, 2006]. The production of hydrogen peroxide and the dissociation of methane by E-fields in these phenomena are thus probably less significant than previously thought [*Atreya et al.*, 2006; *Farrell et al.*, 2006].
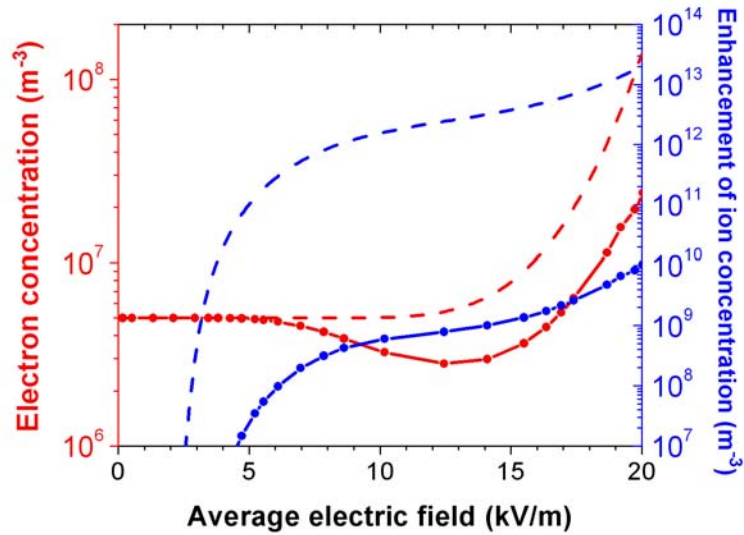
Figure 4.2: Simulated concentrations of electrons (left axis and red lines) and the enhancement of the ion concentration over the background concentration ($n_{-,0} = n_{+,0} = 3 \times 10^9$ m^{-3} [*Molina-Cuberos et al.*, 2002]; right axis and blue lines) as a function of the average E-field between the anode and the cathode. Solid lines with circles indicate results from our numerical saltation model (see Chapter 3) for which the anode is at the surface and the cathode is at the height z_{cat} (see text). For E-fields of ~5-12 kV/m, the electron concentration decreases because of dissociative attachment to CO_2 and adsorption to sand particles, whereas for larger E-fields the electron concentration increases due to the generation of additional electrons through ionization of CO_2 [*Delory et al.*, 2006]. Dashed lines indicate electron and ion concentrations calculated for a homogenous E-field over a length of 0.5 m following *Delory et al.* [2006] and *Atreya et al.* [2006]. That is, we use Eqs. (4.4) and (4.5) to calculate the ion and electron concentrations, but neglect the terms in these equations that account for losses of electrons and the loss of ions to the soil surface.
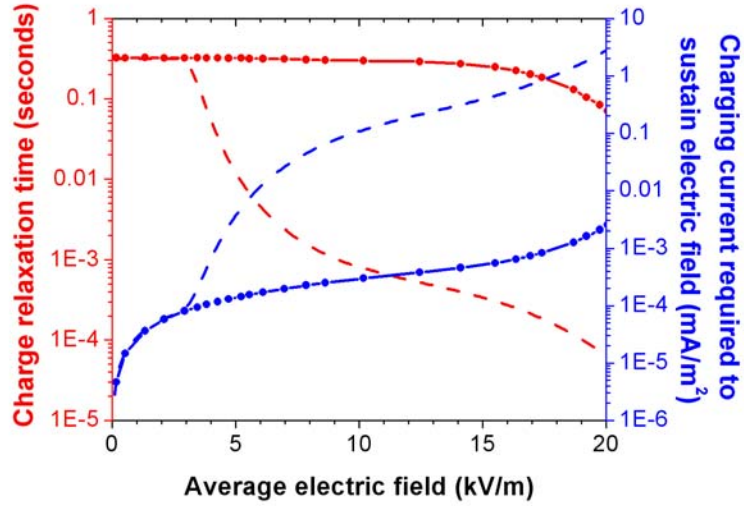
Figure 4.3: Simulated charge relaxation time (left axis and red lines) and charge separation current ($I = \sigma E$) required to sustain the E-field (right axis and blue line) against the relaxation of charge on saltating particles and the surface, as a function of the average E-field between the anode and the cathode. Solid lines with circles indicate results from our numerical saltation model (see Chapter 3) for which the anode is at the surface and the cathode is at the height z_{cat} (see text). Dashed lines indicate results following *Delory et al.* [2006] and *Atreya et al.* [2006], as described in the caption of Figure 4.2.

4.4 CONCLUSIONS

We present the first numerical simulation of E-fields in Martian saltation, and find that E-fields are limited to ~15-20 kV/m. This upper limit is imposed by the rapid increase in atmospheric conductivity as the E-field rises and probably prevents the occurrence of electric discharges in Martian saltation.

Furthermore, our results show that chemical reactions catalyzed by E-fields in saltation are not as important as previously thought [*Atreya et al.*, 2006; *Farrell et al.*, 2006]. Indeed, we find that the plasma in which these reactions occur cannot be sustained because its large conductivity limits the E-field to values well below that necessary to maintain the plasma (Figure 4.3). Nonetheless, the concept of electro-chemical production of oxidants in Martian saltation and dust storms, possibly through electric discharges, remains a possible explanation for the puzzling absence of organics from the Martian soil [*Oyama et al.*, 1977; *Atreya et al.*, 2006] and should be investigated further.

4.5 ACKNOWLEDGEMENTS

CHAPTER 5

THE ELECTRIFICATION OF GRANULAR SYSTEMS OF IDENTICAL INSULATORS

5.1 INTRODUCTION

It has been known since ancient times that two objects rubbed together can charge each other [*Harper*, 1967; *Lowell and Rose-Innes*, 1980]. This frictional or 'triboelectric' charge transfer also occurs between two insulators, which is quite remarkable considering that insulators do not contain free charge carriers [*Lowell and Rose-Innes*, 1980; *Lowell*, 1986; *Shinbrot et al.*, 2008]. Even more remarkable is the observation that triboelectric charging also occurs between insulating particles that are chemically identical (i.e., that have the same contact potential) [*Shaw*, 1926; *Henry*, 1953; *Lowell and Truscott*, 1986a, 1986b; *Shinbrot et al.*, 2008]. For granular systems, the charging is generally such that smaller particles charge negatively while larger particles charge positively. This size-dependent charging of identical insulators has recently been demonstrated in fluidized beds [*Forward et al.*, 2009a], and is suggested by measurements in a wide variety of other granular systems, including powder handling [*Inculet et al.*, 2006], wind-blown sand on Earth [*Schmidt et al.*, 1998; *Zheng et al.*, 2003] and possibly Mars [*Shinbrot et al.*, 2006], wind-blown snow [*Schmidt et al.*, 1999], and volcanic eruptions [*Miura et al.*, 2002]. Determining the physical mechanism behind this perplexing phenomenon could produce fundamental advances in xerox technology [*Schein*, 2007], and further our understanding of the electrification of sand, dust, ash, powder, snow, and ice, and the subsequent occurrence of discharges and associated chemical reactions in these systems [*Lowell and Truscott*, 1986b; *Inculet et al.*, 2006; *Shinbrot and Herrmann*, 2008; *Yair*, 2008; see Chapter 4].

Several physical models have been proposed to explain the mysterious triboelectric charging of identical insulators. *Henry* [1953] conjectured that the charge transfer is due to temperature gradients caused by asymmetry in the rubbing, but experiments by *Lowell*

and Truscott [1986a, 1986b] showed that the charging does not depend on the rubbing speed and therefore the temperature gradient, but only on the total distance over which one object is rubbed over the other. Based on these experimental results, *Lowell and Truscott* [1986b] proposed that the charge transfer is instead due to the presence of high-energy electrons 'trapped' in defect states [*Duke*, 1978]. These states cannot equilibrate with nearby empty low-energy states on the same particle because of energetic constraints [*Lowell and Rose-Innes*, 1980; *Lowell and Truscott*, 1986b]. The existence of these trapped high-energy electron states is supported by the occurrence of phosphorescence and thermoluminescence phenomena in insulators [*Randall and Wilkins*, 1945; *Kron et al.*, 1997; *Aitken*, 1997]. However, if surface contact brings empty low-energy states on another particle within close enough proximity, trapped high-energy electrons could tunnel to those states [*Lowell and Truscott*, 1986b]. An asymmetry in the nature of the surface contact between the two objects could thus produce an imbalance in the number of transferred electrons and thus produce a net transfer of charge. For example, the experiments of *Shaw* [1926], *Henry* [1953], and *Lowell and Truscott* [1986a, 1986b] showed that rubbing a small area of one object over a large area of another, identical, object causes the former object to obtain a negative charge.

For granular systems, *Lacks et al.* [2008] recently showed that a systematic charge transfer is produced by a different asymmetry. They showed that, after several initial collisions in which small and large colliding particles lose roughly equal amounts of trapped electrons, smaller particles have nonetheless lost a larger fraction of their trapped electrons than larger particles have. Therefore, in subsequent collisions, smaller particles give up fewer trapped electrons than larger particles do, leading smaller particles to charge negatively and larger particles to charge positively, in agreement with the measurements discussed above [*Schmidt et al.*, 1998, 1999; *Miura et al.*, 2002; *Zheng et al.*, 2003; *Inculet et al.*, 2006; *Forward et al.*, 2009a].

We here identify a second mechanism that causes small particles to charge negatively and large particles to charge positively. We show that simple geometric considerations cause more electrons to tunnel from the larger particle to the smaller particle than vice versa. We combine this charging mechanism with the 'multiple collisions' mechanism discussed above, and develop the first quantitative charging

scheme for a granular system of identical insulators. The scheme also accounts for the effect of particle charge on subsequent charge transfer, following *Castle and Schein* [1995]. The predictions of our charging scheme are in both qualitative and quantitative agreement with measurements.

In the next section we describe our theoretical model and discuss its assumptions. In Section 5.3, we then use this model to derive the geometric charge transfer due to differences in particle size, formulate a quantitative charging scheme, and compare the predictions of this charging scheme to measurements. In Section 5.4, we discuss the limitations of our charging scheme.

5.2 THEORETICAL MODEL

We consider a granular system of idealized spherical insulating particles that are chemically identical. For simplicity, we assume that electrons on the surface of these particles can be in either a low-energy (L) or a high-energy (H) state [*Lowell and Truscott,* 1986b; *Lacks et al.*, 2008]. The number of high and low-energy electrons on the particle's surface at time t are denoted as $n_{iH}(t)$ and $n_{iL}(t)$, and the initial number of high-energy electrons is given by

$$n_{iH}(0) = 4\pi R_i^2 \rho_{H,0}, \qquad (5.1)$$

where R_i is the radius of particle i. We assume the initial density of high-energy surface states, $\rho_{H,0}$, to be equal for all particles [*Lacks et al.*, 2008; *Duff and Lacks*, 2008]. The surface density of low-energy electrons is probably several orders of magnitude larger [*Lowell and Truscott,* 1986b], but following previous investigators [*Lowell and Truscott,* 1986b; *Lacks et al.*, 2008; *Duff and Lacks*, 2008] we assume that their contribution to the charge transfer is negligible, and the initial value $n_{iL}(0)$ is thus irrelevant.

We assume that, during a collision, electrons can relax from high-energy states on one particle to low-energy states on the opposite particle. Specifically, we assume that all high-energy electrons within a distance δ_0 of the surface of the opposite particle (Fig. 5.1a) will tunnel to empty low-energy states on that particle's surface [*Lowell and Truscott,* 1986b; *Lacks et al.*, 2008; *Duff and Lacks*, 2008]. *Lowell* modeled this electron transfer process in terms of the tunneling dynamics of a particle in a one dimensional square well separated by an energy barrier from another square well (Fig. 5.1b) [*Lowell,*

1979]. He showed that the maximum distance δ_0 that an electron in the ground state of a square well can tunnel during a collision is approximately given by

$$\delta_0 = \frac{\hbar}{\sqrt{8mE_\mathrm{b}}} \ln\left(\frac{\hbar}{\eta m}\frac{t_\mathrm{coll}}{a^2} \right), \tag{5.2}$$

where $\eta = \left(1.12/\pi^2\right)\left(2+\pi\right)$, E_b is the height of the energy barrier between the two potential wells (see Fig. 5.1b), m is the electron mass, $\hbar$ is the reduced Planck constant, t_coll is the time scale of the collision, and a is the radius of the well corresponding to the electron trap. Since electrons can transfer between particles during collisions, net charges can develop on the particles. The net charge on a particle of type i is then given by

$$q_i(t) = e\left[n_{iH}(0) - n_{iH}(t) + n_{iL}(0) - n_{iL}(t)\right], \tag{5.3}$$

where e is the elementary charge.
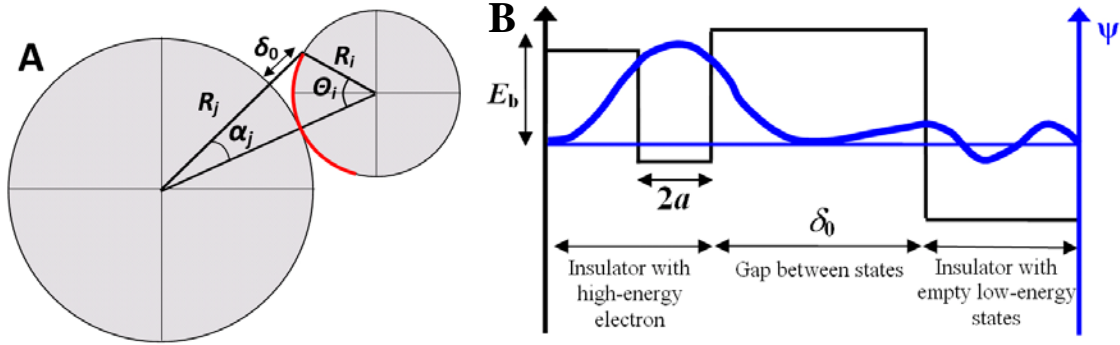
Figure 5.1: (**a**) Schematic of the charge transfer occurring during a collision between two spherical particles of identical material but of different sizes R_i and R_j. The angle θ_i represents the maximum angle from the point of contact on particles i and j from which trapped high-energy electrons can transfer to empty low-energy states on the opposite particle. The area in which electrons can transfer in this manner is indicated by the red arc. (**b**) Simplified schematic representation of the wavefunction of a high-energy electron in an electron trap near the surface of another insulator with empty low-energy states. The black line denotes the electron's potential energy as a function of position, and the blue line denotes its wavefunction. After Fig. 1 in *Lowell* [1979].

If the colliding particles hold net charges, then the electrostatic potential difference ΔV between their surfaces will make the transfer of electrons from the negatively charged to the positively charged particle more energetically favorable than vice versa [*Castle and Schein*, 1995; *Castle*, 1997]. Indeed, this effect will alter the barrier height

such that $E_{\mathrm{b}} = E_{\mathrm{b}0} + e\Delta V$. The potential difference between colliding particles with charges q_i and q_j is approximately given by [*Lowell and Rose-Innes*, 1980; *Castle*, 1997]

$$\Delta V = \frac{\delta_0}{4\pi\varepsilon_0}\left(\frac{q_i}{R_i^2} - \frac{q_j}{R_j^2}\right).$$ (5.4)

Note that ΔV and δ_0 are interdependent, such that Eqs. (5.2) and (5.4) must be solved iteratively.

5.3. RESULTS

5.3.1 Geometric effect in a single collision

We use the theoretical model described above to study the charge transfer between colliding idealized spherical particles of different sizes due. The charge transfer is caused by the tunneling of trapped high-energy electrons to empty, low-energy states on the other particle. We hypothesize that this transfer of electrons is proportional to the particle's surface area that, at the instant of collision, is within the distance δ_0 of the surface of the opposite particle (See Fig. 5.1a).

From Fig. 5.1a, the number of electrons transferred from the high energy states of particle i ($-\Delta n_{i\mathrm{H}}$) to the empty low energy states of particle j ($\Delta n_{j\mathrm{L}}$), is equal to

$$-\Delta n_{i\mathrm{H}} = \Delta n_{j\mathrm{L}} = 2\pi\rho_{\mathrm{H},0}R_i^2\left(1 - \cos\theta_i\right).$$ (5.5)

The angle θ_i represents the maximum angle from the contact point for which the surface of particle i is within the distance δ_0 of the surface of particle j (see Fig. 5.1a), and satisfies

$$R_i \sin\theta_i = \left(R_j + \delta_0\right)\sin\alpha_j;$$ (5.6a)

$$R_i \cos\theta_i + \left(R_j + \delta_0\right)\cos\alpha_j = R_i + R_j;$$ (5.6b)

where the angle α_j is defined in Fig. 5.1a. Solving Eq. (5.6a) for α_j, using that $\cos(\arcsin x) = \sqrt{1 - x^2}$, squaring both sides, and solving for $\cos\theta_i$, we find

$$\cos\theta_i = 1 - \frac{\delta_0}{2R_i}\frac{2R_j + \delta_0}{R_i + R_j}.$$ (5.7)

Substituting this result into Eq. (5.5) then yields the number of electrons transferred between the colliding particles in terms of the particle sizes, the density of trapped states, and the tunneling distance

$$-\Delta n_{i\mathrm{H}} = \Delta n_{j\mathrm{L}} = \pi \rho_{\mathrm{H},0} R_i \delta_0 \frac{2R_j + \delta_0}{R_i + R_j}.$$ (5.8)

Substituting Eq. (5.8) into Eq. (5.3) then yields the net charge transfer experienced by particle i

$$\Delta q_i = \pi e \rho_{\mathrm{H},0} \delta_0^{\,2} \left(\frac{R_i - R_j}{R_i + R_j} \right).$$ (5.9)

Simple geometry thus leads the larger colliding particle to obtain a positive charge denoted by Eq. (5.9), while the smaller particle loses a charge of the same magnitude. This net transfer of charge increases with the imbalance in particle sizes, in agreement with experimental observations [*Zheng et al.*, 2003; *Krauss et al.*, 2003; *Forward et al.*, 2009a].

Although the above result – that in a single collision the larger particle will charge positively and the smaller particle will charge negatively – is valid for idealized spherical particles only, we show in Chapter 5.7 that a similar charge transfer occurs during collisions between cubical particles. Since most natural particles can probably be described as a superposition of spherical and cubical shapes, we argue that the size-dependent charging of spherical and cubical particles can be generalized to natural particles.

5.3.2 Charge transfer scheme including multiple collisions

In addition to the geometric charge transfer mechanism identified above, identical insulators can also charge through undergoing multiple collisions [*Lacks et al.*, 2008]. In essence, these two charging mechanisms are different manifestations of the same physical process: the transfer of trapped high-energy electrons during collisions [*Lowell and Truscott,* 1986b]. In this section, we thus seek to derive a charging scheme that unifies these two related charging mechanisms.

Consider the granular system of identical insulators described in Chapter 5.2. The change in the number of low-energy and high-energy electrons due to charge transfer during particle collisions is given by [*Lacks et al.*, 2008]

$$\frac{dn_{iH}(t)}{dt} = -\sum_j N_j \sigma_{ij} \overline{v_{rel}^{ij}} C^{ij} n_{iH}(t), \text{ and} \tag{5.10a}$$

$$\frac{dn_{iL}(t)}{dt} = \sum_j N_j \sigma_{ij} \overline{v_{rel}^{ij}} C^{ji} n_{jH}(t), \tag{5.10b}$$

where j sums over all particle sizes present in the system, N denotes the particle density, and $\sigma_{ij} = \pi(R_i + R_j)^2$ and $\overline{v_{rel}^{ij}}$ are respectively the collisional cross section and the average relative velocity between particles i and j. The chance C^{ij} that a given high-energy electron on particle i will transfer to an empty low-energy state on particle j depends on the fraction of the particle's surface area that is close enough to the opposite particle's surface (Fig. 5.1a) to allow high-energy electrons to tunnel across. We determine this fraction from Eq. (5.8), obtaining

$$C^{ij} = \frac{\delta_0}{4\pi R_i} \frac{2R_j + \delta_0}{R_i + R_j}. \tag{5.11}$$

The time-evolution of charges on particles in a granular system can thus be obtained by numerically solving Eq. (5.10), and using Eqs. (5.2–5.4, 5.11) to obtain C^{ij}.

In addition to this numerical solution, we can obtain an analytical solution in the limit where the potential difference between oppositely charged particles is not large enough to significantly affect the charge transfer (that is, $\Delta V << E_{b0}$). In this case, we can substitute Eq. (5.11) into Eq. (5.10a) and solve for n_{iH}, yielding

$$n_{iH}(t) = n_{iH}(0)\exp(-t/\tau_i), \tag{5.12}$$

where the decay time constant τ_i is given by

$$\tau_i = \frac{4R_i}{\pi \delta_0 \sum_j N_j \overline{v_{rel}^{ij}} (R_i + R_j)(2R_j + \delta_{eff})}. \tag{5.13}$$

Using Eqs. (5.11–5.13) to solve (5.10b) for n_{iL} then yields

$$n_{iL}(t) = \pi^2 \rho_{H,0} \sum_j N_j \overline{v_{rel}^{ij}} R_j \delta_0 (R_i + R_j)(2R_i + \delta_0)\tau_j [1 - \exp(-t/\tau_j)] + n_{iL}(0), \tag{5.14}$$

such that the net charge over time on a particle is given by

$$q_i(t) = 4\pi R_i^2 e \rho_{H,0} [1 - \exp(-t/\tau_i)]$$

$$-\pi^2 e \rho_{H,0} \sum_j N_j \overline{v_{rel}^{ij}} R_j \delta_0 (R_i + R_j)(2R_i + \delta_0) \tau_j [1 - \exp(-t/\tau_j)]. \quad (5.15)$$

Eqs. (5.10) and (5.15) are respectively the first quantitative numerical and analytical expressions of the triboelectric charging of a granular system of identical insulators.
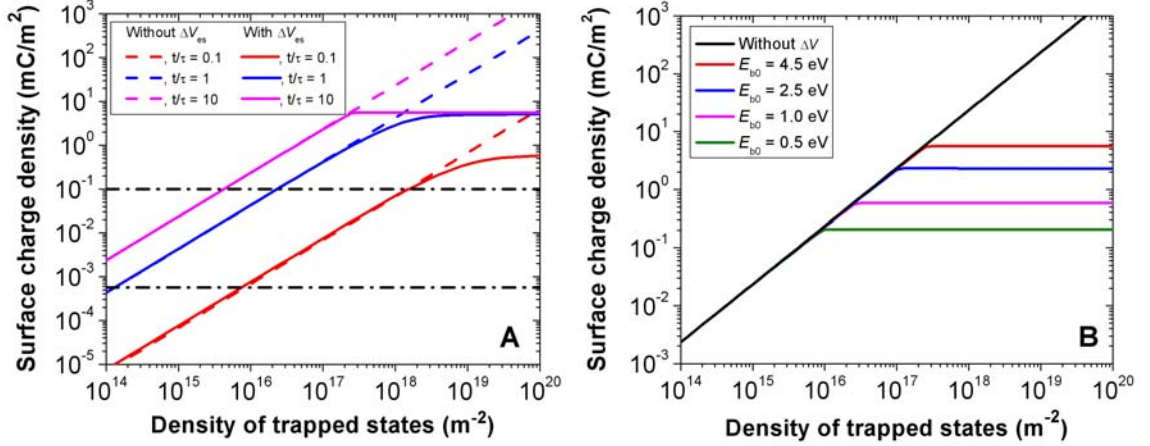
Figure 5.2: **(a)** Average absolute value of the surface charge density as a function of the density of trapped electron surface states for a binary mixture of two particle sizes for t/τ = 0.1, 1, and 10. Dashed and solid lines respectively denote predictions of the analytical (Eq. 5.15) and numerical (Eq. 5.10) solutions. The latter solution accounts for the effect of net particle charges on the subsequent charge transfer during collisions [*Castle and Schein*, 1995; *Castle*, 1997]. This effect causes the surface charge density to be nearly independent of the density of trapped states for $\rho_{H,0}$ > ~10^{18} m^{-2}. The results in this figure depend on the ratio of particle sizes, which we took as 1:4, and on the barrier energy (see Fig. 5.1b), which we took as E_{b0} = 4.5 eV [*Lowell*, 1979]. Note that the results are independent of all other parameters, such as the particle concentration and relative velocity. Those parameters only affect the characteristic charging time τ (see Eq. 5.13). The dash-dotted lines represent lower and upper limits on particle charge densities measured in wind-blown sand and dust devils [*Schmidt et al.*, 1998; *Fuerstenau and Wilson*, 2004].
(b) Same as part **(a)**, except for different values of the barrier energy E_{b0}, with t/τ = 10.

5.3.3 Quantitative application of the charging scheme

To apply the charging scheme developed in the previous section, we must assign numerical values to the parameters $\rho_{H,0}$, E_{b0}, and the ratio t_{coll}/a^2. We take t_{coll}/a^2 = 1 ns/Å^2, based on the estimates a = 1 Å [*Lowell*, 1979] and t_{coll} = 1 ns for two particles that collide with a characteristic speed of 1 m/s and interact over a length scale of ~1 nm [*Lowell*, 1979; *Lowell and Rose-Innes*, 1980]. Note, however, that the results depend only very weakly on the ratio t_{coll}/a^2, due to the logarithm term in Eq. (5.2). The model is more

sensitive to the values of $\rho_{H,0}$ and E_{b0}, and we thus present results over the range of realistic values of these parameters.

Results of the model, with the parameter values described in the previous paragraph, are shown in Figures 5.2 and 5.3. These results are obtained by the numerical solution of Eq. (5.10) and the analytical solution of Eq. (5.15). We find that the charge transfer is usually dominated by the multiple collisions mechanism [*Lacks et al.*, 2008], except when only a few collisions occur, in which case geometric charging (Eq. 5.9) dominates.

Figure 5.2a shows the dependence of the surface charge density on $\rho_{H,0}$ for a binary mixture of two particle sizes. The value of $\rho_{H,0}$ is limited between a lower bound of the typical charge density generated in granular systems of identical insulators ($\sim 10^{14}$ elementary charges per m^2 [*Schmidt et al.*, 1998, *Fuerstenau and Wilson*, 2004]) and an upper bound of ~1 trapped electron per atom ($\sim 10^{20}$ states per m^2). The predicted surface charge density (see Fig. 5.2a) over this wide range of $\rho_{H,0}$ is on the order of magnitude found in experiments [*Schmidt et al.*, 1998, *Fuerstenau and Wilson*, 2004]. Moreover, the magnitude of the surface charge density depends linearly on $\rho_{H,0}$ for small values, but is independent of $\rho_{H,0}$ for larger values of $\rho_{H,0}$, because the electrostatic potential difference ΔV between oppositely charged particles limits any further charge transfer (see Eqs. 5.2 and 5.4). This is a striking parallel to the low and high-density limits of the surface state theory [*Castle and Schein*, 1995; *Castle*, 1997], which describes the charge transfer between insulators of different materials. This qualitative agreement between different approaches to a similar problem is encouraging.

The surface charge density at which the transition between the low-density and high-density regimes occurs depends on the height of the energy barrier E_{b0} (see Fig. 5.2b). A reasonable upper limit on E_{b0} is the equivalent Fermi level of insulators, which is around 4.5 eV [*Lowell*, 1979; *Lowell and Rose-Innes*, 1980]. A detailed electronic structure analysis would be necessary to determine a more precise estimate for E_{b0}. Note that the transition between the low-density and the high-density regime can be very sharp (see also Fig. 5.3a), because of the interdependence between the electrostatic potential difference between colliding particles (ΔV) and the tunneling distance (δ_0). Once ΔV becomes on the order of E_{b0}, it substantially increases δ_0 (see Fig. 5.3b), which in turn

increases ΔV (see Eqs. 5.2 and 5.4). This positive feedback between ΔV and δ_0 produces a sensitive dependence of the tunneling distance on the particle charges, leading to the sharp transition between the low-density and high-density regimes for large times in Figures 5.2 and 5.3. This effect is probably not realistic for an ensemble-averaged particle charge, because the averaging over many particles with somewhat different charges would yield a smoother transition.
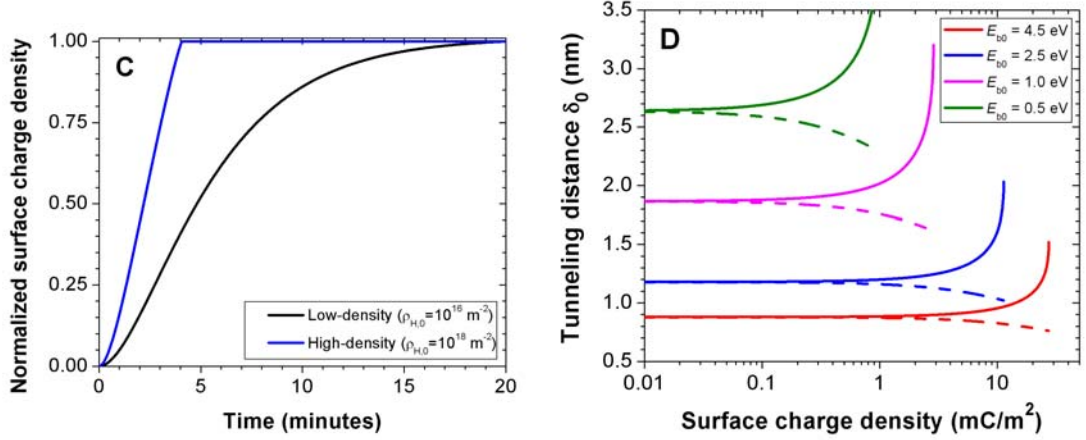
Figure 5.3: **(a)** Normalized surface charge density as a function of time for the low ($\rho_{H,0} = 10^{16}$ m^{-2}), and high ($\rho_{H,0} = 10^{18}$ m^{-2}) limits of the density of trapped electron surface states for $E_{b0} = 4.5$ eV. We use parameters typical for fluidized beds [*Forward et al.*, 2009b], with particle sizes of 100 and 400 μm which both occupy 25% of the volume, and a relative velocity between the particles of 0.1 m/s. The average absolute surface charge density is normalized to its value at 20 minutes. We find a characteristic charging time τ of several minutes, which agrees well with measurements of fluidized beds [*Murtomaa et al.*, 2003; *Revel et al.*, 2003; *Forward et al.*, 2009]. The sharp transition in the charge transfer for the high-density limit is due to the interdependence of the potential difference between colliding particles (ΔV) and the tunneling distance (δ_0), as discussed in the main text and seen in part **(b)**.
(b) The tunneling distance δ_0 (see Eqs. 5.2 – 5.4) for two particles with equal but opposite surface charge density. The solid (dashed) lines denote δ_0 for electrons tunneling from the negatively (positively) charged particle to the positively (negatively) charged particle. The predicted tunneling distance is on the order of 1-2 nm, which is consistent with previous literature estimates [*Harper*, 1967; *Lowell and Rose-Innes*, 1980; *Lowell*, 1979, 1986].

The normalized charging of a binary mixture of two particle sizes with time is shown in Figure 5.3a. Note that the predicted characteristic charging time of several minutes agrees well with measurements in fluidized beds [*Revel et al.*, 2003; *Murtomaa et al.*, 2003; *Forward et al.*, 2009b].

It is noteworthy that, despite the large uncertainty in the value of $\rho_{H,0}$, our charging scheme is in quantitative agreement with measurements even without the use of empirical

parameters (see Chapter 5.4). Indeed, the agreement with measurements is optimal for $\rho_{H,0} \approx 10^{16}$ m^{-2}. In Figure 5.4, we apply this value of $\rho_{H,0}$ to the charging of dust and sand in dust devils and dust storms (see Section 1.2.1), and again find that our charging scheme predicts particle charges of the same order of magnitude as measurements [*Schmidt et al.*, 1998; *Fuerstenau and Wilson*, 2004].
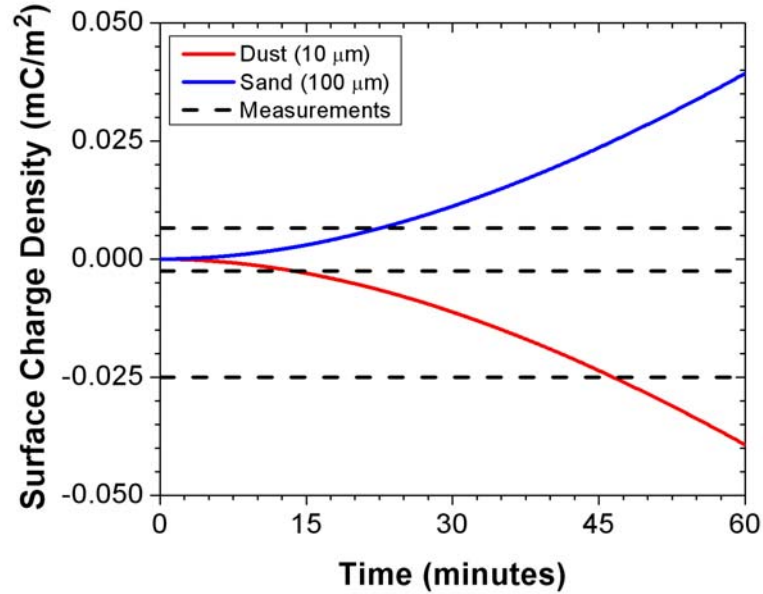
Figure 5.4: Application of our charging scheme to dust storms and dust devils. Charging occurs due to collisions between dust (~10 μm) and sand (~100 μm) (see Section 1.2.1). We used $\rho_{H,0}$ = 10^{16} m^{-2} and E_{b0} = 4.5 eV, assumed a relative velocity of 1 m/s, used mass loadings of 10 g/m^3 for the dust [*Goudie and Middleton*, 2006] and 100 g/m^3 for the sand (Figure 3.4), and used a particle density of 2650 kg/m^3. The predicted characteristic charging time is approximately two hours. The top dashed line indicates measurements of the average charge density of saltating sand [*Schmidt et al.*, 1998], while the bottom two dashed lines denote lower and upper limits of measurements of the negative charge density held by individual 10 μm dust particles [*Fuerstenau and Wilson*, 2004]. Note that the numerical (Eq. 5.15) and analytical (Eq. 5.10) solutions, which respectively do and do not account for the effect of particle charges on subsequent charge transfer during collisions, yield identical results (see also Figure 5.2a).

5.4 DISCUSSION

The present theoretical model is necessarily idealized and neglects certain processes that could affect the charge transfer, especially for particles holding large surface charge densities. First, the model neglects the transfer of low-energy electrons. This assumption is probably justified for low values of the particle charge. However, when particle

charges increase, the energy of low-energy electrons on one particle can be significantly higher than that of empty low-energy states on the oppositely charged particle, which would lead to tunneling of these low-energy electrons. A more detailed model should consider this effect.

A second limitation of the present model is that it does not account for the occurrence of electric discharges between oppositely charged colliding particles. Such discharges can occur if the electric field between the particles exceeds the breakdown electric field described by the 'Paschen law' [*Raizer*, 1997; *Fridman and Kennedy*, 2004],

$$E_{\text{br}} = \frac{BPT_0/T}{C + \ln(PLT_0/T)},$$
(5.16)

where $C = \ln[A/\ln(1/\gamma + 1)]$, P and T are the gas pressure and temperature, and L is the distance over which the discharge occurs. The constants A, B, and γ determine the ionization coefficients [*Raizer*, 1997; *Fridman and Kennedy*, 2004] at $T_0 = 293$ K for different gases. An electric discharge will thus occur if the electric field a distance L from the surface of a charged particle with surface charge density σ exceeds the breakdown field E_{br}. From Gauss' law, the electric field produced by the particle equals

$$E_{\text{p}} = \frac{\sigma R^2}{\varepsilon_0 (R + L)^2}.$$
(5.17)

Solving for the minimum surface charge density σ_{br} at which electric discharges occur for the terrestrial atmosphere (i.e., $P = 10^5$ Pa, $T = 288$ K, $A = 15$ m^{-1}Pa^{-1}, $B = 365$ Vm^{-1}Pa^{-1}, and $\gamma = 0.01$ [*Raizer*, 1997; *Fridman and Kennedy*, 2004]), we find that σ_{br} respectively equals 0.3 and 0.09 mC/m^2 for particles of 10 and 100 μm diameter. Conversely, for the Martian atmosphere (i.e., $P \approx 700$ Pa, $T \approx 230$ K, $A = 15$ m^{-1}Pa^{-1}, $B = 350$ Vm^{-1}Pa^{-1}, and $\gamma = 0.01$ [*Raizer*, 1997; *Fridman and Kennedy*, 2004; Chapter 4]), σ_{br} respectively equals 2.4 and 0.04 mC/m^2 for particles of 10 and 100 μm diameter. For the 100 μm particles, σ_{br} is thus on the order of surface charge densities predicted in Figures 5.2 and 5.4. Depending on the density of trapped high-energy electrons (Fig. 5.2a) and the energy barrier (Fig. 5.2b), the magnitude of the particle charging could thus be limited by the occurrence of 'micro-discharges' between colliding particles, especially for large values of t/τ. Such discharges often occur during experiments with non-identical insulators under

Earth ambient conditions [*Lowell and Rose-Innes*, 1980]. Moreover, terrestrial dust devils have been observed to emit non-thermal microwave radiation [*Ruf et al.*, 2009], which are presumably produced by micro-discharges between colliding particles [*Renno et al.*, 2003].

To allow more flexibility in modeling experiments, a semi-empirical version of the model can be used, in which an effective length scale $\delta_{\text{eff}} = C_{\text{E}}\delta_0$ is used in place of δ_0 in Eqs. (5.11) and (5.15). The empirical parameter C_{E} thus relates the effective distance from the point of contact over which charge is exchanged (δ_{eff}) to the theoretical tunneling distance (δ_0), and is introduced to account for processes that cause the charge transfer for non-idealized particles to differ from our purely theoretical considerations. For example, while our simple model assumes perfectly spherical particles and thus a single point of contact during collisions, natural particles are irregular and will contact each other at many separate locations. Moreover, the transfer efficiency of high-energy electrons within the tunneling distance δ_0 will not be unity, because of the energetic constraints that limit the transition of high-energy electrons to empty low-energy states [*Lowell and Rose-Innes*, 1980; *Lowell and Truscott*, 1986b]. Furthermore, rubbing that may occur during collisions can increase the distance from the 'contact point' for which charge is exchanged beyond the theoretical tunneling distance of Eq. (5.2) [*Lowell*, 1980]. The empirical parameter C_{E} can also account for the fact that the transfer efficiency of high-energy electrons is a function that depends on distance, rather than being a step function at the distance δ_0. Note that C_{E} strongly affects the time constant $\tau = \sum_j N_j \tau_j / \sum_j N_j$ (see Eq. 5.13) with which charging takes place, but does not affect the final charges for large t/τ. Measurements of the characteristic charging time of granular systems of identical insulators could thus determine C_{E} for a particular material without any knowledge of the density of trapped high-energy electrons. Note also that the values of the parameters $\rho_{\text{H},0}$ and C_{E} almost certainly vary by material. Indeed, the density of trapped states is probably related to defects in the crystal structure and thus depends on mechanical surface damage [*Lowell and Truscott*, 1986a, 1986b], while the value of C_{E} probably depends on the material's surface roughness [*Lowell and Rose-Innes*, 1980].

5.5 SUMMARY AND CONCLUSIONS

We show that the widely observed size-dependent triboelectric charging of chemically identical insulators [*Schmidt et al.*, 1998, 1999; *Miura et al.*, 2002; *Zheng et al.*, 2003; *Fuerstenau and Wilson*, 2004; *Inculet et al.*, 2006; *Shinbrot et al.*, 2006; *Forward et al.*, 2009a] is partially due to simple geometrical considerations that produce a net transfer of electrons from larger to smaller particles. This charging mechanism supplements the previously identified 'multiple collisions' charging mechanism [*Lacks et al.*, 2008; *Duff and Lacks*, 2008]. We combined these two related mechanisms into the first quantitative scheme of the size-dependent charging of a granular system of chemically identical insulators. Based solely on theoretical considerations, predictions of our charging scheme are qualitatively and quantitatively consistent with measurements of both the magnitude and the characteristic time scale of the charging. Our theory thus seems to provide an explanation for the hitherto puzzling phenomenon of the size-dependent charging of granular systems of identical insulators.

Our charging scheme can be used to study the electrification of a wide range of granular systems, including fluidized beds [*Revel et al.*, 2003; *Murtomaa et al.*, 2003; *Forward et al.*, 2009a, 2009b], powder handling [*Inculet et al.*, 2006], wind-blown sand and snow [*Schmidt et al.*, 1998, 1999; *Zheng et al.,* 2003; *Shinbrot et al.*, 2006; *Shinbrot and Herrmann*, 2008], dust storms and dust devils (see Section 1.2.1), thunderstorms [*Lowell and Truscott*, 1986b; *Yair*, 2008], and volcanic eruptions [*Miura et al.*, 2002].

Careful measurements are required to further illuminate the basic physical processes underlying the triboelectric charging of identical insulators and to test and refine our charging scheme.

5.6 ACKNOWLEDGEMENTS

5.7 APPENDIX: CHARGE TRANSFER BETWEEN CUBICAL PARTICLES

We showed in Section 5.3.1 that, during collisions between spherical particles, more trapped high-energy electrons transfer from the larger to the smaller particle than vice versa. In this appendix, we show that a similar effect occurs for cubical particles.
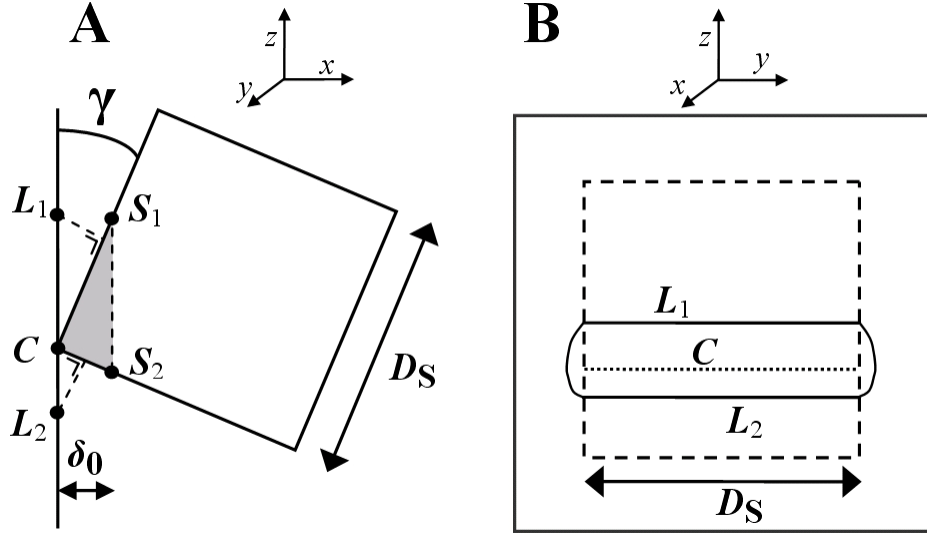
Figure 5.5: (**a**) Schematic in the xz-plane of a collision between a small cubical particle with diameter D_S and a much larger cubical particle with diameter D_L. The distance of the points S_1, S_2, L_1, and L_2 to the opposite particle is exactly δ_0. These points respectively lie at $(\delta_0, \delta_0 / \tan \gamma)$, $(\delta_0, -\delta_0 \tan \gamma)$, $(0, \delta_0 / \sin \gamma)$, and $(0, -\delta_0 / \cos \gamma)$, relative to the point of contact C in the xz-plane. The total area of the smaller cube that lies within a distance δ_0 of the larger cube is thus $A = D_S \Delta CS_1 + D_S \Delta CS_2 + \Delta CS_1 \Delta CS_2$ (see Eq. 5.18), where $\Delta CS_1 = \delta_0 / \sin \gamma$ and $\Delta CS_2 = \delta_0 / \cos \gamma$ are the distances of S_1 and S_2 from C, and the shaded triangle denotes the area $0.5 \Delta CS_1 \Delta CS$.

(**b**) As in (**a**), except for the yz-plane. The outer gray square represents the larger cube, and the dashed rectangle denotes the projection of the smaller cube on the surface of the larger cube. The dotted line represents the line of contact between the particles, and the solid line denotes the points on the larger cube for which the distance to the smaller cube is exactly equal to δ_0. The two semi-ovals are described by the equations $y = \pm\sqrt{\delta_0^2 - z^2 \sin^2 \gamma}$ $(z > 0)$ and $y = \pm\sqrt{\delta_0^2 - z^2 \cos^2 \gamma}$ $(z < 0)$. The total area on the larger cube over which high-energy electrons can tunnel to the smaller cube is thus obtained by integrating these equations (which produces the third term in the brackets on the right-hand side in Eq. 5.19) and adding the result to the area between the lines L_1 and L_2 (which produces the first two terms in Eq. 5.19).

In addition to the assumptions described in Section 5.2, we assume that the difference in the size of the colliding cubical particles is large, such that the collision is

synonomous to that of a cubical particle colliding with a flat plane (Fig. 5.5a). Moreover, for simplicity we neglect variations in the angle of rotation perpendicular to the plane that is illustrated in Fig. 5.5a. Accounting for variations in this angle significantly complicates the below derivation, while it yields the same qualitative result.

From the illustration of the charge transfer in Fig. 5.5a, we find that the number of electrons transferred from the high-energy state of the smaller particle to empty low-energy states on the larger particle equals

$$- \Delta n_{S,H} = - \Delta n_{L,L} = \rho_{H,0} \delta_0 \left(\frac{D_S}{\sin \gamma} + \frac{D_S}{\cos \gamma} + \frac{\delta_0}{\sin \gamma \cos \gamma} \right), \qquad (5.18)$$

where the subscripts S and L respectively refer to the smaller and larger colliding particle, D_S is the radius of the smaller particle, and the angle γ is defined in Fig. 5.5a. Conversely, the number of trapped high-energy electrons transferred from the larger to the smaller particle equals (see Fig. 5.5b)

$$- \Delta n_{L,H} = \Delta n_{S,L} = \rho_{H,0} \delta_0 \left[\frac{D_S}{\sin \gamma} + \frac{D_S}{\cos \gamma} + \frac{\pi \delta_0}{2} \left(\frac{1}{\sin \gamma} + \frac{1}{\cos \gamma} \right) \right]. \qquad (5.19)$$

As was the case with spherical particles, the charge transfer between cubical particles of different sizes is thus asymmetric. This asymmetry is due to the unequal contributions near the side of the small cube (that is, the shaded triangle in Fig. 5.5a for the smaller particle and the ovals in Fig. 5.5b for the larger particle). By subtracting Eqs. (5.18) and (5.19), we find that the net charge transfer experienced by the larger particle equals

$$\Delta q_L = \frac{e \rho_{H,0} \delta_0^2}{\sin \gamma \cos \gamma} \left[\frac{\pi}{2} (\sin \gamma + \cos \gamma) - 1 \right]. \qquad (5.20)$$

The above equations are valid for $|\sin \gamma| \geq \delta_0 / D_S$. Since $D_S \gg \delta_0$ we can safely neglect the small contribution from $|\sin \gamma| < \delta_0 / D_S$. We thus obtain the average charge transfer between colliding particles by integrating over the angle γ

$$\overline{\Delta q_L} \approx \frac{4}{\pi} e \rho_{H,0} \delta_0^2 \int\limits_{\arcsin \frac{\delta_0}{D_S}}^{\pi/4} \frac{\frac{\pi}{2} (\sin \gamma + \cos \gamma) - 1}{\sin \gamma \cos \gamma} d\gamma \approx 2 e \rho_{H,0} \delta_0^2 \left[\left(1 - \frac{2}{\pi} \right) \ln \frac{D_S}{\delta_0} + \ln 2 \right], \qquad (5.21)$$

66

where we again used that $D_S \gg \delta_0$ and that $\cos(\arcsin x) = \sqrt{1-x^2}$. In comparison with Eq. (5.10), the charge transfer between cubical particles is approximately two to four times as large as that between spherical particles.

CHAPTER 6

A COMPREHENSIVE NUMERICAL MODEL OF WIND-BLOWN SAND

6.1 INTRODUCTION

In the previous chapters, we have investigated the effects of sand electrification on saltation on Earth and Mars (Chapters 2, 3, and 4) and derived a quantitative theoretical scheme for the triboelectrification of granular systems of identical insulators, such as saltating sand particles (Chapter 5). In the present Chapter, we describe a comprehensive numerical model of saltation that is the first model capable of reproducing a wide range of field experiments. Note that the present model version neglects the effects of sand electrification, because we focus on developing a model that can reproduce measurements for low to medium shear velocities (<~ 0.5 m/s). However, work is in progress to implement the charging scheme described in Chapter 5 into a future model version [*Kok and Renno*, 2009c].

Numerical models of the different physical processes involved in saltation have been developed by various researchers. *White and Schulz* [1977], *Hunt and Nalpanis* [1985], and *Anderson and Hallet* [1986] were the first to successfully model the trajectories of saltating particles. Building on the success of these initial studies, *Ungar and Haff* [1987] were the first to couple the motion of saltating particles to the retardation of the wind speed near the surface in a simple, steady-state model, in which the trajectories of all saltating particles were assumed identical. Nonetheless, they were able to reproduce some essential features of saltation, such as the near-surface focusing of the wind profiles for different shear velocities (first reported by *Bagnold* [1936]). *Werner* [1990] developed a more comprehensive numerical model of steady-state saltation that allowed for a range of particle trajectories. This model also included a parameterization of the splashing of particles from the soil, which was based on laboratory measurements of particle ejections [*Werner*, 1987]. However, only the more detailed models developed by *Anderson and Haff* [1988, 1991] and *McEwan and Willetts* [1991, 1993] were able to

simulate the development of saltation from inception to steady-state. *Shao and Li* [1999] built on these studies and developed a saltation model as part of a large eddy model that explicitly solved for the wind field. More recently, *Almeida et al.* [2006] coupled a saltation model to the computational fluid dynamics model FLUENT capable of calculating the turbulent wind field in the presence of saltation. While their saltation model assumes identical trajectories and does not explicitly consider the 'splashing' of surface particles, they were able to reproduce empirical expressions for the saltation mass flux. They used this model to study saltation on Mars [*Almeida et al.*, 2008]. *Zheng* and co-workers also developed a numerical model that can reproduce certain essential features of saltation, and were the first to account for the effects of electrostatic forces [*Zheng et al.*, 2006]. Our subsequent study (Chapter 3) indicated that electrostatic forces increase the saltating particle concentration and lower the height of saltation trajectories, thereby possibly resolving the discrepancy between the measured [*Greeley et al.*, 1996; *Namikas*, 2003] and predicted [*Bagnold*, 1941; *Owen*, 1964] height of the saltation layer.

While the models discussed above have provided significant advancements in our understanding of the physics of saltation, they have been unable to accurately reproduce natural saltation. Moreover, these models were generally constrained to saltation of monodisperse particles, while natural saltation occurs over soils containing a range of particle sizes. We here present a comprehensive physically-based numerical model of saltation that can simulate saltation of soils consisting of particles of various sizes. The comprehensive model described in the current chapter is a substantial improvement over the simpler numerical model developed in Chapter 3, because it replaces many of the empirical relationships used in the latter model with physically-based relationships.

Our model shows reasonable to excellent agreement with a variety of experimental data such as the impact threshold, horizontal and vertical profiles of particle mass flux, the wind profile in saltation, and the size distribution of saltating particles. Our model also includes a physically-based parameterization of the splashing of surface particles, which agrees with available laboratory and numerical experiments. To the best of our knowledge, our numerical model is the first capable of reproducing such a wide range of experimental data. Since we use a minimum of empirical relations, we argue that our model can accurately simulate saltation in a variety of physical environments, including

other planets such as Mars [*Almeida et al.*, 2008], saltating snow, and saltation in water. Our model was coded in MATLAB and is freely available by contacting the author.

We describe our model in detail in the next section, compare its results to measurements in Section 6.3, and present conclusions in Section 6.4.

6.2 MODEL DESCRIPTION

We model saltation as the interplay of several processes [*Werner*, 1990; *Anderson and Haff*, 1991; *McEwan and Willetts*, 1991]: (i) the motion of saltating particles, (ii) the modification of the wind profile through momentum transfer between the wind flow and saltating particles, and (iii) the collision of particles with the soil surface and the subsequent ejection or 'splashing' of surface particles into the fluid stream. For simplicity, we simulate particle motion in two dimensions, as previous investigators have also done [e.g., *Werner*, 1990; *Anderson and Haff*, 1991; *McEwan and Willetts*, 1991]. We also neglect the collisions of saltating particles with each other, as well as the effects of electrostatic forces on particle trajectories (see Chapter 3). The effect of both these processes is limited for small to medium shear velocities (i.e., $u^* < {\sim}0.5$ m/s) but probably becomes important for larger shear velocities [*Sorensen and McEwan*, 1996; *Huang et al.*, 2007; see Chapter 3]. We therefore plan to include both mid-air collisions and electrostatic forces in a future model version.

Our numerical model simulates saltation in steady-state (see Figure 6.1). The model uses the logarithmic wind profile known as the "law of the wall" [Prandtl, 1935] to calculate the initial trajectories of saltating particles. The drag exerted by the particles on the wind is then obtained from these trajectories and used to adjust the wind profile. The concentration of saltating particles is calculated using the steady-state condition that the number of particles striking the soil must be equal to the number of rebounding and ejected particles. If the number of rebounding and ejected particles is greater than the number of impacting particles, then the concentration of saltating particles is increased accordingly, which enhances the exchange of momentum with the wind and reduces the near-surface wind speed, causing particles to strike the soil at reduced speed and thereby eject fewer particles. Due to their interdependence, the particle concentration, wind profile, and particle trajectories are calculated iteratively until steady-state is reached (see

Figure 6.1). Because the interaction of saltating particles with the soil surface and the turbulent wind is stochastic (see Sections 6.2.1.2 and 6.2.2), these processes cause variability in the model simulations that can be seen as characteristic of natural saltation. 'Steady-state' saltation as simulated by our model thus entails a dynamic balance that, averaged over many iterations, satisfies the condition that the number of impacting particles is equal to the number of particles that rebound and are ejected from the soil [*Jackson and McCloskey*, 1997; *Anderson and Haff*, 1991].

We discuss each component of the model in detail below. Where possible, we use experimental data to verify the performance of individual model components.
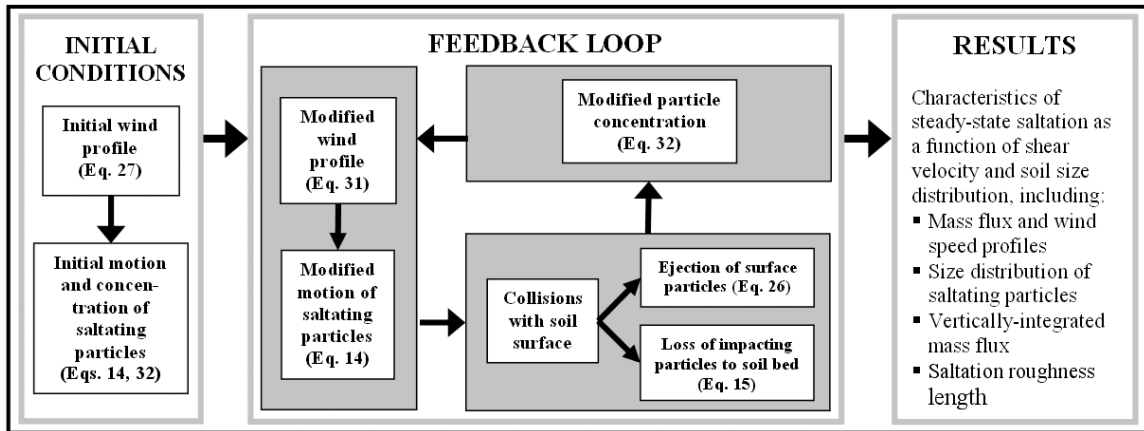
Figure 6.1: Schematic diagram of our numerical saltation model. As in previous studies [*Anderson and Haff*, 1988, 1991; *Werner*, 1990; *McEwan and Willetts*, 1991, 1993], we model saltation by explicitly simulating (i) particle trajectories, (ii) the modification of the wind profile through momentum transfer between the wind flow and saltating particles, and (iii) the collision of particles with the soil surface and the subsequent 'splashing' of surface particles into the fluid stream. The model is initiated by aerodynamically lifting several particles with a speed sufficient to reach a few particle diameters [*Anderson and Haff*, 1991], after which the steps in the feedback loop are repeated until the changes in the saltation trajectories, the wind profile, and the particle concentration are smaller than a specified value in successive iterations. Because of the stochastic interaction of saltating particles with the turbulent wind (Section 6.2.1.2) and the soil surface (Section 6.2.2), steady-state saltation as simulated by our model is a dynamic balance over longer timescales. This is also characteristic of natural saltation [e.g., *Anderson and Haff*, 1991; *Jackson and McCloskey*, 1997]. The model does not incorporate aerodynamic lifting in steady-state saltation, because the fluid shear stress at the surface is below the threshold for lifting (see Section 6.1). For computational efficiency, the model explicitly simulates the trajectories of only a fraction of the particles, and considers those representative of the entire ensemble of saltating particles. Increasing this fraction does not significantly affect the results presented here. The comprehensive model described in the current chapter is a substantial improvement over the simpler numerical model developed in Chapter 3, because it replaces many of the empirical relationships used in the latter model with physically-based relationships.

6.2.1 Particle trajectories

The motion of saltating particles is determined mainly by gravitational and fluid forces. For the present model version, we thus neglect electrostatic forces (see Chapter) and also mid-air collisions [*Sorensen and McEwan*, 1996; *Dong et al.*, 2005; *Huang et al.*, 2007] which affect particle trajectories mostly for large shear velocities (see Section 6.2.6).

6.2.1.1 Fluid forces

The main fluid force affecting particle trajectories is the drag force [e.g., *Anderson and Haff*, 1991],

$$F_d = -\frac{\pi D_p^2}{8} \rho_a C_d v_R \mathbf{v_R},$$
(6.1)

where $\mathbf{v_R} = \mathbf{v} - \mathbf{U}$ is the difference between the particle ($\mathbf{v}$) and wind ($\mathbf{U}$) velocities, and $v_R = |\mathbf{v_R}|$. The drag coefficient (C_d) of natural sand particles is generally larger than that for spherical particles of the same volume, both because their irregular shape produces a larger effective surface area than a sphere and because regions of large curvature can lead to flow separation, which increases the drag [*Dietrich*, 1982]. Detailed measurements of the terminal velocity in water have been used to measure the drag coefficient of natural sand particles [*Dietrich*, 1982; *Camenen*, 2007]. We calculate the drag coefficient of a saltating sand particle using an equation proposed by *Cheng* [1997] that includes the effects discussed above

$$C_d = \left[\left(\frac{32}{Re} \right)^{2/3} + 1 \right]^{3/2},$$
(6.2)

where the particle Reynolds number is given by

$$Re = \frac{\rho_a v_R D_p}{\mu}.$$
(6.3)

Saltating particles also experience lift forces both due to the shearing flow (the 'Saffman force') [*Saffman*, 1965, 1968], and from particle rotation (the 'Magnus force') [*Rubinow and Keller*, 1961]. We calculate these lift forces using the following expressions proposed by *Loth* [2008]

$$F_{\text{saff}} = 1.615 J^* D_{\text{p}}^2 \left(\rho_{\text{a}} \mu \frac{\partial U_{\text{x}}}{\partial z} \right)^{1/2} (\hat{\mathbf{y}} \times \mathbf{v}_{\mathbf{R}}), \text{ and} \qquad (6.4)$$

$$F_{\text{mag}} = \frac{\pi}{8} \rho_{\text{a}} D_{\text{p}}^3 C_{\text{L}\Omega}^* (\mathbf{\Omega}_{\text{p}} \times \mathbf{v}_{\mathbf{R}}), \qquad (6.5)$$

where U_{x} is the horizontal wind speed, $\hat{\mathbf{y}}$ is the unit vector perpendicular to the plane in which particle motion takes place, and J^* is a strong function of the shear of the flow, the kinematic viscosity, and the relative velocity of the particle to the fluid, and is defined by *McLaughlin* [1991]. The normalized spin lift coefficient $C_{\text{L}\Omega}^*$ is given by Eq. 16 in *Loth* [2008] and is ~0.5-0.7 for normal flow conditions in saltation on Earth. Previous studies have assumed $C_{\text{L}\Omega}^* = 1$, which is a good approximation only for Re << 1 [*Rubinow and Keller*, 1961; *White and Schulz*, 1977, *Loth*, 2008], and thus overestimates the lift force caused by particle spin [*Hunt and Nalpanis*, 1985; *Shao*, 2000]. The particle angular velocity Ω_{p} is defined as positive for topspin (i.e., the particle rotates as if rolling in the same direction as it is moving), in which case the lift force is also positive (i.e., pointing upwards). Experiments have shown that saltating particles predominantly have topspin, with Ω_{p} in the range of 100 - 1000 rev/s [*Chepil and Woodruff*, 1963; *White and Schulz*, 1977; *White*, 1982; *Xie et al.*, 2007; *Zou et al.*, 2007]. A likely reason for the predominance of topspin is that the shearing flow exerts a moment on the particles that produces topspin. Moreover, the friction on a particle's underside upon collision with the soil surface also produces torques that favor topspin over backspin. We assume that, after colliding with the surface, saltating particles have an initial spin of $\Omega_{\text{p},0} \approx 400 \pm 500$ rev/s, as suggested by experiments [*Chepil and Woodruff*, 1963; *White and Schulz*, 1977; *White*, 1982; *Xie et al.*, 2007; *Zou et al.*, 2007]. After leaving the surface, the particle spin is affected by the shear of the flow (which imparts topspin), and by viscous dissipation (which reduces the particle spin). Thus, after stochastically determining the particle's spin upon leaving the surface, we calculate the particle spin as a function of time by numerically integrating the differential equation [*Anderson and Hallet*, 1986; *Loth*, 2008]

$$\frac{d\Omega_{\text{p}}}{dt} = \frac{60\mu}{\rho_{\text{p}} D_{\text{p}}^2} \left(\frac{1}{2} \frac{\partial U_{\text{x}}}{\partial z} - \Omega_{\text{p}} \right), \qquad (6.6)$$

where the first term in the brackets on the right-hand side represents the moment exerted by the shearing flow, and the second term denotes viscous dissipation. We neglect forces due to particle rotation that are not in the *xz*-plane (see Figure 6.2) [*Xie et al.*, 2007].

The Saffman force due to the shearing flow is very small, except very close to the surface where the shear is large. In fact, sensitivity studies with our model indicate that the Saffman force can be neglected without measurably affecting particle trajectories. The Magnus lift force due to particle rotation has typical values of a few percent of the particle's weight and therefore does significantly affect particle trajectories, as also indicated by laboratory studies [*White and Schulz*, 1977; *White*, 1982; *Zou et al.*, 2007].
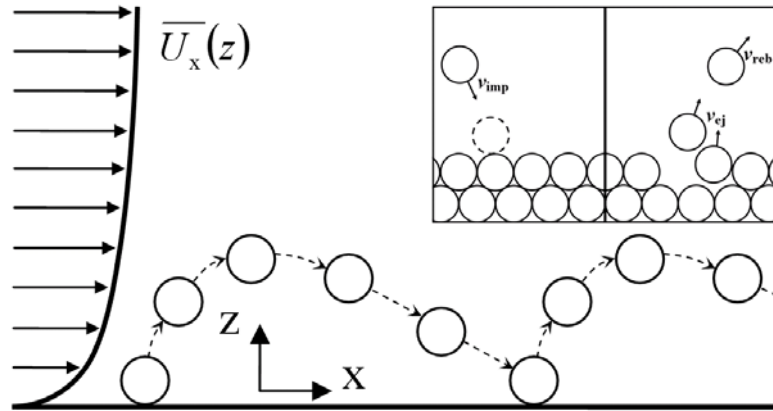
Figure 6.2: Schematic representation of saltation, showing the logarithmic wind profile $\overline{U_x}(z)$ (see Section 6.2.3) to the left of an idealized spherical sand particle propelled by the wind and bouncing along the surface. After lift-off from the surface, saltating particles gain horizontal momentum from the wind, which is partially converted into vertical momentum after colliding with the surface and rebounding. The inset shows a schematic representation of a saltating particle approaching the soil surface (left) and rebounding from it and ejecting (or 'splashing') several surface particles (right).

6.2.1.2 Effect of turbulence on particle trajectories

Previous numerical models of saltation have often neglected the effects of turbulence on particle trajectories [e.g., *Anderson and Haff*, 1988; *McEwan and Willetts*, 1991], despite the fact that turbulence can significantly affect the trajectories of particles smaller than ~250 μm [*Anderson*, 1987]. We therefore do include the effects of turbulence on particles trajectories.

The wind speed can be decomposed into the average wind speed and the turbulent fluctuation:

$$U_x = \overline{U_x} + U_x'; \; U_z = \overline{U_z} + U_z' \tag{6.7}$$

where $\overline{U_x}$, $\overline{U_z}$, U_x', and U_z' are respectively the time-averaged and turbulent horizontal and vertical components of the wind speed at a given height. In the case studies presented in this chapter, we assume horizontal flow (i.e., $\overline{U_z} = 0$). The calculation of $\overline{U_x}$ in the near-surface layer where saltation takes place (the 'saltation layer') is discussed in Section 6.2.3. The turbulent fluctuation experienced by a fluid parcel moving with the flow can be described statistically by [*Van Dop et al.*, 1985; *Wilson and Sawford*, 1996]

$$U_z'(t+dt) - U_z'(t) = -\frac{U_z'(t)}{T_L}dt + n_G\sigma_w\sqrt{2dt/T_L} \; , \tag{6.8}$$

where a similar equation describes U_x'. Eq. (6.8) has the discretized solution

$$U_z'(t+\Delta t) = U_z'(t)\exp(-\Delta t/T_L) + n_G\sigma_w\sqrt{2}\left[1 - \exp\left(-\sqrt{\Delta t/T_L}\right)\right], \tag{6.9}$$

which in the limit $\Delta t \rightarrow dt$ reduces to Eq. (6.8). The model time step Δt is always set smaller than the Lagrangian time scale (T_L), and n_G is a Gaussian distributed random number with zero mean and unit standard deviation. For homogeneous, isotropic turbulence, the standard deviations of the horizontal and vertical turbulent wind speeds equal

$$\sigma_u = b_u \kappa z \left(\frac{\partial \overline{U_x}}{\partial z}\right) \; ; \; \sigma_w = b_w \kappa z \left(\frac{\partial \overline{U_x}}{\partial z}\right), \tag{6.10}$$

where $b_u = 1.4 \pm 0.1$ and $b_w = 2.5 \pm 0.1$ [*Hunt and Weber*, 1979; *Shao*, 1995; *Nishimura and Hunt*, 2000], and where $\kappa = 0.40$ is the von Kármán constant. The Lagrangian time scale T_L represents the approximate time scale over which the velocities experienced by a fluid parcel at times t and $t + T_L$ are statistically related. Since measurements are generally made in a stationary frame of reference, it is notoriously difficult to measure the Lagrangian time scale [*Leuning*, 2000]. To the best of our knowledge, there have been no detailed studies of this time scale in saltation layers. However, the Lagrangian time scale of turbulent flow in forest and vegetation canopies has been studied in detail [*Raupach et al.*, 1996; *Leuning et al.*, 2000]. We thus use the analogy between turbulent flows in forest canopies and saltation layers [*Raupach*, 1991], and define T_L following Eqs. (6.9) and (6.10) of *Leuning et al.* [2000] by equating the canopy height h_c to the height below which the bulk (i.e., 95 %) of the saltation mass flux occurs.
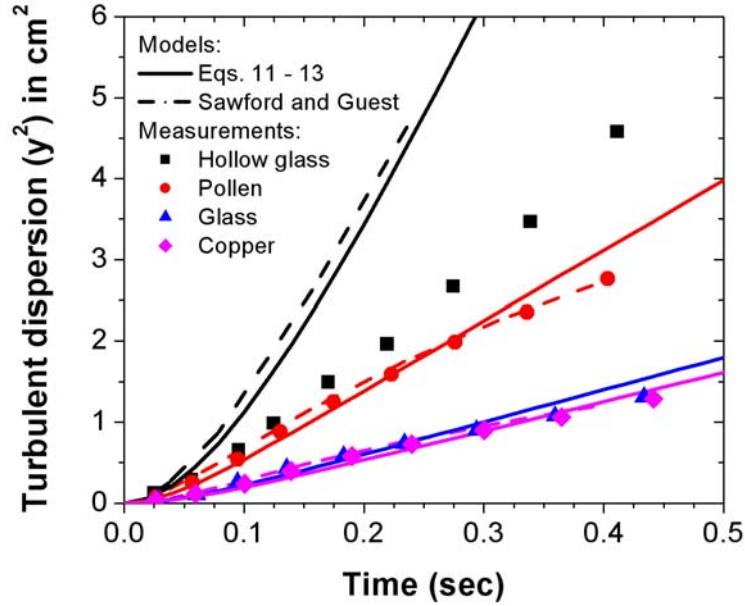
Figure 6.3: Turbulent dispersion perpendicular to the mean flow as measured by *Snyder and Lumley* [1971] for 46.5 μm diameter hollow glass (0.26 g/cm³; black squares), 87.0 μm pollen (1.0 g/cm³; red circles), 87.0 μm solid glass (2.5 g/cm³; blue triangles), and 46.5 μm copper (8.9 g/cm³; magenta diamonds) particles. Included for comparison are the turbulent dispersion simulated for similar particles by the model of *Sawford and Guest* [1991] (dashed black and colored lines) and by Eqs. (6.9) – (6.12) (solid black and colored lines). Good agreement between model predictions and measurements can be seen, except for the hollow glass particles which are the lightest of the four kinds of particles and are least characteristic of saltating particles.

Eqs. (6.8) – (6.10) describe the turbulent fluctuation of the wind speed experienced by a particle moving along the flow streamline. However, gravitational forces and inertia cause the movement of saltating particles to deviate from that of fluid parcels [*Anderson*, 1987; *Sawford and Guest*, 1991]. The time scale T_L* over which the fluctuations in wind speeds experienced by a saltating particle remain statistically correlated is thus shorter [*Csanady*, 1963], because a particle with non-zero velocity relative to the flow requires less time to traverse a turbulent eddy. Although these effects are still not fully understood [*Reynolds*, 2000], *Sawford and Guest* [1991] showed that a reasonable approximation for T_L* for use with the fluctuation of the vertical flow speed is

$$T_L^* = T_L \left[1 + \left(\beta v_R / \sigma_w \right)^2 \right]^{-1/2} , \qquad (6.11)$$

where $\beta = T_L/T_E$ is the ratio of the Lagrangian and Eulerian time scales, which is uncertain but is of order unity [*Sawford and Guest*, 1991; *Reynolds*, 2000; *Anfossi et al.*, 2006]. For horizontal velocity components (i.e., perpendicular to gravity),

$$T_L^* = T_L \left[1 + \left(2\beta v_R / \sigma_u \right)^2 \right]^{-1/2}. \tag{6.12}$$

To test the accuracy of Eqs. (6.9) – (6.12), we used our model to simulate wind tunnel measurements of the dispersion of solid particles (see Figure 6.3) [*Snyder and Lumley*, 1971]. As in *Sawford and Guest* [1991], we found poor agreement between our model and the results of experiments for the lightest particle (47 μm hollow glass), but found excellent agreement for the heavier particles (47 μm copper, 87 μm glass, and 87 μm corn pollen). Since the weight and relaxation time of particles that show good agreement are similar to those of saltating particles, we use the above parameterization in our model.

We neglect the effect of saltating particles on the turbulence level (i.e., σ_u and σ_w), because measurements indicate that such effects are small [*Taniere et al.*, 1997; *Nishimura and Hunt*, 2000].

6.2.1.3 Full equations of motion

We simulate the particle trajectories due to the gravitational and fluid forces described above. The full equations of motion are:

$$ma_x = -\frac{\pi}{8} D_p^2 \rho_a \left[C_d v_R (v_x - U_x) + D_p C_{L\Omega}^* \Omega_p (v_z - U_z) + \frac{12.92}{\pi} J^* \left(\frac{\mu}{\rho_a} \frac{\partial \overline{U_x}}{\partial z} \right)^{1/2} (v_z - U_z) \right], \text{ and} \tag{6.13a}$$

$$ma_z = -\frac{\pi}{8} D_p^2 \rho_a \left[C_d v_R (v_z - U_z) + D_p C_{L\Omega}^* \Omega_p (v_x - U_x) + \frac{12.92}{\pi} J^* \left(\frac{\mu}{\rho_a} \frac{\partial \overline{U_x}}{\partial z} \right)^{1/2} (v_x - U_x) \right] - mg, \tag{6.13b}$$

where m is the particle's mass, v_x, v_z, a_x, and a_z are respectively the particle speeds and accelerations in the x and z directions, and $g = 9.8$ m/s^2 is the gravitational acceleration. The first term on the right-hand side accounts for fluid drag, the second for particle spin, and the third for the Saffman force. The model uses the 4th-order Adams-Moulton method [*Hairer et al.*, 1993] to numerically integrate the equations of motion and obtain the particle trajectories. In order to lower the computational cost, the model randomly selects a number of saltating particles specified by the user, calculates their trajectories, and considers those to represent the entire ensemble of saltating particle trajectories. Increasing the number of simulated saltating particle trajectories beyond the number used to obtain the results presented in this chapter does not significantly affect the model results.

6.2.2 Particle collisions with the surface

The collision of saltating particles with the surface (Figure 6.2) is a key physical process in saltation [*Anderson and Haff*, 1991; *Shao*, 2000]. Saltating particles strike the soil nearly horizontally, at ~5-15° from horizontal, and generally rebound at angles of ~15-70° from horizontal [*Anderson and Haff*, 1988, 1991; *McEwan and Willetts*, 1985, 1986, 1989; *Nalpanis et al.*, 1993; *Rice et al.*, 1995]. The collision of saltating particles with the soil thus converts horizontal momentum into vertical momentum [*Wang et al.*, 2008]. This is essential, as it allows saltating particles to replenish the vertical momentum that is dissipated through fluid drag. Moreover, particles striking the soil can dislodge and eject particles from the surface in a process termed 'splashing' [*Bagnold*, 1973; *Ungar and Haff*, 1987].

6.2.2.1 The rebounding particle

While particle trajectories can be calculated based on simple physical principles (see Section 6.2.1), the collision of saltating particles with the soil surface is inherently a stochastic process. For example, not all saltating particles rebound from the surface, even when they impact it at high speed [*Mitha et al.*, 1986; *Anderson and Haff*, 1991]. The probability that a saltating particle will rebound upon impact can be approximated by [*Anderson and Haff*, 1991]

$$P_{\mathrm{reb}} = B\left[1 - \exp\left(- \gamma v_{\mathrm{imp}}\right)\right], \tag{6.14}$$

where v_{imp} is the speed with which the particle impacts the surface. *Mitha et al.* [1986] determined the parameter B to be 0.94 for 4 mm steel particles, while the 2-dimensional numerical simulations of *Anderson and Haff* [1991] found a similar value of $B \approx 0.95$ for 230 and 320 μm sand particles. To the best of our knowledge, the parameter γ has not been experimentally determined, but the numerical simulations of *Anderson and Haff* [1988, 1991] indicate that it is of order 2 s/m.

We use results of laboratory and numerical studies to describe the velocity of rebounding particles [*White and Schulz*, 1977; *Mitha at al.*, 1986; *Anderson and Haff*, 1991; *McEwan and Willetts*, 1991; *Nalpanis et al.*, 1993; *Rice et al.*, 1995; *Rioual et al.*, 2000; *Oger et al.*, 2005; *Beladjine et al.*, 2007; *Kang et al.*, 2008]. Recent laboratory experiments have shown that the fraction of kinetic energy retained by the rebounding

particle is approximately normally distributed [*Wang et al.*, 2008] while the rebounding angle approximately follows an exponential distribution [*Kang et al.*, 2008; *Willetts and Rice*, 1985, 1986; *McEwan and Willetts*, 1991; *Rice et al.*, 1996]. We thus take the kinetic energy of the rebounding particles to be 45 ± 22 % of the impacting kinetic energy, and the rebound angle as an exponential distribution with a mean of 40° from horizontal.

6.2.2.2 Ejection speed of splashed surface particles

In steady-state saltation, the loss of particles through the process represented by Eq. (6.14) is balanced by the 'splashing' of surface particles. The 'splash function,' which describes the number and velocity of the ejected surface particles as a function of the velocity of the impacting particle [*Ungar and Haff*, 1987] is thus a key component of numerical models of saltation [*Werner*, 1990; *Anderson and Haff*, 1988, 1991; *McEwan and Willetts*, 1991, 1993; *Shao and Li*, 1999]. Instead of using an empirical expression for the splash function that is based on the results of laboratory or numerical experiments, as most previous models have done, we derive a physically based expression of the splash function below.

The ejection of particles from the surface by impacting saltating particles is constrained by the conservation of both energy and momentum. These constraints can be expressed as

$$\varepsilon_{\mathrm{reb}} + \varepsilon_{\mathrm{ej}} + \varepsilon_{\mathrm{F}} = 1 \text{, and} \tag{6.15a}$$

$$\alpha_{\mathrm{reb}} + \alpha_{\mathrm{ej}} + \alpha_{\mathrm{F}} = 1 \text{,} \tag{6.15b}$$

where ε and α respectively refer to the partitioning of energy and momentum, and the subscripts refer to the fraction of the total energy or momentum contained in the rebounding particle (reb), the ejected particles (ej), and that lost through frictional processes (F). In order to derive a physically-based expression of the number and speed of ejected particles, we need to determine whether energy conservation or momentum conservation is the dominant constraint on the ejection of surface particles. To determine this, we unrealistically neglect friction (i.e., $\varepsilon_{\mathrm{F}} = \alpha_{\mathrm{F}} = 0$) in the collision of a particle of mass m_{imp} with a bed of particles with mass m_{ej}, such that we can obtain the maximum

number of particles that can be ejected without violating conservation of energy (N_{max}^{E}) or momentum (N_{max}^{M}). This yields

$$N_{max}^{E} = \frac{(1 - \varepsilon_{reb})m_{imp}v_{imp}^{2}}{m_{ej}\langle v_{ej}^{2}\rangle + 2\phi} \text{, and} \tag{6.16a}$$

$$N_{max}^{M} = \frac{(1 - \alpha_{reb})m_{imp}v_{imp}}{m_{ej}\langle v_{ej}\rangle} \text{,} \tag{6.16b}$$

where ϕ is the energy with which soil particles are bonded with each other, $\langle v_{ej}\rangle$ is the ensemble-averaged ejected particle speed (that is, the speed of ejected particles averaged over many impacts on the soil surface of a particle with a given speed), and $\langle v_{ej}^{2}\rangle$ is the ensemble-averaged square of the ejected particle speed.
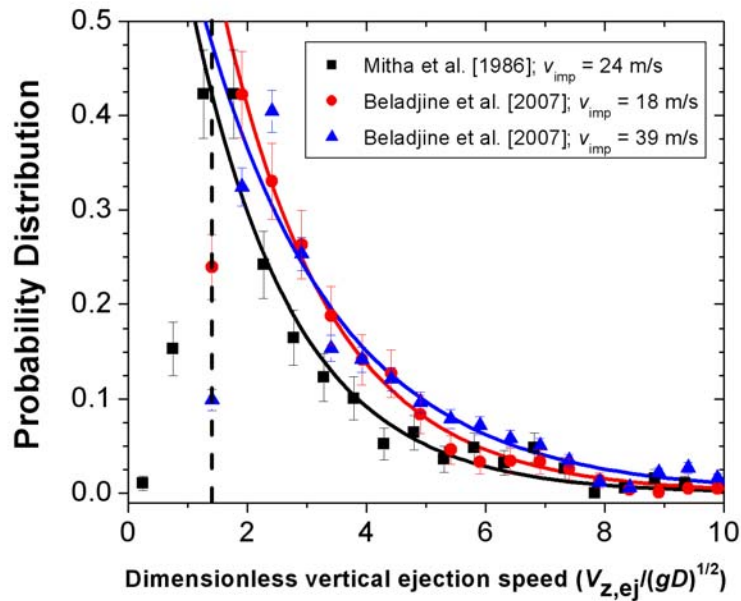
Figure 6.4: Probability distribution of the dimensionless vertical ejection speed. Shown are experimental results for 4 mm steel particles impacting a bed of similar particles at 24 m/s (black squares) [*Mitha et al.*, 1986], and for 6 mm PVC particles impacting at 18 m/s (red circles) and 39 m/s (blue triangles) [*Beladjine et al.*, 2007]. The data above the threshold for which particle detection is reliable (dashed line) [*Beladjine et al.*, 2007] are well-described by exponential distributions (black, red, and blue solid lines). Error bars are derived from the total number of particle counts contained in each data point.

In order to compare $N_{\max}^E$ and $N_{\max}^M$ we need to relate $\left\langle v_{\mathrm{ej}}^2 \right\rangle$ to $\left\langle v_{\mathrm{ej}} \right\rangle$. Such a relation can be obtained by assuming a functional form for the probability distribution $P(v_{\mathrm{ej}})$ of the speed of ejected particles. The numerical simulations of *Anderson and Haff* [1991] found that $P(v_{\mathrm{ej}})$ takes the form of an exponential distribution, which is also suggested by experimental results (see Figure 6.4). We thus take [*Werner*, 1990; *Sorensen*, 1991; *Anderson and Haff*, 1991],

$$P(v_{\mathrm{ej}}) = \frac{\exp\left(-v_{\mathrm{ej}} / \left\langle v_{\mathrm{ej}} \right\rangle\right)}{\left\langle v_{\mathrm{ej}} \right\rangle}. \tag{6.17}$$

We find from Eq. (6.17) that $\left\langle v_{\mathrm{ej}}^2 \right\rangle = 2 \left\langle v_{\mathrm{ej}} \right\rangle^2$, which we combine with Eq. (6.16) to obtain the critical impact speed v_{imp}^{crit} at which the constraints posed by energy and momentum conservation are equally restricting (i.e., where $N_{\max}^E = N_{\max}^M$). This yields

$$v_{\mathrm{imp}}^{crit} = \frac{2}{1 + \alpha_{\mathrm{reb}}} \left[\left\langle v_{\mathrm{ej}} \right\rangle + \phi / m_{\mathrm{ej}} \left\langle v_{\mathrm{ej}} \right\rangle\right] \approx \frac{2 \left\langle v_{\mathrm{ej}} \right\rangle}{1 + \alpha_{\mathrm{reb}}}, \tag{6.18}$$

where we used that $\varepsilon_{\mathrm{reb}} = \alpha_{\mathrm{reb}}^2$ and assumed that $\phi << m_{\mathrm{ej}} \left\langle v_{\mathrm{ej}} \right\rangle^2$ for loose sand, as is typical for saltation on dry dunes and beaches. When $v_{\mathrm{imp}} << v_{\mathrm{imp}}^{crit}$, we have that $N_{\max}^E << N_{\max}^M$, such that energy conservation constrains the number of surface particles that can be ejected. Conversely, when $v_{\mathrm{imp}} >> v_{\mathrm{imp}}^{crit}$, we find that $N_{\max}^E >> N_{\max}^M$, such that momentum conservation becomes the main constraint. Since the speed of ejected particles is approximately an order of magnitude smaller than the impacting speed [e.g., *Rice et al.*, 1995], we find that generally $v_{\mathrm{imp}} >> v_{\mathrm{imp}}^{crit}$ and thus that $N_{\max}^E >> N_{\max}^M$. This implies that the splashing of loose sand particles from the surface by saltating particles is limited primarily by momentum conservation, and not as much by energy conservation. While the inclusion of frictional processes will affect the exact value of v_{imp}^{crit}, it is unlikely to alter this general conclusion. Note however that the ejection of dust particles from the soil is rather different, because in this case ϕ is not small. Therefore, energy conservation might be the dominant constraint limiting the number of ejected dust particles. Indeed, this is what measurements by *Shao et al.* [1993] suggest.

81

We thus impose conservation of momentum on the number of surface particles that can be ejected, and thereby find that

$$N(v_{\text{imp}}) m_{\text{ej}} \langle v_{\text{ej}} \rangle = \langle \alpha_{\text{ej}} \rangle m_{\text{imp}} v_{\text{imp}}, \tag{6.19}$$

where $\langle \alpha_{\text{ej}} \rangle$ is the ensemble-averaged fraction of the impacting momentum that is spent on splashing particles from the surface, and N is the average number of ejected particles, which depends on the particle impact speed v_{imp}. We neglect the dependence of N on the impact angle [*Beladjine et al.*, 2007], because the range of angles with which saltating particles impact the surface is relatively narrow [e.g., *Wang et al.*, 2008]. Both laboratory and modeling studies suggest that the number of ejected particles scales approximately linearly with the impact speed [*Anderson and Haff*, 1988, 1991; *McEwan and Willetts*, 1991; *Rice et al.*, 1996; *Rioul et al.*, 2000; *Oger et al.*, 2005; *Beladjine et al.*, 2007],

$$N \approx A v_{\text{imp}}. \tag{6.20}$$

Dimensional analysis [*Beladjine et al.*, 2007] and conservation of momentum suggests that the parameter A can be rewritten as

$$A = \frac{a}{\sqrt{gD}} \frac{m_{\text{imp}}}{m_{\text{ej}}}, \tag{6.21}$$

where D is a typical particle size (~250 μm for saltation on Earth), and a is a dimensionless constant that is independent of the impacting velocity and the masses of the impacting and ejected particles, and lies in the range of $0.01 - 0.05$ [*Willetts and Rice*, 1985, 1986, 1989; *McEwan and Willetts*, 1991; *Rice et al.*, 1995, 1996]. Combining Eqs. (6.19)-(6.21) then yields the simple expression

$$\langle v_{\text{ej}} \rangle = \frac{\langle \alpha_{\text{ej}} \rangle \sqrt{gD}}{a}. \tag{6.22}$$

Thus, assuming that the fraction of momentum spent on splashing particles from the surface ($\langle \alpha_{\text{ej}} \rangle$) does not depend on impact speed, the average speed of ejected particles should be independent of the impact speed. This is indeed consistent with results for large impact speeds from laboratory experiments; Werner [1987, 1990] found that $\langle v_{\text{ej}} \rangle$ remains approximately constant for a dimensionless impact speed larger than ~68, and *Rioul et al.* [2000] and *Beladjine et al.* [2007] reported similar results.

However, Eq. (6.22) is only valid for large impact speeds, where $N \gg 1$, such that momentum and energy conservation are automatically satisfied by the statistical (ensemble) approach of Eqs. (6.17, 6.19). For smaller impact speeds, for which $N \sim 1$, the speed of ejected particles can no longer be approximated by Eq. (6.22), because momentum and energy conservation do not allow the high-speed tail of the exponential distribution of impact speeds of Eq. (6.17) with $\langle v_{ej} \rangle$ defined by Eq. (6.22). Thus, for smaller impact speeds, the discrete nature of the ejection process (that is, $N \approx 1$ rather than $N \gg 1$) provides explicit constraints on momentum and energy conservation that are not automatically satisfied by Eqs. (6.17) and (6.19),

$$\sum_i m_{ej}^i v_{ej}^i \leq \left(1 - \alpha_{reb}\right) m_{imp} v_{imp} \text{, and} \tag{6.23a}$$

$$\sum_i m_{ej}^i v_{ej}^{i\,2} \leq \left(1 - \alpha_{reb}^2\right) m_{imp} v_{imp}^2 , \tag{6.23b}$$

where the superscript i sums over all the ejected particles, and where we again used that $\varepsilon_{reb} = \alpha_{reb}^2$. When the impacting particle has only enough energy to at most eject one surface particle, Eq. (6.23) thus truncates the probability distribution of ejection speeds given by Eq. (6.17). This leads to a decrease in the average ejected particle speed for small impact speeds, as was indeed found by numerical [*Anderson and Haff*, 1988, 1991] and experimental studies with natural sand [*Willets and Rice*, 1985, 1986, 1989; *Rice et al.*, 1995]. Note that the constraints of energy and momentum conservation described by Eq. (6.23) are automatically satisfied in Eqs. (6.17) and (6.19) when $N \gg 1$.

Figure 6.5 compares $\langle v_{ej} \rangle$ obtained from a Monte Carlo simulation using Eqs. (6.17, 6.20, 6.21, 6.23) with results from experimental [*Willetts and Rice*, 1985, 1986, 1989; Rice et al., 1995] and numerical [*Anderson and Haff*, 1988, 1991] studies. The increase of $\langle v_{ej} \rangle$ at low v_{imp} is reproduced by our analytical model, as is the independence of $\langle v_{ej} \rangle$ for larger v_{imp} reported in the literature [*Werner*, 1987, 1990; *Haff and Anderson*, 1993; *Rioual et al.* 2000; *Oger et al.*, 2005; *Beladjine et al.*, 2007]. The average dimensionless ejection speed presented in Figure 6.5 can be described by the expression

$$\frac{\langle v_{ej} \rangle}{\sqrt{gD}} = \frac{\langle \alpha_{ej} \rangle}{a} \left[1 - \exp\left(-\frac{v_{imp}}{40\sqrt{gD}} \right) \right], \tag{6.24}$$

such that Eq. (6.22) is retrieved for very large dimensionless impact speeds, where $N \gg 1$.

Eq. (6.24) thus constitutes a physically-based expression of the speed of ejected particles, which shows good agreement with experiments (Figure 6.5). The distribution of ejection speeds for the whole range of N is well-described by the exponential distribution of Eq. (6.17), with $\langle v_{ej} \rangle$ given by Eq. (6.24).
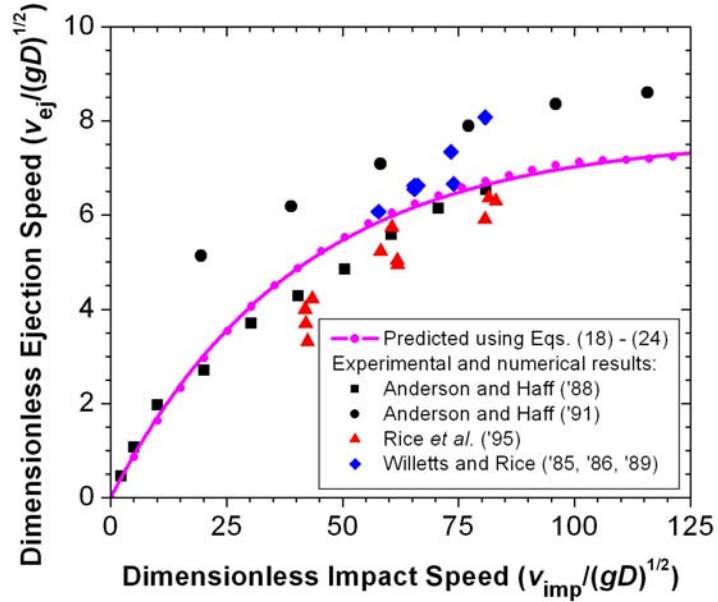
Figure 6.5: The average dimensionless speed of ejected surface particles ($\overline{v_{ej}}/\sqrt{gD}$) as a function of the dimensionless speed of the impacting particle ($v_{imp}/\sqrt{gD}$). We used Eqs. (6.17) – (6.23) to perform a Monte Carlo simulation (magenta circles) of particles impacting a bed of similar particles, for which we used parameters as specified in Table 6.1. The model results do not depend on the particle size. The magenta solid line represents the fit to these results as given by Eq. (6.24). Experimental results from *Willetts and Rice* [1985, 1986, 1989] (red triangles) denote the average speed of particles splashed from a bed of mixed particles by a medium-sized (250-355 μm) impacting particle, whereas the results from *Rice et al.* [1995] (blue diamonds) represent the average speed by which fine (150-250 μm), medium (250-355 μm), and coarse (355-600 μm) particles are ejected from a bed of mixed particles by an impacting particle of the same size. The numerical studies of *Anderson and Haff* [1988] and [1991] (black squares and circles, respectively) were performed for 2-dimensional sand particles of 1 mm and 230-320 μm diameter, respectively. Results from similar experimental and numerical studies with particles other than sand grains [e.g., *Oger et al.*, 2005; *Beladjine et al.*, 2007] are omitted. The sphericity and the elastic and friction coefficients of such particles differ from those of natural sand, which likely affects the experimental results [*Mitha et al.*, 1986; *Anderson and Haff*, 1991].

6.2.2.3 Ejection angle of splashed surface particles

Since the collision of soil particles with the surface converts horizontal momentum into vertical momentum, there are no convenient energetic constraints on the angles at which particles are ejected. We therefore use the consensus result of laboratory and numerical studies that the angle at which particles are ejected can be described by an exponential distribution with a mean of 50 degrees from horizontal [*Willetts and Rice*, 1985, 1986, 1989; *Anderson and Haff*, 1988, 1991; *Werner*, 1990; *McEwan and Willetts*, 1991; *Rice et al.*, 1995, 1996].

6.2.2.4 Ejection of particles from mixed soils

The above analysis for the splash function can be easily extended to mixed soils by assuming that a particle's chance of being ejected from the surface depends on its cross-sectional area [*Rice et al.*, 1995; *Shao and Mikami*, 2005]. For a mixed soil, the number of particles ejected from each particle size bin then becomes

$$N^k = \frac{a}{\sqrt{gD}} \frac{m_{\mathrm{imp}}}{m_{\mathrm{ej}}^j} \left(\frac{D_{\mathrm{ej}}^k}{D_{\mathrm{imp}}} \right)^2 v_{\mathrm{imp}} f^k = \frac{a}{\sqrt{gD}} \frac{D_{\mathrm{imp}}}{D_{\mathrm{ej}}^k} v_{\mathrm{imp}} f^k, \qquad (6.25)$$

where D_{imp} and D_{ej}^k are the diameter of the impacting and ejected particles, and f^k denotes the mass fraction of the kth particle bin of the soil's particle size distribution.

6.2.3 Wind profile

The wind profile over an aerodynamically rough surface in the absence of saltating particles [*Prandtl*, 1935; *Bagnold*, 1941] is given by

$$\overline{U_{\mathrm{x}}}(z) = \frac{u*}{\kappa} \ln\left(\frac{z}{z_0} \right), \qquad (6.26)$$

where z is the vertical distance from the surface, $u*$ is the wind shear velocity or friction velocity and is a measure of the gradient of the fluid flow field, and $z_0 \approx D/30$ is the surface roughness [*Nikuradse*, 1933], where D is the characteristic size of soil particles.

The initial wind profile given by Eq. (6.26) is modified by the transfer of momentum between the wind flow and saltating particles. The amount of horizontal fluid momentum that fluxes into the saltation layer depends directly on the shearing of the

flow, and is equal to the fluid shear stress $\tau = \rho_a u *^2$ above the saltation layer. At steady state, this flux of horizontal momentum into the saltation layer is partitioned between saltating particles (τ_p) and the fluid (τ_a), such that [*Raupach*, 1991]

$$\tau = \tau_a(z) + \tau_p(z). \tag{6.27}$$

The fluid momentum flux $\tau_a(z)$ in the saltation layer is a function of the velocity gradient,

$$\tau_a(z) = \rho_a \left[\kappa z \frac{\partial \overline{U_x}(z)}{\partial z} \right]^2, \tag{6.28}$$

and $\tau_a(z) = \tau$ for z above the saltation layer. Combining Eqs. (6.27) and (6.28) then yields

$$\frac{\partial \overline{U_x}(z)}{\partial z} = \frac{1}{\kappa z} \sqrt{u *^2 - \tau_p(z)/\rho_a}, \tag{6.29}$$

with the particle momentum flux given by [*Shao*, 2000]

$$\tau_p(z) = \sum_i m^i v_x^i(z) - \sum_j m^j v_x^j(z), \tag{6.30}$$

where the superscripts i and j respectively sum over all descending and ascending particles that pass the height z per unit area and unit time.

We calculate $\tau_p(z)$ as a function of the particle trajectories (see Section 6.2.1) and the concentration of saltating particles (see below), and use it to numerically integrate Eq. (6.29) to obtain the wind profile in the saltation layer

6.2.4 Particle concentration

The concentration of saltating particles is affected by both the capture of impacting saltating particles by the soil bed (Eq. 6.14) and the production of new saltating particles through splashing (Eq. 6.25). The concentration n^k of saltating particles in the particle bin k is thus described by

$$\frac{dn^k}{dt} = \sum_i \frac{a}{\sqrt{gD}} \frac{D_{imp}^i}{D_{ej}^k} v_{imp}^i f^k - \sum_{j_k} 1 - B\left[1 - \exp\left(-\mathcal{W}_{imp}^{j_k}\right)\right], \tag{6.31}$$

where i and j_k respectively sum over all saltating particles and over all particles in bin k that are impacting the soil surface per unit time and unit area. The first term on the right-hand side accounts for the production of saltating particles through splashing, and the

second term accounts for the loss of saltating particles to the soil. As the model progresses through successive iterations (see Figure 6.1), it uses Eq. (6.31) to converge to the steady-state particle concentration. Indeed, if the number of splashed surface particles is greater than the number of saltating particles settling back to the soil surface, then the concentration of saltating particles increases. This augments the particle momentum flux and thus decreases the wind speed (Eq. 6.29), which lowers the typical impact speed of saltating particles, thus reducing the number of splashed particles. If, on the other hand, the number of splashed particles is insufficient to balance the settling of saltating particles back to the soil surface, then the particle concentration will decrease. This increases the wind speed and thus the typical impact speed, which in turn increases the number of splashed particles. The model thus iteratively adjusts the particle concentration until steady-state is reached and the particle concentration remains constant with time (i.e., $dn^k/dt = 0$, for all k). In steady-state, we then have that

$$\sum_i \frac{a}{\sqrt{gD}} \frac{D^i_{imp}}{D^k_{ej}} v^i_{imp} f^k = \sum_{j_k} 1 - B\left[1 - \exp\left(-\gamma v^{j_k}_{imp}\right)\right],\qquad(6.32)$$

for all k. As mentioned in Section 1, the stochastic nature of the interaction of saltating particles with the soil surface and with the turbulent wind field means that the model reaches a dynamic balance in which Eq. (6.32) is satisfied over longer time scales (a few seconds; *Anderson and Haff*, 1988, 1991; *Jackson and McCloskey*, 1997). We believe this is an accurate representation of natural saltation.

Since the parameters a, B, and γ in Eqs. (6.31, 6.32) have not been accurately determined by measurements (Table 6.1), a useful constraint on their values is that Eq. (6.32) must be satisfied at the impact threshold. Since the particle concentration (and thus $\tau_p(z)$ in Eq. (6.29)) is small at the impact threshold, the wind profile is simply given by Eq. (6.26), such that particle trajectories are obtained in a straightforward manner. Indeed, for given values of the parameters a, B, and γ, we can calculate the value of the impact threshold at which Eq. (6.32) is satisfied. We find that the functional form of the impact threshold is reproduced almost independently of the values of these parameters, and that $a = 0.020$, $B = 0.96$, and $\gamma = 1.0$ s/m provides good quantitative agreement with measurements of the impact threshold (see Figure 6.6). These parameter values are in agreement with available laboratory and numerical experiments (Table 6.1). To our

knowledge, no previous numerical models of saltation have been able to reproduce measurements of the impact threshold.
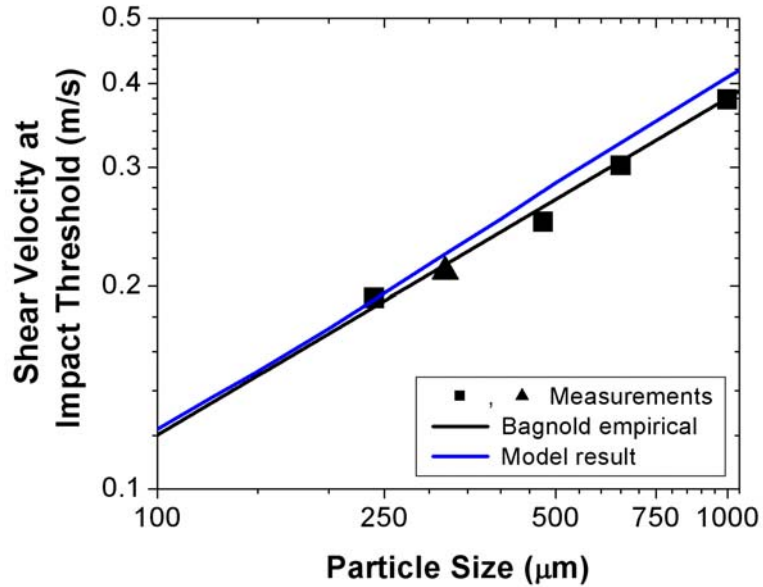
Figure 6.6: Impact threshold for Earth ambient conditions as measured in wind-tunnel experiments by *Bagnold* [1937] (black squares) and *Iversen and Rasmussen* [1994] (black triangle), and predicted by our numerical saltation model (blue line). Also plotted is Bagnold's empirical relation for the impact threshold (black line) [*Bagnold*, 1937, pp. 435].

An additional constraint on the values of *a*, *B*, and *γ* can be obtained by using Eq. (6.32) to determine an approximate average impact speed in steady-state saltation. This can be done by assuming that particle impact speeds are exponentially distributed (see Eq. 6.17), as previous studies have suggested [*Anderson and Hallet*, 1986] and results from our model indicate (not shown). Solving Eq. (6.32) for the average impact speed in this manner yields $\overline{v_{imp}} \approx 1.2$ m/s for 250 μm particles. Note that assuming different plausible impact speed distributions, such as a gamma function [*White and Schulz*, 1977], yields only slightly different values of $\overline{v_{imp}}$. Since the average impact speed is independent of shear velocity [*Ungar and Haff*, 1987], we also expect particle speeds for different shear velocities to converge near the surface. Recent measurements of particle speeds using laser-Doppler anemometry in a wind-tunnel [*Rasmussen and Sorensen*, 2008] have indeed found that particle speeds for different shear velocities converge to a common value of 1.3-1.5 m/s at 4 mm from the surface. This agreement between measurements and the qualitative and quantitative predictions of our model supports the

physical basis underlying our splash parameterization and the chosen values for the
parameters *a, B*, and γ.

Variable (units)	Physical meaning	Relevant literature	Range in literature	Value used in model	Relative uncertainty	Relative sensitivity
$\langle \alpha_{ej} \rangle$	Average fraction of impacting momentum spent on ejecting surface particles	*Rice et al.* [1995]	0.14 – 0.20	$\frac{\langle 1-\sqrt{\varepsilon_{reb}} \rangle}{2.5} \approx 0.15$	Medium	Medium
β	The ratio of the Lagrangian and Eulerian time scales	*Anfossi et al.* [2006]	0.3 – 4	1	High	Low
$\langle \varepsilon_{reb} \rangle$	Average fraction of impacting kinetic energy retained by rebounding particle	*Wang et al.* [2008]	0.43 – 0.46	0.45	Medium	High
γ	Parameter that scales the exponential decay with impact speed of a saltating particle's rebound probability	*Anderson and Haff* [1991]	~2	1	Very high	Low
θ_{ej}	The mean of the exponential distribution that describes the angle from horizontal with which a surface particle is ejected	*Willetts and Rice* [1985, 1986, 1989]; *Anderson and Haff* [1988, 1991]; *McEwan and Willetts* [1991]; *Rice et al.* [1995, 1996]	40 - 60˚	50˚	Low	Low
θ_{reb}	The mean of the exponential distribution that describes the angle from horizontal with which a saltating particle rebounds	*Magnus and Schulz* [1977]; *Willetts and Rice* [1985, 1986, 1989]; *Anderson and Haff* [1988, 1991]; *McEwan and Willetts* [1991]; *Nalpanis et al.* [1993]; *Rice et al.* [1995, 1996]; *Kang et al.,* [2008]	25 – 50˚	40˚	Low	Medium
ρ_a (kg/m³)	Air density – calculated using the ideal gas law with P = 101325 Pa, T = 300 K, and a molar mass of 28.9 grams	N/A	N/A	1.174	N/A	N/A
ρ_p (g/cm³)	Particle density	N/A	N/A	2.65	Very low	Low
$\sigma_{\varepsilon_{reb}}$	Standard deviation of the normal distribution that describes the fraction of kinetic energy that is retained upon rebound	*Wang et al.* [2008]	0.17 – 0.22	0.22	High	Low
σ_{Ω_p} (rev/s)	Standard deviation of the normal distribution that describes the particle spin upon leaving the surface of rebounding or ejected particles	*Chepil and Woodruff* [1963]; *White and Schulz* [1977]; *White* [1982]; *Xie et al.* [2007]; *Zou et al.* [2007]	unclear	500	Very high	Very low
Ω_p (rev/s)	Mean of the normal distribution that describes the particle spin upon leaving the surface of rebounding and ejected particles	*Chepil and Woodruff* [1963]; *White and Schulz* [1977]; *White* [1982]; *Xie et al.* [2007]; *Zou et al.* [2007]	100 – 1000	400	High	Medium
a	Dimensionless constant that scales proportionality between impact speed and number of ejected particles	*McEwan and Willetts* [1991]; *Rice et al.* [1995, 1996]	0.01 – 0.05	0.02	Medium	High
b_u (m/s)	The standard deviation of the turbulent horizontal wind speed	*Shao* [1995]; *Nishimura and Hunt* [2000]	2.4 – 2.5	2.5	Low	Very low
b_w (m/s)	The standard deviation of the turbulent vertical wind speed	*Hunt and Weber* [1979]; *Shao* [1995]; *Nishimura and Hunt* [2000]	1.2 – 1.5	1.4	Low	Low
B (s/m)	Probability that a high-speed particle rebounds upon impacting the soil surface	*Mitha et al.* [1986]; *Anderson and Haff* [1991]	~0.94 – 0.95	0.96	High	Medium

Table 6.1. Description of parameters used in the numerical model, with the range given in the relevant literature, the value used in the model, a subjective indication of the uncertainty in the parameter's value, and the relative sensitivity of the model results to variations in the parameter's value.

6.2.5 Treatment of particles in creep and suspension

As mentioned in the introduction, sediment can be transported by wind in suspension (< 70 μm), saltation (~70 – 500 μm), or creep (> 500 μm) [*Shao*, 2000]. Our model implicitly accounts for creep through the splash parameterization (Section 6.2.2). Indeed, Eq. (6.23) limits the speed with which a massive particle can be ejected from the surface, which in essence describes the process of impacts of smaller particles 'pushing' a larger surface particle in the direction of the wind flow. The good agreement of our model with measurements of the saltation mass flux profile close to the surface (see Section 6.3.1) thus supports the physical basis of our splash parameterization.

We plan to include the emission and transport of suspended dust in a future version of the model.

6.2.6 Discussion of model assumptions

The wind-driven motion of sand particles over a mobile particle bed is a complex process. As also done in previous studies [e.g., *Werner*, 1990; *Anderson and Haff*, 1991; *Shao and Li*, 1999], we focus on the most important physical processes and make several assumptions to keep our numerical model of saltation manageable. Below we list and discuss the most important assumptions made in our model.

1. *Mid-air collisions and electrostatic forces are neglected*. For large shear velocities (i.e., $u^* > ~0.5$ m/s), the particle concentration becomes so large that saltating particles are likely to collide with one or several other particles during a single hop [*Sorensen and McEwan*, 1996; *Dong et al.*, 2005; *Huang et al.*, 2007]. Moreover, electric forces due to sand electrification become large enough to affect particle lifting (Chapter 2) and trajectories (Chapter 3). Since both these processes are less important for small to medium wind shear velocities (i.e., $u^* < ~0.5$ m/s), we do not include these processes in the version of the model described in this chapter. However, work is in progress to include mid-air collisions and sand electrification, following the charging scheme described in Chapter 5, in a future model version [*Kok and Renno*, 2009c].

2. *Steady-state saltation*. When saltation is initiated, the drag of saltating particles on the wind increases the apparent surface roughness [*Owen*, 1964; *McEwan and Willetts*,

1993]. The time scale associated with the adjustment of the near-surface wind to this additional roughness is short – on the order of one second [*Anderson and Haff*, 1988, 1991; *McEwan and Willetts*, 1993; *Jackson and McCloskey*, 1997]. However, the time scale required for the near-surface boundary layer to fully adjust to the flow above the saltation layer is much larger [*McEwan and Willetts*, 1993]. We assume that the flow in the saltation layer is fully adjusted to the flow above the saltation layer, which is not always the case in natural saltation.

3. *Wind speed perpendicular to gravity.* While we define the surface as perpendicular to gravity in the results presented in this chapter, the model is capable of simulating saltation on sloping terrain. We also assume that the wind flow is parallel to the surface. However, a non-zero flow velocity perpendicular to the surface can be included in the model, as done in a previous numerical model by *Yue and Zheng* [2007].

4. *The soil surface is flat.* Sand ripples with typical heights of ~1 cm [*Bagnold*, 1941] usually form during saltation on dunes and beaches. Such ripples will affect the wind flow. However, we follow previous investigators [e.g., *Anderson and Haff*, 1988, 1991; *Shao and Li*, 1999; *Almeida et al.*, 2006] and for simplicity assume that the soil surface is flat.

5. *Particle motion is modeled in two dimensions only.* We assume particle speed to be zero in the direction perpendicular to the plane spanned by the wind and gravitational vectors, while experiments show that ejected and rebounding particles have a small but non-zero speed in this direction [*Xie et al.*, 2007]. Neglecting this component of the particle momentum slightly affects the splash parameterization of Section 6.2.2 [*Zheng et al.*, 2008].

6.3 TESTING OF THE MODEL WITH MEASUREMENTS

We test our model by comparing its results to measurements of the horizontal and vertical profiles of particle mass flux, the total height-integrated mass flux, the size distribution of saltating particles, and the wind profile and aerodynamic roughness length during saltation. When available, we use field measurements rather than wind tunnel measurements since recent studies have shown wind tunnel measurements to differ

significantly and systematically from natural saltation [*Farrell and Sherman*, 2006; *Sherman and Farrell*, 2008].

The values of the parameters used in the model are listed in Table 6.1. We have also included a subjective estimate of the uncertainty of these parameters, as well as a relative indication of the model sensitivity. We hope these estimates can help guide future experimental studies of saltation.

6.3.1 Particle mass flux profiles

Detailed field measurements of the variation of the particle mass flux with height were made by several investigators and are summarized in *Farrell and Sherman* [2006]. Our model shows good agreement with such vertical mass flux profiles as measured by *Greeley et al.* [1996] and *Namikas* [2003] for low ($u* = 0.31$ m/s) and medium ($u* = 0.48$ m/s) shear velocities (Figures 6.7a, 6.7b). For larger shear velocities ($u* = 0.63$ m/s), our model appears to underestimate the decrease in mass flux with height (Figure 6.7c). A possible reason for this is the absence in the present model version of electrostatic forces, which are thought to decrease the height of particle trajectories as the wind speed increases (Chapter 3). Detailed measurements of the horizontal profile of the particle mass flux (i.e., the variation of the particle deposition rate with horizontal distance from a certain starting point) have also been made by *Namikas* [2003]. Simulations with our model show excellent agreement with these measurements (Figure 6.7d-f).

Figure 6.8 compares modeled and measured horizontal and vertical mass flux profiles of particles of various sizes [*Namikas*, 2006]. There is reasonable to good agreement between measurements and the predictions of our model, especially when the many uncertainties that affect the results are considered. The predicted flux of fine particles (< ~200 μm) does however decay somewhat too quickly with vertical and horizontal distances (Figure 6.8a, d). These particles are substantially affected by turbulence [*Anderson*, 1987] and this discrepancy could thus be an indication that the modeled Lagrangian time scale (see Section 6.2.1.2) is too short. Field measurements of this time scale in the saltation layer would thus be a useful addition to the literature.
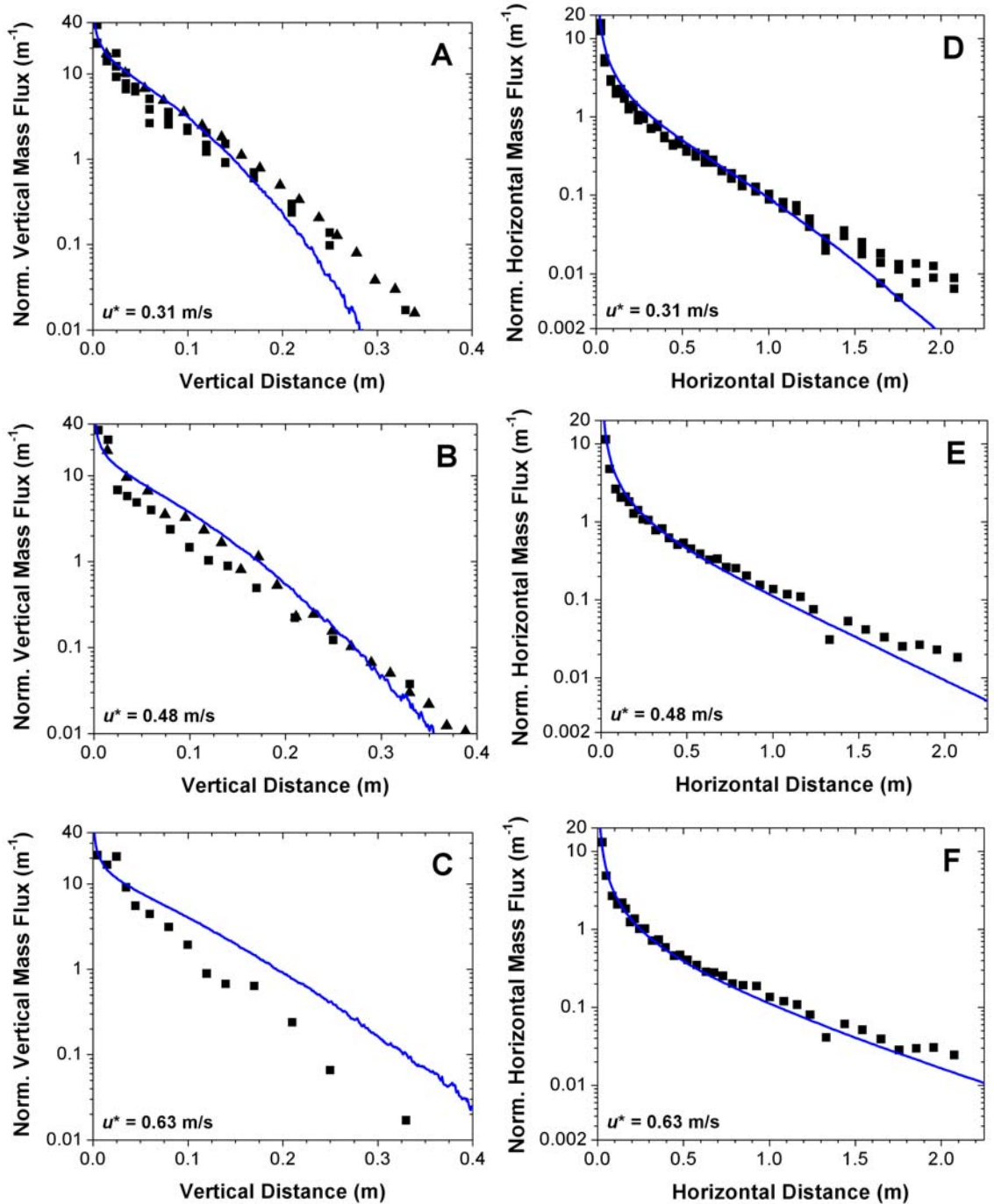
Figure 6.7: Vertical and horizontal mass flux profiles for $u* = 0.31$, 0.48, and 0.63 m/s. Triangles denote vertical mass flux profile measurements from runs 4 and 5b of *Greeley et al.* [1996] and squares denote both vertical and horizontal mass flux profile measurements from runs 4, 5, 8, 13, and 14 of *Namikas* [2003]. Model results (solid blue line) were obtained for the size distribution reported in *Namikas* [2003], which we assume characteristic for *Greeley et al.*'s measurements as well, since their measurements were taken in a similar location. Both measured and modeled mass flux profiles were normalized by their total mass flux to facilitate comparison.
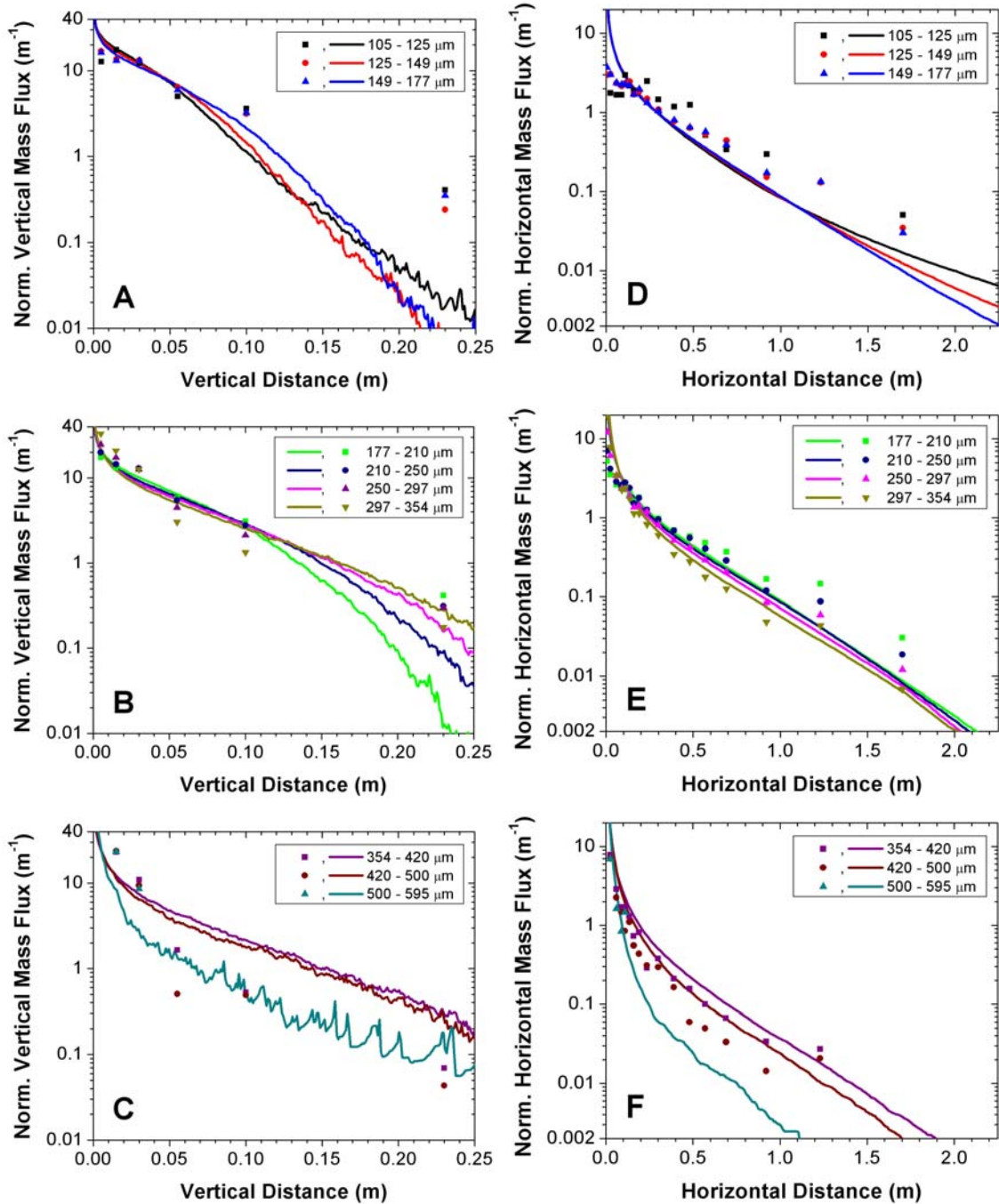
Figure 6.8: Vertical and horizontal mass flux profiles for different particle sizes. The colored symbols represent measurements taken at $u* = 0.36$ m/s by *Namikas* [1999, 2003, 2006], and colored lines denote the model prediction for the corresponding particle size. In order to facilitate comparison, both measured and modeled mass flux profiles are normalized by the total saltation mass flux of a given particle bin. The increased noise at larger heights in the vertical mass flux profiles is due to the low probability of particles to saltate at those heights, which results in a larger uncertainty.

Another possible explanation for this discrepancy could be that smaller particles rebound with a greater fraction of their inbound kinetic energy than larger particles do. Indeed, *Namikas* [2006] recently proposed that particles leave the surface with a kinetic energy that is independent of particle size. A simple model using this assumption shows good agreement with measurements [*Namikas*, 2006]. However, this model requires the speed of small particles leaving the surface to be several times their terminal speed, which would imply that these particles actually gain energy upon rebounding from the surface. This is energetically inconsistent. Moreover, results of a wide range of laboratory experiments have consistently reported that the speed with which particles leave the surface is a constant fraction of the impact speed, and that this fraction is independent of particle size [*Willetts and Rice*, 1985, 1986, 1989; *Rice et al.*, 1995, 1996; *Wang et al.*, 2008] and impact speed [*Rioual et al.*, 2000; *Oger et al.*, 2005; *Beladjine et al.*, 2007]. Nonetheless, a more comprehensive investigation of Namikas' hypothesis is desirable.

6.3.2 Height-integrated mass flux

The total height-integrated mass flux of saltating particles is a key parameter for studies of dune formation [*Sauermann et al.*, 2001], wind erosion [*Sterk*, 2003], and dust aerosol emission [*Marticorena and Bergametti*, 1995]. Many wind-tunnel and field measurements have therefore measured the variation of the total mass flux with shear velocity. These measurements are however difficult to compare directly because of variations in experimental conditions, such as particle size, wind-tunnel characteristics, and air pressure. To nonetheless make a comparison between the large body of experimental studies of saltation mass flux and our model predictions, we non-dimensionalize the total mass flux [*Iversen and Rasmussen*, 1999],

$$Q_0 = \frac{gQ}{\rho_a u*^3},$$
(6.33)

where Q is the total height-integrated saltation mass flux, which is usually assumed to scale with the cube of the shear velocity [*Bagnold*, 1941; *Owen*, 1964; *Iversen and Rasmussen*, 1999].
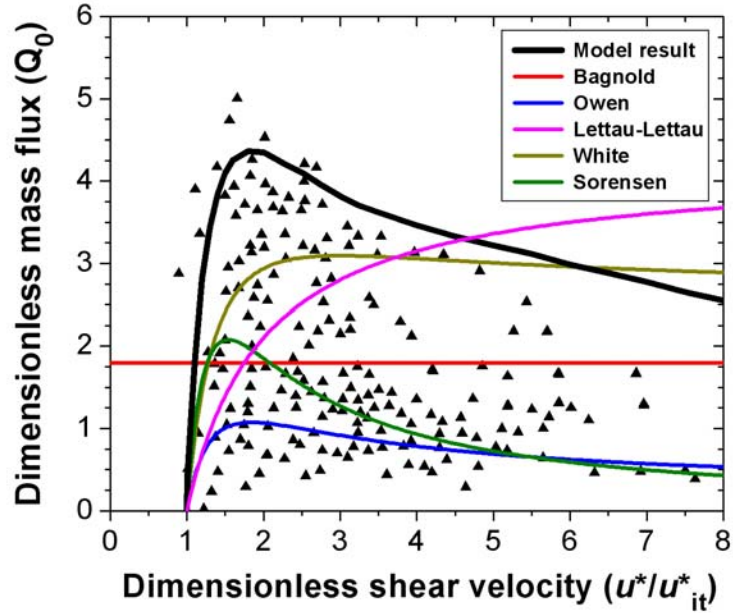
Figure 6.9: Dimensionless saltation mass flux Q_0 (see Eq. 6.33) as a function of dimensionless shear velocity (u^*/u^*_{it}, where u^*_{it} is the impact threshold) simulated with our numerical model (black line), and compared with results from over a dozen wind tunnel studies and one field study compiled by *Iversen and Rasmussen* [1999] (triangles). The large scatter in the experimental results is likely caused by varying experimental conditions, such as particle size, air pressure, and wind-tunnel characteristics [*Iversen and Rasmussen*, 1999]. A peak in the dimensionless mass flux is nonetheless apparent around $u^*/u^*_{it} \approx 2$, and is reproduced by the model. For comparison we also included prominent empirical equations of the saltation mass flux (colored lines) by *Bagnold* [1941] ($Q_0 = 1.8$), *Owen* [1964] ($Q_0 = [0.25 + v_t/3u^*][1 - (u^*_{it}/u^*)^2]$), where v_t is the terminal velocity of saltating particles), *Lettau and Lettau* [1978] ($Q_0 = 4.2[1 - u^*_{it}/u^*]$), *White* [1979] ($Q_0 = 2.61[1 - u^*_{it}/u^*][1 + u^*_{it}/u^*]^2$), and *Sorensen* [1991, 2004] ($Q_0 = [1 - u^{*2}_{it}/u^{*2}][\alpha + \gamma u^*_{it}/u^* + \beta u^{*2}_{it}/u^{*2}]$, with $\alpha = 0$, $\beta = 3.9$, and $\gamma = 3.0$ from Figure 3 in *Sorensen* [2004]). Model results (black line) were obtained for the size distribution of typical beach sand reported in *Namikas* [2003], with an approximate median diameter of 250 μm. For very large shear velocities (i.e., $u^*/u^*_{it} > \sim 4$), a substantial fraction (on the order of $5 - 25$ %) of the predicted mass flux is due to suspended sand transported at large heights. To exclude this fraction from the saltation mass flux, we omit the mass flux transported above a height of 0.5 meters, in accordance with the vertical extent of mass flux collectors used in wind-tunnel [e.g., *Iversen and Rasmussen*, 1999] and field studies [e.g., *Bagnold*, 1938; *Greeley et al.*, 1996; *Namikas*, 2003].

Figure 6.9 compares our model predictions to a compilation of field and wind-tunnel measurements of the dimensionless mass flux [Iversen and Rasmussen, 1999]. Our model reproduces the observed peak of the dimensionless mass flux at $u^*/u^*_{it} \approx 2$ [Iversen and Rasmussen, 1999], where u^*_{it} is the impact threshold, as well as the subsequent decrease for larger shear velocities. Many empirical models are unable to

reproduce these features (see Figure 6.9 and *Iversen and Rasmussen*, 1999). The predicted height-integrated mass flux does appear larger than reported by most experimental studies, which may be because sand collectors used in these studies have an efficiency of only ~50-70 % [*Greeley et al.*, 1996; *Rasmussen and Mikkelsen*, 1998]. Moreover, both mid-air collisions and strong electrostatic forces are hypothesized to decrease the mass flux at large shear velocities [*Sorensen and McEwan*, 1996; *Sorensen*, 2004; Chapter 3]. Since both these processes are not included in the present model version, the overestimation of the mass flux at large shear velocities is thus expected.

6.3.3 Size distribution of saltating particles

Once saltation is initiated, the transfer of momentum to the soil surface by particle impacts causes a wide range of particle sizes to enter saltation. Thus, saltation is not limited to those particles whose threshold shear velocity ($u*_t$) is below the wind shear velocity ($u*$), as is often assumed [e.g., *Marticorena and Bergametti*, 1995]. Rather, the size distribution of saltating particles is determined by two factors: (i) the probability of particles of a given size to be ejected from the surface (see Eq. 6.25), and (ii) the time that particles of a given size spend in saltation before settling back onto the soil surface.

Measurements of the size distribution of saltating particles were reported by *Williams* [1964]. Moreover, we used the size-resolved vertical mass flux profiles reported by *Namikas* [2006] to obtain the saltation size distribution in his field measurements [*Namikas*, 1999, 2003]. The model-predicted saltation size distribution shows good agreement with the measurements of *Williams* [1964] and with those reconstructed from *Namikas* [2006] (Figure 6.10). In general, we find that the size distribution of saltating particles in the range 100 – 500 μm roughly matches the parent soil size distribution (see Section 3.7). This occurs because while larger particles have an increased chance of being ejected from the surface (see Eq. 6.25 and [*Rice et al.*, 1995]), they also tend to have shorter lifetimes. Conversely, smaller particles are ejected less frequently, but have longer lifetimes once ejected. These two effects cause the saltation size distribution to be similar to that of the soil in the range 100 – 500 μm.
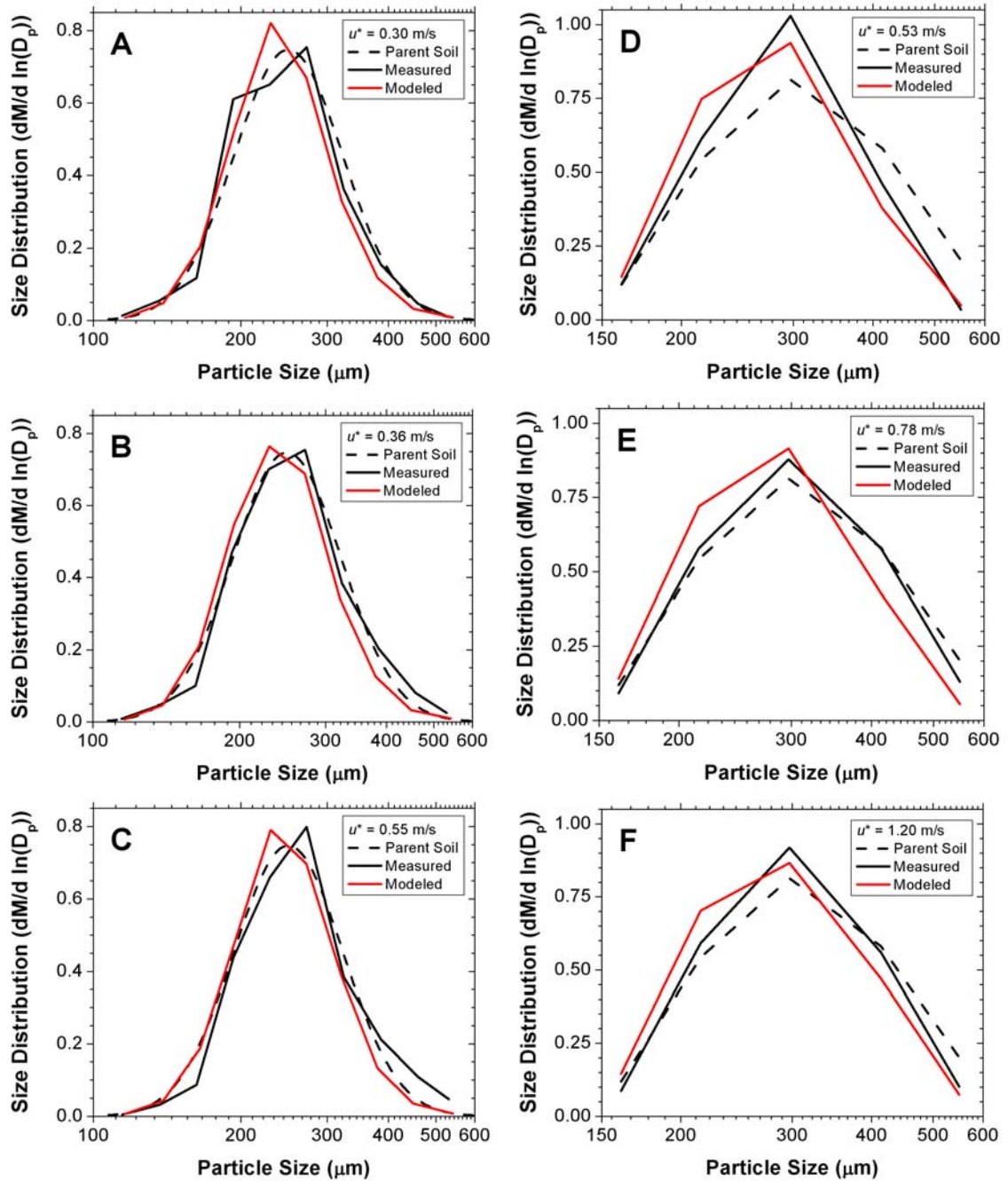
Figure 6.10: Size distributions of saltating particles during saltation, as measured (solid black lines) by *Williams* [1964] (left) and *Namikas* [1999, 2003, 2006] (right) and predicted with our numerical model (red solid lines). Model results were obtained for the same parent soil (dashed black lines) and wind conditions. The saltation size distribution for Namikas' field measurements was obtained by summing the particle size-resolved vertical mass flux reported in Figure 3 of *Namikas* [2006]. We define the size distribution of saltating particles as the contribution of each particle bin to the total height-integrated mass flux, in accordance with measurements [*Williams*, 1964; *Namikas*, 2006].
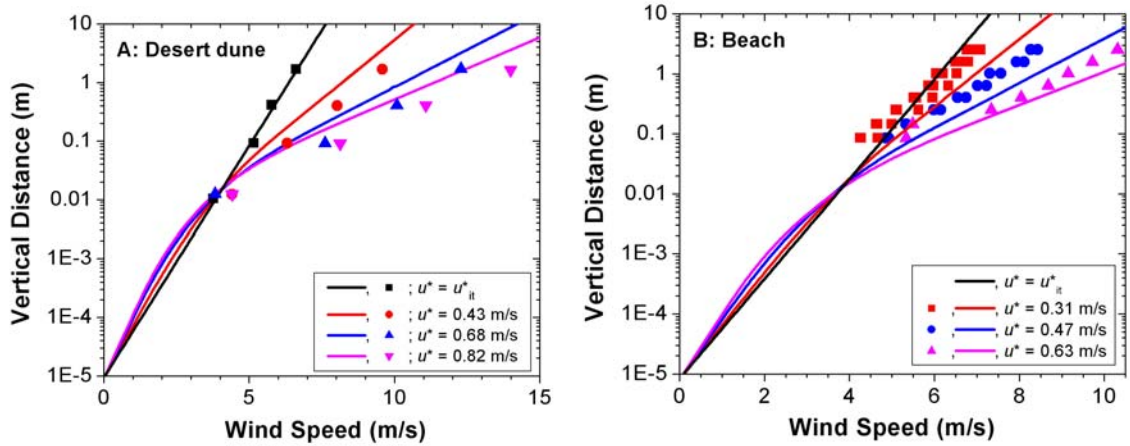
Figure 6.11: Wind profiles during saltation on a desert dune [*Bagnold*, 1938] (symbols in the left graph), on a beach [*Namikas*, 1999] (symbols in the right graph), and modeled (colored lines) for similar conditions. Since *Bagnold* [1938] did not report a soil size distribution, we assume this to be similar to the size distribution of saltating particles (i.e., we used the saltating particle size distribution for u^* = 0.33 m/s reported in Bagnold's Figure 7), as experiments indicate (see Figure 6.9). Using this size distribution, the model predicts an impact threshold (black line) that is in excellent agreement with Bagnold's measured impact threshold (black squares). The model results for *Namikas* [1999] use the size distribution as reported in *Namikas* [2003], for which the model predicts an impact threshold of 0.21 m/s (black line), in good agreement with Namikas' estimated impact threshold of 0.20 – 0.23 m/s [*Namikas*, 1999].

Note that both measurements and our model predictions show that the size distribution shifts slightly towards larger particles as the shear velocity increases. The likely physical reason for this phenomenon is that, while the average impact speed stays approximately constant with increasing shear velocity (see discussion in Section 6.2.4), we find that the probability distribution of impact speeds broadens with shear velocity. As a result, an increasing fraction of impacting particles has very large impact speeds. Since larger surface particles require greater impact speeds to be splashed into saltation, rather than creep along the surface, the number of large particles entering saltation increases with shear velocity. This leads to the observed and predicted slight shift in the saltation size distribution towards larger particle sizes as the shear velocity increases.

6.3.4 The wind speed and roughness length in saltation

Measurements of the wind speed in saltation were made by numerous researchers and are summarized in *Sherman and Farrell* [2008]. Figure 6.11 shows wind speeds predicted by our model and compared to wind speeds measured on a desert dune by *Bagnold* [1938] and on a beach by *Namikas* [1999]. The model is in reasonable

99

agreement in both cases, but underestimates the wind speed in comparison with *Bagnold* [1938], while it overestimates the wind speed in comparison with *Namikas* [1999]. Note that the focusing of the wind profiles (the so-called 'Bagnold focus' [*Bagnold*, 1936]) at a height of ~1 cm is reproduced in both cases.

At a given shear velocity, the wind speed directly above the saltation layer is determined by the increase in the aerodynamic roughness length produced by the transfer of wind momentum to saltating particles [*Owen*, 1964]. Several models have been proposed to relate the aerodynamic roughness length in saltation to the shear velocity [*Charnock*, 1955; *Raupach*, 1991; *Sherman*, 1992]. However, the most physically plausible relationship is probably the modified Charnock relationship [*Sherman*, 1992; *Sherman and Farrell*, 2008]

$$ z_{0S} = z_0 + C_m \frac{\left(u* - u*_{it}\right)^2}{g}, \tag{6.34} $$

where z_{0S} is the aerodynamic roughness length during saltation, and $u*_{it}$ is the impact threshold. *Sherman and Farrell* [2008] used a compilation of 137 wind profiles from field measurements and determined the value of the modified Charnock constant to be $C_m = 0.132 \pm 0.080$. However, for a compilation of 197 wind tunnel experiments, they found that $C_m = 0.0120 \pm 0.0007$. This significant difference in the saltation roughness length between field and wind tunnel experiments indicates that most wind tunnel experiments do not successfully replicate the physics of natural saltation [*Sherman and Farrell*, 2008]. A similar result was obtained by *Farrell and Sherman* [2006], who reported that vertical mass flux profiles in wind tunnel experiments are significantly different from those occurring in natural saltation.

Figure 6.12 compares the model-predicted saltation roughness length with a collection of field measurements compiled by *Sherman and Farrell* [2008]. Our model reproduces the functional form of the modified Charnock model [*Sherman*, 1992] very well, while the agreement with alternative models, such as the Raupach model [*Raupach*, 1991] and the normal Charnock model [*Charnock*, 1955], is not as good (not shown). Moreover, the best-fit value of the modified Charnock constant from our model results is $C_m = 0.125$, which is very close to the value obtained by *Sherman and Farrell* [2008]. Our results are thus in excellent agreement with field measurements of the roughness

length in saltation and provide strong support for the physical correctness of the modified Charnock relationship [*Sherman*, 1992; *Sherman and Farrell*, 2008].
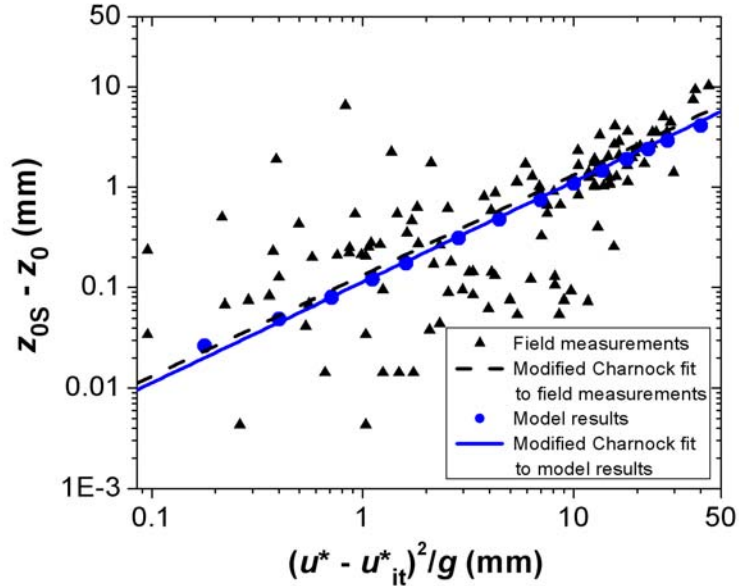
Figure 6.12: Aerodynamic roughness length in saltation from a compilation of field measurements by *Sherman and Farrell* [2008] (black triangles), and simulated by our model (blue circles). Also included are fits with the modified Charnock relationship (Eq. 6.34) [Charnock, 1955; Sherman, 1992] to the compilation of field measurements (black dashed line) and to our model results (blue solid line). The large scatter in the experimental results is probably due to measurement error and variations in experimental conditions, such as particle size, soil moisture content, and surface slope.

6.4 CONCLUSIONS

We have developed a comprehensive numerical model that can simulate steady-state saltation over mixed soils. Our model explicitly simulates particle trajectories due to gravitational and fluid forces and accounts for the effects of turbulence using a parameterization that we show to produce good agreement with measurements (Figure 6.3). We derived a physically-based parameterization of the 'splashing' of surface particles by impacting saltating particles that shows good agreement with available measurements (Figure 6.5), correctly predicts the average impact speed of particles in steady-state saltation (Section 6.2.4) and, when implemented in our numerical saltation model, reproduces measurements of the impact threshold (Figure 6.6).

Our numerical model is the first physically-based model that can reproduce a wide variety of experimental data, including vertical and horizontal profiles of particle mass

flux (Figures 6.7 and 6.8), the total height-integrated mass flux (Figure 6.9), the size distribution of saltating particles (Figure 6.10), and the wind speed in saltation (Figure 6.11). Our model is also the first to reproduce measurements of the aerodynamic roughness length in saltation (Figure 6.12) and reproduces the most physically plausible functional form of the dependence of the roughness length on the shear velocity [*Sherman and Farrell*, 2008].

At large shear velocities, there seems to be less agreement between model predictions and measurements of the vertical profile of the mass flux and the total mass flux (Figures 6.7c and 6.9). This probably occurs because the current model version neglects mid-air collisions and electrostatic forces, which are both thought to become important at large shear velocities [*McEwan and Sorensen*, 1996; Chapter 3]. Work is in progress to include these processes in a future model version [*Kok and Renno*, 2009c].

Since we designed our model to use a minimum of empirical relations, we argue that it is a 'general' model that can be applied, with minimal adaptation, to similar problems in different physical regimes, such as saltating snow, saltation on different planets, and saltation in water. Our model is freely available by contacting the author.

As we outlined in the introduction, a detailed physical understanding of saltation is vital to a variety of problems across scientific disciplines. Of particular interest is the emission of dust aerosols by the impacts of saltating particles on the soil surface [*Shao et al*, 1993; *Marticorena and Bergametti*, 1995; *Shao*, 2000]. These dust aerosols substantially affect the Earth's radiative balance through a variety of processes, and understanding the physical mechanism of their emission is thus essential to understanding past and predicting future climate changes [*Sokolik et al*., 2001; *IPCC*, 2007]. We therefore aim to use our model to develop a physically based parameterization of dust emission for use in climate models.

6.5 ACKNOWLEDGEMENTS

submitted as an article to *Journal of Geophysical Research – Atmospheres* [*Kok and Renno*, 2009b], and is available online at http://arxiv.org/abs/0901.0270 .

CHAPTER 7
CONCLUSIONS AND FUTURE WORK

The objective of this thesis has been to contribute to a comprehensive understanding of saltation. As outlined in Chapter 1, specific contributions towards this central objective were made through three distinct but related investigations: the analysis of the effect of electric forces on saltation and dust lifting (Chapters 2, 3, and 4), the development of a quantitative theoretical model of the electrification of wind-blown sand and other granular systems of chemically identical insulators (Chapter 5), and the development of a comprehensive numerical model of saltation that can be used to study a wide variety of natural processes driven by saltation (Chapter 6). Below, I briefly summarize the contributions of this thesis to by three distinct investigations.

7.1 THE EFFECT OF SAND ELECTRIFICATION ON SALTATION AND DUST LIFTING

The analysis of the role of sand electrification on saltation and dust lifting was described in Chapters 2, 3, and 4. In Chapter 2, I used laboratory experiments to show that E-fields in excess of ~80 kV/m reduce the wind stress required to lift surface particles by over 10 % (Figure 2.6) and that E-fields larger than ~150-175 kV/m can even directly lift surface particles (Figures 2.4 and 2.5). These effects are potentially important, since E-fields measured in saltation, dust storms, and dust devils range between 1-200 kV/m (see Section 1.2.1).

In Chapter 3, I used these laboratory findings to develop a numerical model of saltation (see Section 3.7), and used it to study the effects of sand electrification on saltation. I found that sand electrification approximately doubles the particle concentration at large wind speeds (Figure 3.4). Moreover, I found that sand electrification lowers the trajectories of saltating particles, because they are attracted to the oppositely charged soil surface. This finding seems to resolve the discrepancy

between classical theory, which predicts that the saltation layer height increases sharply with wind speed, and measurements, which show that the saltation layer height is approximately constant with wind speed (Figure 3.5).

In Chapter 4, I applied the numerical model of saltation described in Chapter 3 to Mars, and expanded it by including plasma physics to account for the ionization of CO_2 by large E-fields. I found that this ionization substantially reduces the time scale with which charges on saltating particles decay, thereby limiting the build-up of E-fields to ~15 – 20 kV/m (Figure 4.1). Since electric discharges in the saltation layer require an E-field of over 40 kV/m (Eq. 4.1), such discharges are thus unlikely to occur. Moreover, the results indicate that the production of hydrogen peroxide and the dissociation of methane by E-fields in saltation, dust storms, and dust devils are less significant than previously thought because, for a given E-field, the concentration of energetic electrons that produce these important chemical effects is lower than previously suggested (Figure 4.2). The occurrence on Mars of both methane and hydrogen peroxide are highly relevant to studies of past and present life there.

7.2 UNDERSTANDING THE PHYSICAL PROCESSES UNDERLYING THE ELECTRIFICATION OF GRANULAR SYSTEMS OF IDENTICAL INSULATORS

While the above results have provided more insight into the effects of sand electrification on saltation, they have not determined why sand and dust become electrified in the first place. The widely observed dependence of this charging on particle size is especially puzzling, because the particles are macroscopic and chemically identical; therefore, there is no contact potential difference between particles of different sizes. In Chapter 5, I presented a theoretical model of the triboelectrification of granular systems of chemically identical insulators, based on the existence of trapped high-energy electrons on the surface of insulators [*Lowell and Truscott*, 1986b]. I showed that the size-dependent charging of chemically identical particles is at least partially due to (i), simple geometric considerations which cause more electrons to tunnel from the larger particle to the smaller particle than vice versa (Eq. 5.9), and (ii), the fact that smaller particles will lose a larger fraction of high-energy electrons during initial collisions, such

that during subsequent collisions they will give up fewer trapped electrons than larger particles do [*Lacks et al.*, 2008]. Both these effects cause smaller particles to charge negatively and larger particles to charge positively, in agreement with experimental observations [*Schmidt et al.*, 1998, 1999; *Miura et al.*, 2002; *Zheng et al.*, 2003; *Inculet et al.*, 2006; *Forward et al.*, 2009a]. I implemented both these charging mechanisms into a quantitative scheme that, based purely on theoretical considerations, is both qualitatively and quantitatively consistent with measurements (Figures 5.2 and 5.4). It thus appears that the theoretical model presented in Chapter 5 provides an explanation for the hitherto mysterious size-dependent electrification of granular systems of identical insulators, such as wind-blown sand.

7.3 THE DEVELOPMENT OF A COMPREHENSIVE NUMERICAL MODEL OF SALTATION

In addition to investigations into the effect of electric forces on saltation and dust lifting and the development of a quantitative theoretical model that helps explains the occurrence of sand electrification, I also developed a comprehensive numerical model of steady-state saltation in Chapter 6. This comprehensive model is a substantial improvement over the simpler numerical model developed in Chapter 3, because it replaces many of the empirical relationships used in the latter model with physically-based relationships. As such, the comprehensive numerical model described in Chapter 6 is intended for application to natural saltation and thus, in contrast to most previous studies, can simulate saltation over mixed soils. The model simulates the motion of saltating particles due to gravity, fluid drag, particle spin, fluid shear, and turbulence, and explicitly accounts for the retardation of the wind due to drag from saltating particles. It also includes a physically-based parameterization of the ejection of surface particles by impacting saltating particles which matches experimental results (Figure 6.5). The model is the first to reproduce measurements of the wind shear velocity at the impact threshold (i.e., the lowest shear velocity for which saltation is possible; see Figure 6.6) and of the aerodynamic roughness length in saltation (Figure 6.12). It also correctly predicts a wide range of other saltation processes, including profiles of the wind speed and particle mass flux (Figures 6.7, 6.8, and 6.11), the total height-integrated mass flux (Figure 6.9), and

the size distribution of saltating particles (Figure 6.10). Indeed, this model is the first to reproduce such a wide range of experimental data. Since the model is formulated using a minimum of empirical relations, it can be easily adapted to study saltation under a variety of physical conditions, such as saltation on other planets, saltation under water, and saltating snow.

7.4 FUTURE WORK

The research described in this dissertation suggests several avenues for future studies that would further improve the understanding of dust lifting, saltation, and the effects of sand electrification. Below, I list particularly promising directions for future investigations.

1. The understanding of the physical processes that cause sand electrification (Chapter 5) should be integrated into our comprehensive numerical model of saltation (Chapter 6), which currently neglects the effects of sand electrification (see Section 6.2.6). Work in this direction is already under way [*Kok and Renno*, 2009c], and is likely to lead to an improved understanding of both the effects of sand electrification on saltation and the physical reason that causes the height of the saltation layer to remain constant with wind speed (Figure 3.5).

2. To further improve our understanding of the effects of sand electrification, additional measurements of particle charge and *E*-fields in saltation are critical. Currently, only one study of *E*-fields in natural saltation is available [*Schmidt et al.*, 1998], and more such studies are thus required. The miniature electric field sensor that our research group developed [*Renno et al.*, 2008] would be ideally suited to make these measurements.

3. The comprehensive numerical model of saltation described in Chapter 6 was developed partially to improve the understanding of the emission of dust aerosols, which greatly influence climate and climate change (Chapter 1). Applying the model to dust emission is thus a logical and important next step. In particular, the model should be used to aid the development of a physically-based relationship between the wind shear velocity and the saltation mass flux [*Kok and Renno*, 2007]. Moreover, the model should be used to better understand the physical

parameters that determine the energy with which saltating particles impact the soil, since the subsequent ejection of dust aerosols from the soil is proportional to this impacting energy [*Shao and Raupach*, 1993]. Note that the saltators' energy is strongly dependent on the particle speed, and thus the height of the saltation layer (see Figure 3.5). Developing a more rigorous theory of saltation (possibly including the effects of electric forces), which correctly predicts the height of the saltation layer is thus critical to forecasting dust aerosol emissions as a function of wind speed and soil characteristics.

4. The comprehensive numerical model of saltation developed in Chapter 6 should also be applied to Mars. Aeolian processes on that planet are of immense importance and both shape the landscape and affect the climate [*Greeley and Iversen*, 1985; *Fenton et al.*, 2007]. While there has been recent progress in developing numerical models of Martian saltation [*Almeida et al.*, 2008], these models have not been rigorously shown to reproduce measurements of natural saltation on Earth, and their validity on Mars is thus uncertain. Preliminary results of the numerical model developed in Chapter 6 when applied to martian conditions indicate that the impact threshold on Mars is substantially smaller than previously thought, which implies that martian saltation has a large hysteresis effect. That is, once saltation is initiated, it can be sustained at substantially lower wind speeds [*Claudin and Andreotti*, 2006; *Almeida et al.*, 2008]. Moreover, the trajectories of saltating particles seem to be substantially lower than previously suggested. The difference probably occurs because previous studies did not explicitly account for the ejection of surface particles by the impact of saltating particles.

APPENDIX:
LIST OF PUBLICATIONS GENERATED BY THESIS

Kok, J. F., and D. J. Lacks, The triboelectrification of granular systems of identical insulators, *Phys. Rev. E*, in review, available online at arxiv.org/abs/0902.3411

Kok, J. F., and N. O. Renno (2006), Enhancement of the emission of mineral dust aerosols by electric forces, *Geophys. Res. Lett.*, 33, L19S10.

Kok, J. F., and N. O. Renno (2008), The effects of electric forces on dust lifting: Preliminary studies with a numerical model, *J. Phys. Conf. Ser.,* 142, 012047.

Kok, J. F., and N. O. Renno (2008), Electrostatics in wind-blown sand, *Phys. Rev. Lett.,* 100, 014501.

Kok, J. F., and N. O. Renno (2009), Electrification of wind-blown sand on Mars and its implications for atmospheric chemistry, *Geophys. Res. Lett.,* 36, L05202.

Kok, J. F., and N. O. Renno, A comprehensive numerical model of wind-blown sand, *J. Geophys. Res.*, in review, available online at arxiv.org/abs/0901.0270 .

Rasmussen, K. R., J. F. Kok, and J. P. Merrison (2009), Enhancement in wind driven sand transport by electric fields, *Planet. Space Sci.*, published online, http://dx.doi.org/10.1016/j.pss.2009.03.001

Renno, N. O., and J. F. Kok, (2008), Electrical activity and dust lifting on Earth, Mars, and beyond, *Space Sci. Rev.*, 137(1-4), 419-434.

Renno, N. O., J. F. Kok, H. Kirkham, and S. Rogacki (2008), A miniature sensor for electrical field measurements in dusty planetary atmospheres, *J. Phys. Conf. Ser.,* 142, 012075.

Ruf, C., N. O. Renno, J. F. Kok, E. Bandelier, M. J. Sanders, S. Gross, L. Skjerve, B. Cantor, The emission of non-thermal radiation by a Martian dust storm, *Geophys. Res. Lett.*, in review.

BIBLIOGRAPHY

Aitken, M. J.,, in *Chrometric Dating in Archaeology*, edited by Taylor and Aitken (Plenum Press, New York, 1997).

Almeida, M. P., et al. (2006), Aeolian transport layer, *Physical Review Letters*, *96*(1), 018001.

Almeida, M. P., et al. (2008), Giant saltation on Mars, *Proceedings of the National Academy of Sciences of the United States of America*, *105*(17), 6222-6226.

Anderson, R. S., and B. Hallet (1986), Sediment transport by wind – toward a general model, *Geological Society of America Bulletin*, *97*(5), 523-535.

Anderson, R. S. (1987), Eolian sediment transport as a stochastic process – the effects of a fluctuating wind on particle trajectories, *Journal of Geology*, *95*(4), 497-512.

Anderson, R. S., and P. K. Haff (1988), Simulation of eolian saltation, *Science*, *241*(4867), 820-823.

Anderson, R. S., and P. K. Haff (1991), Wind modification and bed response during saltation of sand in air, *Acta Mech. Suppl. 1*, 21-51.

Anfossi, D., et al. (2006), Estimation of the ratio between the Lagranglan and Eulerian time scales in an atmospheric boundary layer generated by large eddy simulation, *Atmospheric Environment*, *40*(2), 326-337.

Atreya, S. K., et al. (2006), Oxidant enhancement in Martian dust devils and storms: Implications for life and habitability, *Astrobiology*, 6, 439– 450.

Bagnold, R. A. (1935), The movement of desert sand, *Geogr. J.*, *85*(4), 342-365.

Bagnold, R. A. (1936), The movement of desert sand, *Proceedings of the Royal Society of London Series a-Mathematical and Physical Sciences*, *157*(A892), 0594-0620.

Bagnold, R. A. (1937), The transport of sand by wind, *The Geographical Journal*, *89*(5), 409-438

Bagnold, R. A. (1938), The measurement of sand storms, *Proceedings of the Royal Society of London Series a-Mathematical and Physical Sciences*, *167*(A929), 0282-0291.

Bagnold, R. A. (1941), *The physics of blown sand and desert dunes*, Methuen, New York.

Bagnold, R. A. (1973), Nature of saltation and bed-load transport in water, *Proceedings of the Royal Society of London Series a-Mathematical Physical and Engineering Sciences*, *332*(1591), 473-504.

Beladjine, D., et al. (2007), Collision process between an incident bead and a three-dimensional granular packing, *Physical Review E*, *75*(6), 061305.

Cakmur, R.V., R. L. Miller, and O. Torres (2004), Incorporating the effect of small-scale circulations upon dust emission in an atmospheric general circulation model, *J. Geophys. Res.*, *109*(D7)*,* D07201, doi:10.1029/2003JD004067.

Camenen, B. (2007), Simple and general formula for the settling velocity of particles, *Journal of Hydraulic Engineering-Asce*, *133*(2), 229-233.

Castle, G. S. P. (1997), Contact charging between insulators, *J. Electrost.*, *40-1*, 13-20.

Castle, G. S. P., and L. B. Schein (1995), General model of sphere sphere insulator contact electrification, *J. Electrost.*, *36*(2), 165-173.

Charnock, H. (1955), Wind stress on a water surface, *Q. J. R. Meteorol. Soc.*, 81, 639–640.

Cheng, N. S. (1997), Simplified settling velocity formula for sediment particle, *Journal of Hydraulic Engineering-Asce*, *123*(2), 149-152.

Chepil, W. S. (1958), The use of evenly spaced hemispheres to evaluate aerodynamic forces on a soil surface, *Trans. Am. Geophys. Un., 39*, 397-403.

Chepil, W. S. (1963), The physics of wind erosion and its control, *Adv. Agron.*, 15, 3–11.

Claudin, P., and B. Andreotti (2006), A scaling law for aeolian dunes on Mars, Venus, Earth, and for subaqueous ripples, *Earth Planet. Sc. Lett., 252*(1-2), 30-44, doi:10.1016/j.epsl.2006.09.004.

Corn, M. (1961), Adhesion of solid particles to solid surfaces, I, A review, *J. Air Pollut. Control Assoc.*, *11*, 523-528.

Crozier, W.D. (1964), Electric field of New Mexico dust devil, *J. Geophys. Res.*, 69(24), 5427-&.

Crozier, W.D. (1970), Dust devil properties, *J. Geophys. Res.*, 75(24), 4583-&.

Csanady, G. T. (1963), Turbulent diffusion of heavy particles in the atmosphere, *Journal of the Atmospheric Sciences*, *20*(3), 201-208.

Delory, G., et al. (2006), Oxidant enhancement in martian dust devils and storms: Storm electric fields and electron dissociative attachment, *Astrobiology, 6*(3), 451-462.

Demon, L., DeFelice, P., Gondet, H., Kast, Y., Pontier, L.,1953. Premiers résultats obtenus au cours du printemps 1953, *J. Rech. Cent. Natl Rech. Sci.*, 24, 126–137.

DeMott, P. J., et al. (2003), African dust aerosols as atmospheric ice nuclei, *Geophysical Research Letters*, *30*(14), 1732.

Desch, S. J., and J. N. Cuzzi (2000), The generation of lightning in the solar nebula, *Icarus*, *143*, 87-105.

Dietrich, W. E. (1982), Settling velocity of natural particles, *Water Resources Research*, *18*(6), 1615-1626.

Dong, Z. B., et al. (2005), Simulation of the probability of midair interparticle collisions in an aeolian saltating cloud, *Journal of Geophysical Research-Atmospheres*, *110*(D24), D24113.

Draine , B. T., and B. Sutin (1987), Collisional charging of interstellar grains, *Astrophys. J.*, *320* (2), 803-817.

Duff, N., and D. J. Lacks (2008), Particle dynamics simulations of triboelectric charging in granular insulator systems, *J. Electrost.*, *66*(1-2), 51-57.

Duke, C. B. (1978), Polymers and molecular solids – new frontiers in surface science, *Surf. Sci.*, *70*(1), 674-691.

Eden, H., and B. Vonnegut (1973), Electrical breakdown caused by dust motion in low-pressure atmospheres - considerations for Mars, *Science, 180*(4089), 962-963.

Farrell, W., G. Delory, S. Cummer, and J. Marshall (2003), A simple electrodynamic model of a dust devil, *Geophys. Res. Lett., 30*(20), 2050, doi:10.1029/2003GL017606.

Farrell, W.M., et al. (2004), Electric and magnetic signatures of dust devils from the 2000-2001 MATADOR desert tests, *J. Geophys. Res.-Planets*, *109*(E3), E03004.

Farrell, W. M., G. T. Delory, and S. K. Atreya (2006), Martian dust storms as a possible sink of atmospheric methane, *Geophys. Res. Lett., 33* (21), L21203, doi:10.1029/2006GL027210.

Farrell, E. J., and D. J. Sherman (2006), Process-scaling issues for aeolian transport modelling in field and wind tunnel experiments: Roughness length and mass flux

distributions, *Journal of Coastal Research*, *1*, 384-389.

Fenton, L. K., et al. (2007), Global warming and climate forcing by recent albedo changes on Mars, *Nature*, *446*(7136), 646-649.

Formisano, V., S. Atreya, T. Encrenaz, N. Ignatiev, and M. Giuranna (2004), Detection of methane in the atmosphere of Mars, *Science, 306* (5702), 1758-1761, doi: 10.1126/science.1101732.

Forward, K. M., D. J. Lacks, and R. M. Sankaran (2009a), Charge Segregation Depends on Particle Size in Triboelectrically Charged Granular Materials, *Phys. Rev. Lett.*, *102*(2), 028001.

Forward, K. M., D. J. Lacks, and R. M. Sankaran (2009b), Triboelectric charging of granular insulator mixtures due solely to particle-particle interactions, Ind. Eng. Chem. Res., DOI: 10.1021/ie8004786, in press.

Freier, G. D. (1960), The electric field of a large dust devil. *J. Geophys. Res.*, *65*, 3504.

Fridman, A. A., and L. A. Kennedy (2004), *Plasma Physics and Engineering*, Taylor & Francis, New York.

Fuerstenau, S., and G. Wilson (2004), A particle charge spectrometer for determining the charge and size of individual dust grains on Mars, *Electrostatics 2003*, **178**, 143.

Gillette, D.A., I. H. Blifford, and D. W. Fryrear (1974), The influence of wind velocity on the size distribution of aerosols generated by the wind erosion of soils, *J. Geophys. Res., 79*, 4068-4075.

Gillette, D. A., J. Adams, A. Endo, D. Smith, and R. Kihl (1980), Threshold velocities for input of soil particles into the air by desert soils, *J. Geophys. Res.*, *85*(NC10), 5621-5630.

Gillette, D. A., and W. Chen (1999), Size distributions of saltating grains: An important variable in the production of suspended particles, *Earth Surf. Proc. Landforms.*, *24*(5), 449-462.

Gillette, D. A., B. Marticorena, and G. Bergametti (1998), Change in the aerodynamic roughness height by saltating grains: Experimental assessment, test of theory, and operational parameterization, *J. Geophys. Res.*, *103*(D6), 6203-6209.

Gillette, D. A., and T. R. Walker (1977), Characteristics of airborne particles produced by wind erosion of sandy soil, high plains of west Texas, *Soil Science*, *123*(2), 97-110.

Goudie, A.S., and N.J. Middleton (2006), *Desert dust in the global system*, Springer, Berlin.

Greeley, R., and J. D. Iversen (1985), *Wind as a Geological Process on Earth, Mars, Venus, and Titan*, Cambridge University Press, New York.

Greeley, R., et al. (1996), Field measurements of the flux and speed of wind-blown sand, *Sedimentology*, *43*(1), 41-52.

Gurevich A. V., G. M. Milikh, and R. Rousseldupre (1992), Runaway electron mechanism of air breakdown and preconditioning during a thunderstorm, *Phys. Lett. A*, 165 (5-6), 463-468.

Haff, P. K., and R. S. Anderson (1993), Grain scale simulations of loose sedimentary beds – the example of grain-bed impacts in aeolian saltation, *Sedimentology*, *40*(2), 175-198.

Hairer, E, S. P. Nørsett, and G. Wanner (1993), *Solving ordinary differential equations I: Nonstiff problems* (2nd ed.), Springer Verlag, Berlin.

Harper, W.R., *Contact and Frictional Dissipation*, Clarendon Press, Oxford (1967)

Henry, P.S.H. (1953), Survey of generation and dissipation of static electricity, *Br. J. Appl. Phys.* **4**(Suppl. 2), S6.

Houghton, J. T., Y. Ding, D. J. Griggs, M. Noguer, P. van der Linden, X. Dai, and K. Maskell (Eds.) (2001), *Climate Change 2001: The Scientific Basis—Contributions of Working Group I to the Third Assessment Report of the Intergovernmental Panel on Climate Change*, Cambridge Univ. Press, New York.

Huang, N., et al. (2007), A model of the trajectories and midair collision probabilities of sand particles in a steady state saltation cloud, *Journal of Geophysical Research-Atmospheres*, *112*(D8), D08206.

Hunt, J.C.R., and P. Nalpanis (1985), Saltating and suspended particles over flat and sloping surfaces. I. Modelling concepts, *Proc. Int. Workshop Physics of Blown Sand*, *1*, 9-36.

Hunt, J. C. R., and A. H. Weber (1979), Lagrangian statistical analysis of diffusion from a ground-level source in a turbulent boundary-layer, *Quarterly Journal of the Royal Meteorological Society*, *105*(444), 423-443.

Inculet, I. I., G. S. P. Castle, and G. Aartsen (2006), Generation of bipolar electric fields during industrial handling of powders, *Chem. Eng. Sci.*, *61*(7), 2249-2253.

IPCC (2007): *Climate Change 2007: The Physical Science Basis. Contribution of Working Group I to the Fourth Assessment Report of the Intergovernmental Panel on Climate Change* [Solomon, S., D. Qin, M. Manning, Z. Chen, M. Marquis, K.B. Averyt, M.Tignor and H.L. Miller (eds.)]. Cambridge University Press, Cambridge,

United Kingdom and New York, NY, USA.

Iversen, J. D., and K. R. Rasmussen (1994), The effect of surface slope on saltation threshold, *Sedimentology*, *41*(4), 721-728.

Iversen, J. D., and K. R. Rasmussen (1999), The effect of wind speed and bed slope on sand transport, *Sedimentology*, *46*(4), 723-731.

Jackson, D. W. T., and J. McCloskey (1997), Preliminary results from a field investigation of aeolian sand transport using high resolution wind and transport measurements, *Geophysical Research Letters*, *24*(2), 163-166.

Jackson J.D. (1999), *Classical Electrodynamics*, 3rd ed., Wiley, New York.

Jackson, T.L., Farrell, W.M., 2006. Electrostatic fields in dust devils: an analog to Mars, *IEEE Trans. Geosci. Remote Sens.*, 44, 2942–2949.

Jackson, T. L., W. M. Farrell, G. T. Delory, and J. Nithianandam (2008), Effect of dust absorption on the electron avalanche process occurring within Martian dust storms, *Geophys. Res. Lett.*, 35 (16), L16201, doi:10.1029/2008GL034523.

Jauregui, E. (1989), Meteorological and environmental aspects of dust storms in northern Mexico, *Erdkunde*, *43*, 141-147.

Jickells, T. D., et al. (2005), Global iron connections between desert dust, ocean biogeochemistry, and climate, *Science*, *308*(5718), 67-71.

Kamra, A.K. (1972), Measurements of electrical properties of dust storms, *J. Geophys. Res.*, 77(30), 5856-&.

Kanagy, S. P., and C. J. Mann (1994), Electrical properties of eolian sand and silt. Earth Sci. Rev., 36, 181-204.

Kang, L. Q., et al. (2008), Reconstructing the vertical distribution of the aeolian saltation mass flux based on the probability distribution of lift-off velocity, *Geomorphology*, *96*(1-2), 1-15.

Keith, B.A., 1944. A suggested classification of Great Plains dust storms. *Trans. Kans. Acad. Sci.*, 47, 95–109.

Kok, J. F., and D. J. Lacks (2009), The triboelectrification of granular systems of identical insulators, *Phys. Rev. E*, in review, available online at http://arxiv.org/abs/0902.3411 .

Kok, J. F., and N. O. Renno (2006), Enhancement of the emission of mineral dust aerosols by electric forces, *Geophys. Res. Lett.*, *33*(19), L19S10.

Kok, J.F., and N.O. Renno (2007), Physically based numerical model of wind-blown sand suggests deficiencies in classical saltation theory, *Eos Trans. AGU*, Fall Meet. Suppl., Abstract NG43A-01.

Kok, J. F., and N. O. Renno (2008), Electrostatics in wind-blown sand, *Phys Rev. Lett.*, *100*(1), 014501.

Kok, J. F., and N. O. Renno (2009a), The electrification of wind-blown sand on Mars and its implications for atmospheric chemistry, *Geophys. Res. Lett.*, 36, L05202.

Kok, J. F., and N. O. Renno (2009b), A comprehensive numerical model of wind-blown sand, *J. Geophys. Res.*, in review, available online at http://arxiv.org/abs/0901.0270 .

Kok, J. F., and N. O. Renno (2009c), A detailed numerical investigation into wind-blown sand, in preparation.

Krauss, C. E., et al. (2003), Experimental evidence for electrostatic discharging of dust near the surface of Mars, *New J. Phys.*, *5*, 9.

Kron, A., et al. (1997), Luminescence from gamma- and beta-irradiated HDPE and LLDPE, *Polym. Int.*, *42*(2), 131-137.

Lacks, D. J., et al. (2008), Nonequilibrium accumulation of surface species and triboelectric charging in single component particulate systems, *Phys. Rev. Lett.*, *100*(18).

Lacks, D. J., and A. Levandovsky (2007), Effect of particle size distribution on the polarity of triboelectric charging in granular insulator systems, *J. Electrostat.* 65(2), 107-112.

Lancaster, N. (1986), Grain-size characteristics of linear dunes in the Southwestern Kalahari, *J. Sediment. Petrol.*, *56*(3), 395-400.

Lebedev, N. N., and I. P. Skalskaya (1962), Force Acting on a Conducting Sphere in Field of a Parallel Plate Condenser, *Soviet Physics-Technical Physics*, *7*, 268.

Lettau, K., and H. H. Lettau (1978), Experimental and micro-meteorological field studies of dune migration. In: Exploring the World's Driest Climate (Ed. by H.H. Lettau and K. Lettau), IES Report, *101*, 110-147. University of Wisconsin-Madison, Institute for Environmental Studies.

Leuning, R., et al. (2000), Source/sink distributions of heat, water vapour, carbon dioxide and methane in a rice canopy estimated using Lagrangian dispersion analysis, *Agricultural and Forest Meteorology*, *104*(3), 233-249.

Li, Z. S., J. R. Ni, and C. Mendoza (2004), An analytic expression for wind-velocity profile within the saltation layer, *Geomorphology*, *60*(3-4), 359-369.

Loth, E. (2008), Lift of a solid spherical particle subject to vorticity and/or spin, *Aiaa Journal*, *46*(4), 801-809. Lowell, J. (1979), Tunnelling between metals and insulators and its role in contact electrification, *J. Phys. D Appl. Phys.*, *12*(9), 1541-1554.

Lowell, J. (1986), Constraints on contact charging of insulators. 1. Spatial localization of insulator states, *J. Phys. D Appl. Phys.*, *19*(1), 95-104.

Lowell, J., and A. C. Rose-Innes (1980), Contact electrification, *Adv. Phys.*, *29*(6), 947-1023.

Lowell, J., and W. S. Truscott (1986a), Triboelectrification of identical insulators. 1. An experimental investigation, *J. Phys. D Appl. Phys.*, *19*(7), 1273-1280.

Lowell, J., and W. S. Truscott (1986b), Triboelectrification of identical insulators: II. Theory and further experiments, *J. Phys. D: Appl. Phys., 19*, 1281-1298.

Marticorena, B., and G. Bergametti (1995), Modeling the atmospheric dust cycle. 1. Design of a soil-derived dust emission scheme, *Journal of Geophysical Research-Atmospheres*, *100*(D8), 16415-16430.

McEwan, I. K., and B. B. Willetts (1991), Numerical model of the saltation cloud, *Acta Mech. Suppl. 1*, 53-66.

McEwan, I. K., and B. B. Willetts (1993), Adaptation of the near-surface wind to the development of sand transport, *Journal of Fluid Mechanics*, *252*, 99-115.

McLaughlin, J. B. (1991), Inertial migration of a small sphere in linear shear flows, *Journal of Fluid Mechanics*, *224*, 261-274.

Melnik, O., and M. Parrot (1998), Electrostatic discharge in Martian dust storms, *J. Geophys. Res., 103* (A12), 29,107-29,117.

Michael, M., et al. (2008), Dust charging and electrical conductivity in the day and nighttime atmosphere of Mars, *J. Geophys. Res.*, *113*(E7), E07010.

Mitha, S., et al. (1986), The grain-bed impact process in aeolian saltation, *Acta Mechanica*, *63*(1-4), 267-278.

Miura, T., et al. (2002), Measurements of electric charge distribution in volcanic plumes at Sakurajima Volcano, Japan, *B. Volcanol.*, *64*(2), 75-93.

Molina-Cuberos, G.J.., et al. (2001), A model for the Martian ionosphere below 70 km, *Adv. Space Res., 27* (11), 1801-1806.

Molina-Cuberos, G.J.., et al. (2002), Ion-neutral chemistry model of the lower ionosphere of Mars, *J. Geophys. Res., 107* (E5), 5027, doi:10.1029/2000JE001447.

Morsi, S. A., and A. J. Alexander (1972), Investigation of particle trajectories in 2-phase flow systems, *J. Fluid Mech.*, *55*, 193.

Myhre, G., and F. Stordal (2001), Global sensitivity experiments of the radiative forcing due to mineral aerosols, *J. Geophys. Res.*, *106*, 18,193–18,204.

Murtomaa, M., et al. (2003), Electrostatic measurements on a miniaturized fluidized bed, *J. Electrost.*, *57*(1), 91-106.

Nalpanis, J., J. C. R. Hunt, and C. F. Barrett (1993), Saltating particles over flat beds, *J. Fluid Mech.*, *251*, 661-685.

Namikas S. L. (1999), Aeolian saltation: field measurements and numerical simulations, PhD Thesis, University of Southern California, Los Angeles.

Namikas, S. L. (2003), Field measurement and numerical modelling of aeolian mass flux distributions on a sandy beach, *Sedimentology*, *50*(2), 303-326.

Namikas, S. L. (2006), A conceptual model of energy partitioning in the collision of saltating grains with an unconsolidated sediment bed, *Journal of Coastal Research*, *22*(5), 1250-1259.

Nemoto, M., and K. Nishimura (2004), Numerical simulation of snow saltation and suspension in a turbulent boundary layer, *Journal of Geophysical Research-Atmospheres*, *109*(D18), D18206.

Nikuradse, J. (1933), Laws of flow in rough pipes (1950 translation), Tech. Memo. 1292, *Natl. Advis. Comm. on Aeronaut.*, Washington, D. C.

Nishimura, K., and J. C. R. Hunt (2000), Saltation and incipient suspension above a flat particle bed below a turbulent boundary layer, *Journal of Fluid Mechanics*, *417*, 77-102.

Oger, L., et al. (2005), Discrete Element Method studies of the collision of one rapid sphere on 2D and 3D packings, *European Physical Journal E*, *17*(4), 467-476.

Owen, P. R. (1964), Saltation of uniform grains in air, *Journal of Fluid Mechanics*, *20*(2), 225-242.

Oyama, V., B. Berdahl, and G. Carle (1977), Preliminary findings of Viking gas-exchange experiment and a model for Martian surface chemistry, *Nature, 265* (5590), 110-114.

Painter, T. H., et al. (2007), Impact of disturbed desert soils on duration of mountain snow cover, *Geophysical Research Letters*, *34*(12), L12502.

Prandtl, L. (1935), The mechanics of viscous flows, in *Aerodynamic Theory*, Vol. III, edited by W. F. Durand, Springer, Berlin.

Prospero, J. M. (1999), Assessing the impact of advected African dust on air quality and health in the eastern United States, *Human and Ecological Risk Assessment*, *5*(3), 471-479.

Qu, J. J., et al. (2004), Wind tunnel simulation experiment and investigation on the electrification of sandstorms, *Sci. China Ser. D*, *47*, 529-539.

Raizer, Y. P. (1997), *Gas Discharge Physics*, Springer, Berlin.

Randall, J. T., and M. H. F. Wilkins (1945), Phosphorescence and electron traps .2. The interpretation of long-period phosphorescence, *Proc. R. Soc. A*, *184*(999), 390-407.

Rasmussen, K. R., and H. E. Mikkelsen (1991), Wind tunnel observations of aeolian transport rates, *Acta Mechanica, Suppl. 1*, 135-144.

Rasmussen, K. R., and H. E. Mikkelsen (1998), On the efficiency of vertical array aeolian field traps, *Sedimentology*, *45(4)*, 789-800.

Rasmussen, K. R., and M. Sorensen (2008), Vertical variation of particle speed and flux density in aeolian saltation: Measurement and modeling, *Journal of Geophysical Research-Earth Surface*, *113*(F2), F02S12.

Raupach, M. R. (1991), Saltation laters, vegetation canopies and roughness lengths, *Acta Mech., Suppl.* 1, 83-96, 1991.

Raupach, M. R., et al. (1996), Coherent eddies and turbulence in vegetation canopies: The mixing-layer analogy, *Boundary-Layer Meteorology*, *78*(3-4), 351-382.

Renno, N. O., A. S. Wong, S. K. Atreya, I. de Pater, and M. Roos-Serote (2003), Electrical Discharges and Broadband Radio Emission by Martian Dust Devils and Dust Storms, *Geophys. Res. Lett., 30*(22), 2140.

Renno, N. O., et al. (2004), MATADOR 2002: A pilot field experiment on convective plumes and dust devils, *Journal of Geophysical Research-Planets*, *109*(E7), E07001.

Renno, N. O., and J. F. Kok (2008), Electrical activity and dust lifting on Earth, Mars, and beyond, *Space Sci. Rev.*, *137*(1-4), 419-434, doi:10.1007/s11214-008-9377-5.

Renno, N. O., J. F. Kok, H. Kirkham, and S. Rogacki (2008), A miniature sensor for electrical field measurements in dusty planetary atmospheres, *J. Phys. Conf. Ser.,* 142, 012075.

Revel, J., et al. (2003), Generation of static electricity during fluidisation of polyethylene and its elimination by air ionisation, *Powder Technology*, *135*, 192-200.

Reynolds, A. M. (2000), On the formulation of Lagrangian stochastic models for heavy-particle trajectories, *Journal of Colloid and Interface Science*, *232*(2), 260-268.

Rice, M. A., et al. (1995), An experimental study of multiple grain-size ejecta produced by collisions of saltating grains with a flat bed, *Sedimentology*, *42*(4), 695-706.

Rice, M. A., et al. (1996), Observations of collisions of saltating grains with a granular bed from high-speed cine-film, *Sedimentology*, *43*(1), 21-31.

Rioual, F., et al. (2000), Experimental study of the collision process of a grain on a two-dimensional granular bed, *Physical Review E*, *62*(2), 2450-2459.

Rubinow, S. I., and J. B. Keller (1961), The Transverse Force on Spinning Spheres Moving in a Viscous Liquid, *Journal of Fluid Mechanics*, *11*(3), 447-459.

Ruf, C., N. O. Renno, J. F. Kok, E. Bandelier, M. J. Sanders, S. Gross, L. Skjerve, B. Cantor, The emission of non-thermal radiation by a Martian dust storm, *Geophys. Res. Lett.*, in review.

Saffman, P. G. (1965), The Lift on a Small Sphere in a Slow Shear Flow, *Journal of Fluid Mechanics*, *22*, 385.

Saffman, P. G. (1968), Correction, *Journal of Fluid Mechanics*, *31*, 624-&.

Sawford, B. L., and F. M. Guest (1991), Lagrangian statistical simulation of the turbulent motion of heavy particles, *Boundary-Layer Meteorology*, *54*(1-2), 147-166.

Sauermann, G., et al. (2001), Continuum saltation model for sand dunes, *Physical Review E*, *6403*(3), 031305.

Schein, L. B. (2007), Applied physics - Recent progress and continuing puzzles in electrostatics, *Science*, *316*(5831), 1572-1573.

Schmidt, D.S., R.A. Schmidt, and J.D. Dent (1998), Electrostatic force on saltating sand, *J. Geophys. Res.*, 103(D8), 8997-9001, 1998.

Schmidt, D. S., et al. (1999), Electrostatic force in blowing snow, *Bound.-Lay. Meteorol.*, *93*(1), 29-45.

Shaw, P. E. (1926), The electrical charges from like solids, *Nature*, *118*, 659-660.

Shao, Y., and M. R. Raupach (1992), The overshoot and equilibration of saltation, *Journal of Geophysical Research-Atmospheres*, *97*(D18), 20559-20564.

Shao, Y., M. R. Raupach, and P. A. Findlater (1993), Effect of saltation bombardment on the entrainment of dust by wind, *Journal of Geophysical Research-Atmospheres*, *98*(D7), 12719-12726.

Shao, Y. P. (1995), A Lagrangian stochastic model for nonpassive particle diffusion in turbulent flows, *Mathematical and Computer Modelling*, *21*(9), 31-37.

Shao, Y. P., and A. Li (1999), Numerical modelling of saltation in the atmospheric surface layer, *Boundary-Layer Meteorology*, *91*(2), 199-225.

Shao, Y. P., and H. Lu (2000), A simple expression for wind erosion threshold friction velocity, *Journal of Geophysical Research-Atmospheres*, *105*(D17), 22437-22443.

Shao, Y. P., and M. Mikami (2005), Heterogeneous saltation: Theory, observation and comparison, *Boundary-Layer Meteorology*, *115*(3), 359-379.

Shao, Y. P. (2000), *Physics and Modelling of Wind Erosion*, Kluwer Academic, Dordrecht.

Sherman, D. J. (1992), An equilibrium relationship for shear velocity and apparent roughness length in aeolian saltation, *Geomorphology*, *5*(3-5), 419-431.

Sherman, D. J., and E. J. Farrell (2008), Aerodynamic roughness lengths over movable beds: Comparison of wind tunnel and field data, *Journal of Geophysical Research-Earth Surface*, *113*(F2), F02S08.

Shinbrot, T., et al. (2006a), Triboelectrification and razorbacks: Geophysical patterns produced in dry grains, *Phys. Rev. Lett.*, *96*(17).

Shinbrot, T., et al. (2008), Spontaneous tribocharging of similar materials, *Epl*, *83*(2).

Shinbrot, T., and H. J. Herrmann, Granular matter – Static in motion, *Nature*, 451(7180), 773-774.

Snyder, W. H., and J. L. Lumley (1971), Some measurements of particle velocity autocorrelation functions in a turbulent flow, *Journal of Fluid Mechanics*, *48*(JUL13), 41.

Sokolik, I. N., et al. (2001), Introduction to special section: Outstanding problems in quantifying the radiative impacts of mineral dust, *Journal of Geophysical Research-Atmospheres*, *106*(D16), 18015-18027.

Sorensen, M. (1991), An analytic model of wind-blown sand transport, *Acta Mech. Suppl. 1*, 67-81.

Sorensen, M., and I. McEwan (1996), On the effect of mid-air collisions on aeolian saltation, *Sedimentology*, *43*(1), 65-76.

Sorensen, M. (2004), On the rate of aeolian transport, *Geomorphology*, *59*(1-4), 53-62.

Sterk, G. (2003), Causes, consequences and control of wind erosion in Sahelian Africa: A review, *Land Degradation & Development*, *14*(1), 95-108.

Stow, C.D. (1969), Dust and sand storm electrification, *Weather*, 24,134-24,137.

Sun, D. L., et al. (2008), Contrasting the 2007 and 2005 hurricane seasons: Evidence of possible impacts of Saharan dry air and dust on tropical cyclone activity in the Atlantic basin, *Geophysical Research Letters*, *35*(15), L15405.

Taniere, A., et al. (1997), On the behaviour of solid particles in a horizontal boundary layer with turbulence and saltation effects, *Experiments in Fluids*, *23*(6), 463-471.

Tegen, I., and A.A. Lacis (1996), Modeling of particle size distribution and its influence on the radiative properties of mineral dust aerosol, *J. Geophys. Res.*, *101*, 19,237 – 19,244.

Twomey, S. (1974), Pollution and planetary albedo, *Atmospheric Environment*, *8*, 1251-1256.

Ungar, J. E., and P. K. Haff (1987), Steady-state saltation in air, *Sedimentology*, *34*(2), 289-299.

Vandop, H., et al. (1985), Random-walk models for particle displacements in inhomogeneous unsteady turbulent flows, *Physics of Fluids*, *28*(6), 1639-1653.

Wahlin, L. (1986), Atmospheric Electrostatics, Wiley, New York.

Wang, D. W., et al. (2008), Statistical analysis of sand grain/bed collision process recorded by high-speed digital camera, *Sedimentology*, *55*(2), 461-470.

Werner, B.T. (1987). *A physical model of wind-blown sand transport*, Ph.D. thesis, California Institute of Technology.

Werner, B. T. (1990), A steady-state model of wind-blown sand transport, *Journal of Geology*, *98*(1), 1-17.

White, B. R., and J. C. Schulz (1977), Magnus effect in saltation, *Journal of Fluid Mechanics*, *81*(JUL13), 497-512.

White, B. R. (1982), 2-phase measurements of saltating turbulent boundary-layer flow, *International Journal of Multiphase Flow*, *8*(5), 459-473.

Willetts, B.B. and M.A. Rice (1985), Inter-saltation collisions, *Proc. Int. Workshop Physics of Blown Sand*, *1*, 83-100.

Willetts, B. B., and M. A. Rice (1986), Collisions in aeolian saltation, *Acta Mechanica*, *63*(1-4), 255-265.

Willetts, B. B., and M. A. Rice (1989), Collisions of quartz grains with a sand bed – the influence of incident angle, *Earth Surface Processes and Landforms*, *14*(8), 719-730.

Williams E. R., et al. (2009), The electrification of dust-lofting gust fronts ('haboobs') in the Sahel, *Atm. Res.*, 91(2-4), 292-298.

Williams, G. (1964), Some aspects of the eolian saltation load, *Sedimentology*, *3*(4), 257-287.

Wilson, J. D., and B. L. Sawford (1996), Review of Lagrangian stochastic models for trajectories in the turbulent atmosphere, *Boundary-Layer Meteorology*, *78*(1-2), 191-210.

White, B. R. (1979), Soil transport by winds on Mars, *Journal of Geophysical Research*, *84*(NB9), 4643-4651.

Xie, L., et al. (2007), Laboratory measurement of saltating sand particles' angular velocities and simulation of its effect on saltation trajectory, *Journal of Geophysical Research-Atmospheres*, *112*(D12), D12116.

Yair, Y., et al. (2006), Evidence for synchronicity of lightning activity in networks of spatially remote thunderstorms, *Journal of Atmospheric and Solar-Terrestrial Physics*, *68*(12), 1401-1415.

Yue, G. W., and X. J. Zheng (2007), Effect of thermal diffusion and electrostatic force on evolution of wind-blown sand flow, *Applied Mathematics and Mechanics-English Edition*, *28*(2), 183-192.

Zhai, Y., S. A. Cummer, and W. M. Farrell (2006), Quasi-electrostatic field analysis and simulation of Martian and terrestrial dust devils, *J. Geophys. Res., 111* (E6), E06016, doi:10.1029/2005JE002618.

Zhang, H.-F., Wang, T., Qu, J.-J., and M.-H. Yan (2004), An Experimental and observational study on the electric effect of sandstorms, *Chinese J. Geophys. – Ch.*, *47*, 53-60.

Zheng, X.J., N. Huang, and Y.-H. Zhou (2003), Laboratory measurement of electrification of wind-blown sands and simulation of its effect on sand saltation movement, *J. Geophys. Res.*, *108*(D10), 4322, doi:10.1029/2002JD002572.

Zheng, X. J., et al. (2006), The effect of electrostatic force on the evolution of sand saltation cloud, *European Physical Journal E*, *19*(2), 129-138.

Zheng, X. J., et al. (2008), A three-dimensional analysis on lift-off velocities of sand grains in wind-blown sand flux, *Earth Surface Processes and Landforms*, *33*(12), 1824-1838.

Zimon, A. (1982), *Adhesion of Dust and Powder*, 2nd ed., Consultants Bureau, New York.

Zou, X. Y., et al. (2007), Effects of the Magnus and Saffman forces on the saltation trajectories of sand grain, *Geomorphology*, *90*(1-2), 11-22.